NAVAL POSTGRADUATE SCHOOL

MONTEREY, CALIFORNIA

THESIS

THEORETICAL DESIGN AND MODELING OF AN INFANTRY RAILGUN PROJECTILE

by

James A. Brady

December 2005

Thesis Advisor: William B. Maier II
Second Reader: Ronald E. Brown

Approved for public release; distribution unlimited.

THIS PAGE INTENTIONALLY LEFT BLANK

REPORT DOCUMENTATION PAGE	*Form Approved OMB No. 0704-0188*

Public reporting burden for this collection of information is estimated to average 1 hour per response, including the time for reviewing instruction, searching existing data sources, gathering and maintaining the data needed, and completing and reviewing the collection of information. Send comments regarding this burden estimate or any other aspect of this collection of information, including suggestions for reducing this burden, to Washington headquarters Services, Directorate for Information Operations and Reports, 1215 Jefferson Davis Highway, Suite 1204, Arlington, VA 22202-4302, and to the Office of Management and Budget, Paperwork Reduction Project (0704-0188) Washington DC 20503.

1. AGENCY USE ONLY *(Leave blank)*	**2. REPORT DATE** December 2005	**3. REPORT TYPE AND DATES COVERED** Master's Thesis	
4. TITLE AND SUBTITLE: Theoretical Design and Modeling of an Infantry Railgun Projectile		**5. FUNDING NUMBERS**	
6. AUTHOR(S) James A. Brady			

7. PERFORMING ORGANIZATION NAME(S) AND ADDRESS(ES)
    Naval Postgraduate School
    Monterey, CA 93943-5000
		8. PERFORMING ORGANIZATION REPORT NUMBER	

9. SPONSORING /MONITORING AGENCY NAME(S) AND ADDRESS(ES) N/A		**10. SPONSORING/MONITORING AGENCY REPORT NUMBER**	

11. SUPPLEMENTARY NOTES The views expressed in this thesis are those of the author and do not reflect the official policy or position of the Department of Defense or the U.S. Government.

12a. DISTRIBUTION / AVAILABILITY STATEMENT Approved for public release; distribution is unlimited	**12b. DISTRIBUTION CODE**

13. ABSTRACT (maximum 200 words)

In order for railgun technology to be relevant to the Infantry, the design of the projectile must incorporate the following three concepts: an effective ballistics package, geometries for aerodynamic stability; and a non-parasitic conducting armature.   I designed an effective 30mm and scaled 40mm projectile which incorporates the aforementioned concepts.   My ballistics analysis concluded with two AUTODYN™ finite-element computer models that refined theoretical estimates for target penetration. The proposed railgun projectiles were effective in penetrating 100 mm of Rolled Homogenous Armor and in perforating 8 inches of Double Layered Reinforced Concrete. My theoretical analysis in aerodynamics predicts in-flight stability with a minimum static margin of approximately two percent. The analysis and modeling of the electromagnetic launch resulted in an adequate design. For this analysis, I used three Comsol Multiphysics™ finite-element computer models. The modeling results validated fundamental railgun equations. The final projectile design concluded with a 3 m barrel and is characterized by the following parameters: conducting rails with an inductance gradient ≈ 0.38 μH/m; an average temperature rise in the rails of 20 °C per shot; an effective current of less than 2 MA; and a projectile launch velocity of 1100 m/s.

14. SUBJECT TERMS Railgun, Projectile, Ballistic Penetration, Aerodynamic Stability, Electromagnetic Launch, Future Combat System, FCS, Infantry			**15. NUMBER OF PAGES** 146
			16. PRICE CODE
17. SECURITY CLASSIFICATION OF REPORT Unclassified	**18. SECURITY CLASSIFICATION OF THIS PAGE** Unclassified	**19. SECURITY CLASSIFICATION OF ABSTRACT** Unclassified	**20. LIMITATION OF ABSTRACT** UL

NSN 7540-01-280-5500

Standard Form 298 (Rev. 2-89)
Prescribed by ANSI Std. 239-18

THIS PAGE INTENTIONALLY LEFT BLANK

THEORETICAL DESIGN AND MODELING OF AN INFANTRY RAILGUN PROJECTILE

James A. Brady
Captain, Infantry, United States Army
B.S., Physics, United States Military Academy, 1997

Submitted in partial fulfillment of the
requirements for the degree of

MASTER OF SCIENCE IN PHYSICS

from the

NAVAL POSTGRADUATE SCHOOL
December 2005

Author: James A. Brady

Approved by: William B. Maier II
                   Thesis Advisor

                   Ronald E. Brown
                   Co-Advisor

                   James Luscombe
                   Chairman, Department of Physics

THIS PAGE INTENTIONALLY LEFT BLANK

ABSTRACT

In order for railgun technology to be relevant to the Infantry, the design of the projectile must incorporate the following three concepts: an effective ballistics package, geometries for aerodynamic stability, and a non-parasitic conducting armature. I designed an effective 30mm and scaled 40mm projectile that incorporates the aforementioned concepts. My ballistics analysis concluded with two AUTODYN™ finite-element computer models that refined theoretical estimates for target penetration. The proposed railgun projectiles were effective in penetrating 100 mm of Rolled Homogenous Armor and in perforating 8 inches of Double Layered Reinforced Concrete. My theoretical analysis in aerodynamics predicts in-flight stability with a minimum static margin of approximately two percent. The analysis and modeling of the electromagnetic launch resulted in an adequate design. For this analysis, I used three Comsol Multiphysics™ finite-element computer models. The modeling results validated fundamental railgun equations. The final projectile design concluded with a 3 m barrel and is characterized by the following parameters: conducting rails with an inductance gradient ≈ 0.38 μH/m; an average temperature rise in the rails of 20 °C per shot; an effective current of less than 2 MA; and a projectile launch velocity of 1100 m/s.

THIS PAGE INTENTIONALLY LEFT BLANK

TABLE OF CONTENTS

LIST OF FIGURES

LIST OF TABLES

THIS PAGE INTENTIONALLY LEFT BLANK

LIST OF SYMBOLS, ACRONYMS, AND ABBREVIATIONS

A	Cross-sectional Area; or Aspect Ratio
a_P	Projectile's acceleration
b	Wing Span
C_{D_0}	Coefficient of Drag for Zero Angle of Attack
$\left(C_{D_0}\right)_{BODY}$	Coefficient of Drag for the Projectile's Body
$\left(C_{D_0}\right)_{BODY,\,COAST}$	Coefficient of Drag for Base Pressure Drag from the Projectile's Body
$\left(C_{D_0}\right)_{BODY,\,FRICTION}$	Coefficient of Drag for Skin Friction from the Projectile's Body
$\left(C_{D_0}\right)_{BODY,WAVE}$	Coefficient of Drag for Wave Drag from the Projectile's Body
$\left(C_{D_0}\right)_{PF}$	Coefficient of Drag for the Pitch Fins
$\left(C_{D_0}\right)_{TAIL}$	Coefficient of Drag for the Tail Fins, used for Pitch Fins or Yaw Fins
$\left(C_{D_0}\right)_{TAIL,\,FRICTION}$	Coefficient of Drag for Skin Friction from the Tail Fins
$\left(C_{D_0}\right)_{TAIL,WAVE}$	Coefficient of Drag for Wave Drag from the Tail Fins
$\left(C_{D_0}\right)_{YF}$	Coefficient of Drag for the Yaw Fins
$\left(C_{N\alpha}\right)_N$	Nose-body Normal Force Coefficient Derivation due to Angle of Attack α
$\left(C_{N\beta}\right)_N$	Nose-body Normal Force Coefficient Derivation due to Angle of Attack β
$\left(C_{N\alpha}\right)_{PF}$	Pitch Fin Normal Force Coefficient Derivation due to Angle of Attack α
$\left(C_{N\beta}\right)_{YF}$	Yaw Fin Normal Force Coefficient Derivation due to Angle of Attack β
C_{MAC}	Mean Aerodynamic Chord
$\bar{c}$	Reference Chord Length
D	Primary Diameter
D_0	Zero Angle of Attack Drag Force

d	Equivalent Diameter
F	Lorentz Force; or Railgun Force
f_c	Compressive strength of concrete
G	Electrical Action
g	Specific Action
I	Effective Current
L	Primary Length
L'	Inductance Gradient
L_N	Length of Nose cone
M	Primary Mass; or Mach number
M'	Residual Mass after penetration
M_P	Mass of Projectile
$(M_\alpha)_P$	Pitching Moment
$(M_\beta)_Y$	Yaw Moment
n_W	Number of Wing Planforms
$P(V_C)/L$	Penetration Depth per Length of projectile at the Critical Velocity
P_{rigid}/L	Penetration Depth per Length of projectile as a rigid penetrator
P_{tot}/L	Total Penetration Depth per Length of projectile
q_∞	Dynamic Pressure
r_N	Radius of Nose Cone; or Nose-body effective moment arm
r_{PF}	Pitch Fin effective moment arm
r_{YF}	Yaw Fin effective moment arm
S_{REF}	Surface Reference Area
S_{BODY}	Body Reference Area
S_{PF}	Surface Area of Pitch Fins
S_{TF}	Surface Area of Tail Fins, used for Pitch Fins or Yaw Fins
S_{YF}	Surface Area of Yaw Fins

SM_P	Pitch Static Margin
SM_Y	Yaw Static Margin
t_{MAC}	Wing Thickness
t_p	Concrete Thickness Required to Prevent Perforation
t_s	Concrete Thickness Required to Prevent Scabbing
T	Target Thickness
U_∞	Dynamic Flow Velocity
u	Projectile's velocity
V_L	Limit Velocity
V_N	Volume of Nose Cone
V_r	Residual Velocity
v_L	Electromagnetic Launch Velocity
$(X_{AC})_P$	Aerodynamic Center with respect to Pitch
$(X_{AC})_Y$	Aerodynamic Center with respect to Yaw
X_{CG}	Center of Gravity
$(X_{CP})_N$	Nose-body Center of Pressure
$(X_{CP})_{PF}$	Pitch Fin Center of Pressure
$(X_{CP})_{YF}$	Yaw Fin Center of Pressure
x	Concrete Thickness Required to Prevent Penetration
x_L	Railgun Barrel Length
α	Pitch Angle of Attack
β	$\sqrt{M^2-1}$, where M is the Mach number; or Yaw Angle of Attack
ΔT	Average Temperature Change
δ_{LE}	Leading Edge Thickness Angle
Λ_{LE}	Leading Edge Angle
γ	Specific Heat Ratio
θ	Impact Obliquity Angle

Al	Aluminum
ARL	Army Research Laboratory
APFSD	Armor Piercing Fin Stabilized Discarding Sabot
CPA	Compensated Pulsed Alternator
Cu	Copper
DLRC	Doubled Layered Reinforced Concrete
FCS	Future Combat System
IAT	Institute for Advanced Technology
IFV	Infantry Fighting Vehicle
L/D	Length to Diameter Ratio
MOD	Modification
NDRC	National Defense Research Committee
RHA	Rolled Homogeneous Armor
SAM	Specific Action to Melt
SDZ	Surface Danger Zone
SM	Static Margin
T/D	Target Thickness to Projectile Diameter Ratio
W	Tungsten
2D	Two Dimensional
3D	Three Dimensional

ACKNOWLEDGMENTS

THIS PAGE INTENTIONALLY LEFT BLANK

I.   INTRODUCTION AND DESIGN OVERVIEW

A.   INTRODUCTION

Several Department of Defense Development, Test and Evaluation (DT&E) activities along with other U.S. research organizations are exploring railgun technologies with the expectation of replacing current military munitions with hypervelocity projectiles. Of particular interest to the Army are currently funded programs to develop railgun applications for its Future Combat System (FCS) [1]. A key unresolved challenge in this effort is the design of an appropriate railgun projectile. The current primary concept for a potential FCS Army railgun projectile integrates a hypervelocity long-rod penetrator with an aluminum fall-away electrical conducting armature [2]. This projectile concept endeavors to meet the FCS requirement for defeating modern composite armor in conventional warfare. However, it has limited utility in urban military operations where the forward placement of dismounted infantry and minimization of collateral damage are important operational requirements.   Given the current integration of units into combined arms teams and the likelihood of future unconventional urban conflicts, the optimal design of a railgun projectile must incorporate a multipurpose penetrator that minimizes fratricide and collateral damage.

One objective of the FCS development program is to replace the capabilities of the M1 Abrams Main Battle Tank (MBT) and the M3 Bradley Infantry Fighting Vehicle (IFV) with one multipurpose armored vehicle [3]. The Army has already organized and fielded an Intermediate Brigade Combat Team (IBCT) that uses Light Armor Vehicles (LAV) in an attempt to replace the capabilities of the MBT and IFV. The IBCT still has two different vehicles to support combined arms operations, a mobile gun system and an infantry carrier vehicle. Major benefits of the LAV are that it is easily deployable via Air Force airlift assets and is highly mobile in rough terrain. The shortfalls of the LAV are a reduction in lethality and survivability [4]. The inherent deficiencies with the LAV have caused the Army to retain the MBT and IFV until it is able to field the FCS as more suitable replacement.

The Army intends to develop a railgun for the FCS in order to match or exceed the lethality of the MBT and IFV, while trying to equal the deployability and mobility of

the LAV. The challenges for a railgun design include appropriate barrel dimensions, power supplies, and projectile launch configurations. Longer railgun barrels require less electrical current to achieve a hypervelocity projectile launch. The barrel length restriction for the FCS is approximately 3 meters. This estimate is based upon a barrel that is one-third the maximum vehicle length for the FCS which is eight meters [5]. A three meter railgun barrel is shorter than full scale experimental laboratory barrels (ten meters) [6]. The optimal geometries for the conducting rails are rectangular configurations. These geometries allows for the highest inductance per unit length, or inductance gradient, which directly affects the electromagnetic force on a projectile [7]. The primary candidate for the railgun power supply is a pair of inertial energy storage rotating machines, also known as Compensated Pulsed Alternators (CPA). The Army version of this power supply is projected to have a maximum energy storage capacity of 20 MJ and a peak output current of 1.08 MA [8]. The Armor Piercing Fin Stabilized Sabot Discarding (APFSD) projectile is a leading candidate for the primary ballistics package because it has proven lethality against modern armored vehicles [2]. APFSD designers can easily configure the sabot petals to fit the geometry of the barrel [9]. The projectile launch package must include a device to conduct current and maintain electrical contact with the rails. The portion of a railgun projectile's launch package that conducts current induces the necessary electromagnetic force required for acceleration and final muzzle velocity. Army designers have decided that the best device for this purpose is a base-push or mid-ride fall-away aluminum armature. The proposed configurations of these armatures have shapes that allow the launch induced electromagnetic force to push the sides of this malleable metal against the rails [10]. Given the aforementioned FCS railgun constraints and design solutions, the Army believes that it can achieve launch velocities of 2.5 km/s using an APFSD projectile and deliver lethal impact energy to conventional armor targets.

The Army designed the APFSD round for Kinetic Energy (KE) impacts against heavy to light skin enemy armored vehicles. The primary ballistic packages of APFSD projectiles are tungsten or depleted-uranium penetrators that have length to diameter ratios (L/D) of anywhere between 5 and 30, with respective diameters between 15 mm and 7 mm [11]. These penetrators are highly effective at defeating modern enemy

armored vehicles. The high L/D characteristic that makes them devastating against armor actually work against them when penetrating urban targets. Bradley IFV gunners who have used conventional APFSD rounds against urban or concrete structures report that the penetrator passes through the target leaving a hole on the order of its body diameter. These gunners prefer to use the larger diameter aluminum-training round against concrete targets because it is significantly more effective [11]. From a ballistic effects perspective, as seen by IFV gunners, the APFSD is not a multipurpose projectile.

When considering engagements with the proposed railgun launch package, the fall-away armature and sabot petals induce restrictions on its safe battlefield employment. The U.S. military successfully trains with APFSD rounds and has used them in combat. The Department of the Army has mandated the following restrictions on the use of the APFSD with dismounted infantry: firing over the heads of unprotected personnel is prohibited; no personnel can be within 60 degrees of the gun target line for the first 100 m of the projectile's trajectory; no personnel can be within 7 degrees of the gun target line after the 100 m primary limit up to 400 m [12]. These restrictions are for the Bradley IFV using a conventionally fired APFSD, and they are even greater for the M1 Abrams. The predictive error impact area, Surface Danger Zone (SDZ), for the Bradley M919 APFSD extends from the IFV out to 18 km [12]. The proposed railgun launch package will force the Army to impose more significant restrictions on the placement of dismounted infantry and SDZs because the aluminum fall-away armature and ballistic penetrator will have lethal launch velocities at 2.5 km/s. The Army cannot ignore these restrictions, and therefore, ground commanders will most likely relegate the use of railguns only to specific engagements such as those found in conventional armor warfare.

If the urban and unconventional style of warfare in Operations Enduring Freedom and Iraqi Freedom are any indication of the future, then the proposed design of the Army railgun projectile will have limited utility. Armor and Infantry units operate in a combined arms team where dismounted infantry are often forward of supporting heavy armor assets. Within urban areas this is especially true. Armored vehicles that travel through urban terrain, without the support of forward or flanking infantry, are susceptible to side attacks by an unconventional enemy force. One must expect that dismounted infantry will continue to operate forward of FCS vehicles in future combat situations.

Another important issue in urban warfare is irregular friendly unit boundaries. Senior ground commanders often break up the control of towns or cities into multiple unit sectors. Subordinate commanders operating in these sectors normally find that they have weapons orientations toward other friendly units, and they must be mindful of the maximum effective range of their most lethal weapons. Given that company level sectors in urban operations are anywhere between 5 to 10 km in width or depth, the approximate 18 km maximum effective range of a conventional APFSD will most certainly cross friendly unit boundaries. Another significant consideration in urban operations is the minimization of collateral damage. Ground commanders cannot control or predict the amount of collateral damage that APFSD rounds will produce in urban terrain and are unwilling to use them unless there is a military necessity. If the future FCS vehicle has a railgun with the proposed Army APFSD projectile, then firing safety issues will most likely constrain its employment [13].

In order for railgun technology to be more relevant to Armor and Infantry combined arms teams, the design of the projectile must incorporate the following concepts:

- The projectile must be effective against various infantry targets, while minimizing collateral damage in urban warfare environments.
- The projectile must be aerodynamically stable upon launch to provide precise trajectories for surgical strikes.
- The projectile must be self-conducting during electromagnetic launch such that no parasitic mass falls away in flight, which minimizes SDZ and prevents possible fratricide.

B. DESIGN OVERVIEW

The primary objective of this thesis research was to create a credible and relevant alternative to the Army's APFSD railgun projectile, i.e. a projectile that better satisfies the operational requirements of Infantry combined arms teams in future combat urban warfare scenarios. In order to prove the merits of a credible design alternative, this research involved the analysis of ballistic penetration, aerodynamic stability, and electromagnetic launch. I limited the scope of this research to theoretical design and

modeling. Using a recursive design loop involving ballistics, aerodynamics, and electromagnetic launch, I developed a plausible design alternative, which I refer to in this thesis as the Infantry Railgun Projectile.

A critical step in any technical development process is to first create a set of reasonable constraints. Designers can then use these constraints to produce a baseline product for further testing and evaluation. After analyzing the limiting factors and operational requirements of an Army FCS railgun projectile, I created a specific set of constraints for my design (See Appendix A). Using these constraints, I developed a baseline 30mm primary diameter, 1.5 kg, design projectile that is shown in Figure 1. I also created a scaled 40mm, 3.5 kg, projectile that I use to expose the advantages or disadvantages of size and weight. Detailed material properties, geometrics specifications, volume, mass and overall center of mass of both design projectiles are listed in the appendix (See Appendix B) [14], [15].
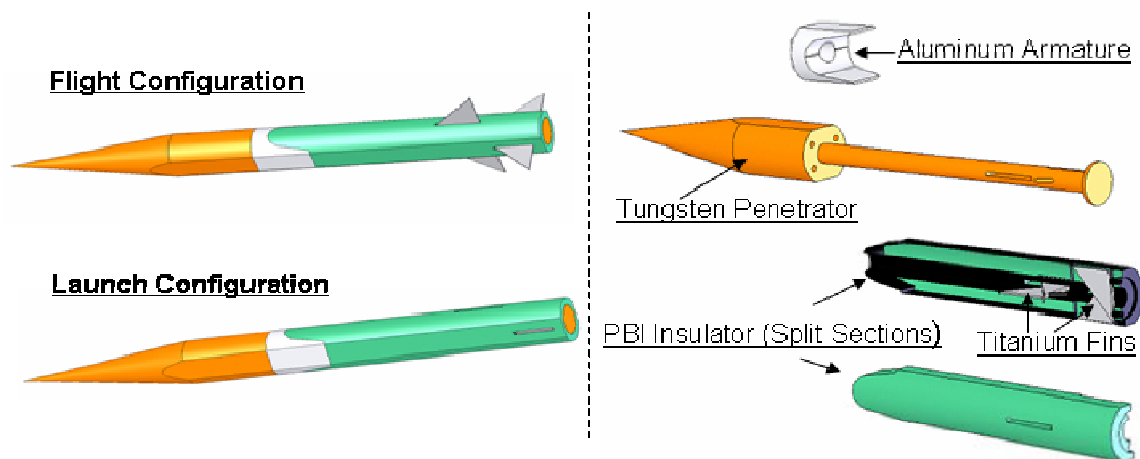
Figure 1. Infantry Railgun Projectile

As shown in Figure 1, the Infantry Railgun Projectile is comprised of four major components. The tungsten penetrator serves as the primary ballistics package in the projectile. Its configuration allows for the successful penetration of armor targets and the perforation of concrete targets. The tungsten penetrator also acts as a secondary conductive armature to distribute the flow of current through the projectile. The aluminum armature is the principal electrical conductor in the projectile. It creates the first cross contact surface between the two conducting rails inside an electromagnetic

gun. The inverted "U" shape, cut into the base of the aluminum armature, allows the launch induced electromagnetic force to push its back edges against the conducting rails. This prevents "Transition" which is a technical term that railgun designers use to describe the loss of solid electrical contact between the conducting rails [7]. Since the electrical conductivity of tungsten is similar to that of aluminum, current will distribute itself through the tungsten penetrator and aluminum armature. The Polybenzimidazole (PBI) electrical insulator behind the aluminum armature prevents current from finding a cross conduction path between the rails. The insulator's secondary purpose is to support and protect the deployable stability fins that are folded inside the projectile's body during launch. PBI is a synthetic polymer that is temperature resistant up to 500 °C and is mechanically strong (42 MPa compressive yield and 160 MPa ultimate tensile strength) [15]. Another important property of this polymer is that manufacturers can easily cast this material into cylindrical shapes [16]. The last major component of the projectile is the titanium stability fins. Their function is to provide in-flight stability. The forward set of fins is for yaw stability, and the rear set is for pitch stability. I do not discuss the exact assembly of these components because that would involve specific engineering practices that do not fall into the scope of this research. Considering the sophistication of several Army weapon systems, I assume that the assembly of this projectile is both realistic and achievable. Overall, these four components act in concert with each other to allow for a successful electromagnetic launch, stable trajectory, and penetration of realistic targets.

The configuration of the design projectile is suitable for electromagnetic launch from a rectangular railgun bore. The choice of materials and the geometric dimensions of the conducting rails are crucial factors in the analysis of electromagnetic launch. Multiple research organization have conceptualized, developed, and experimentally tested railgun barrels that use copper rectangular conducting rails. Given a generic version of this railgun barrel from the Institute for Advanced Technology (IAT), I have paired it with the design projectile to create a conceptual barrel that includes insulation and confinement [8]. The configuration of this barrel is shown in Figure 2.

Infantry Railgun Barrel

Steel Confinement Material

Rectangular Bore

Ceramic Insulator

x_L = 3 m barrel

Copper Conducting Rails
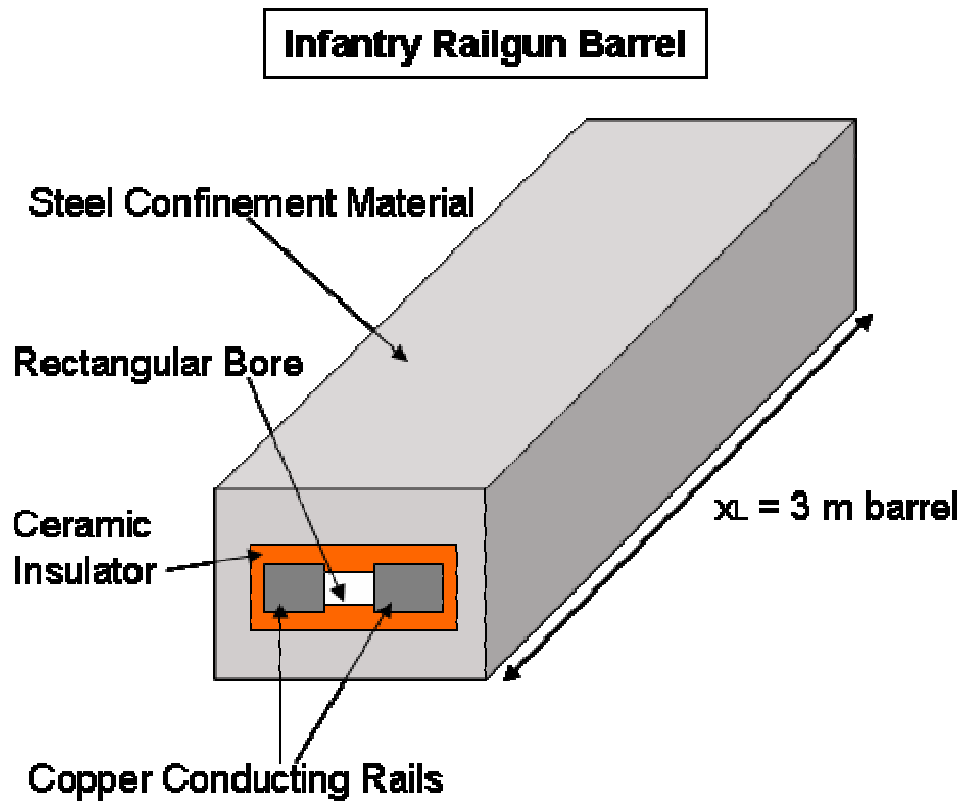
Figure 2.   Generic Railgun Barrel

In summary, I developed both a baseline and a scaled projectile design that included constraints imposed by operational concerns, rectangular conducting rails and in-flight stability. I analyzed ballistic effects with semi-empirical equations. The ballistic analysis produced minimum penetration velocities that I feed into my aerodynamic analysis. Using semi-empirical aerodynamic equations, I made estimates on aerodynamic stability and found that the projectiles were at least neutrally stable at a flight velocity of 1100 m/s with a minimum static margin of two percent. I then analyzed aerodynamic drag with further semi-empirical equations, and developed an equation for both projectiles that estimated their velocities with respect to flight distance. These equations allowed for calculations of final impact velocities for a 2 km and 500 m target. Using the impact velocities and a modified form of both design projectiles, I successfully modeled their impacts against the 2 km and 500 m targets with AUTODYN™, a finite-element hydro-code. Given the constraints of a 3 meter barrel length, an average temperature rise in the rails of 20 °C, and an 1100 m/s launch velocity, I successfully optimized the electromagnetic launch to produce final rail dimensions, an effective current, and the

7

inductance gradient. I used another finite-element code, Comsol Multiphysics™, to model static currents, magnetic fields, and the resulting electromagnetic force.   I compared the modeled inductance gradients to their theoretic values, and found agreement to within 10 percent. Using this finite-element code one more time, I created a transient conductive heat model to analyze the temperature rise in the aluminum armature over the 5 ms launch time.   I found that the aluminum armatures for both projectiles were below their melting points. In conclusion, the final designs of both Infantry Railgun Projectiles have satisfied the objectives of this thesis research. Although further work on these projectiles is necessary for their practical development, they serve as feasible alternatives to the APFSD railgun projectile.

II. BALLISTICS

A. BALLISTICS OVERVIEW

During the initial design phases of this research, I first tested all geometric and material projectile configurations against a primary ballistic objective. My ballistic analysis was always the first step in a recursive design loop that also analyzed aerodynamic stability and electromagnetic launch. I placed great emphasis upon choosing appropriate targets and evaluating theoretical penetration effects. The results of this ballistic analysis show that the design projectiles in this thesis have characteristics necessary to defeat modern battlefield targets.

The primary ballistic objective for this research is the penetration of 100 mm of Rolled Homogenous Armor (RHA) with a zero degree obliquity angle (normal incidence) at a range of 2 km. The parameters of RHA thickness, obliquity angle and range are mutually important variables that represent an equivalent medium-armor target. All modern Infantry Fighting Vehicles (IFV) have kinetic energy projectiles. A comparison of international IFV armor penetrators shows diverse penetration capabilities [17]. Individual countries place different design importance in areas such as vehicle weight, rates of fires, ammunition carrying capacity, and survivability [18]. After investigating various IFV penetrators and their respective penetration capabilities, I found that the primary ballistic objective listed above is realistic. Furthermore, an IFV projectile that can penetrate this target is at the forefront of current technology [17].

I selected a standard 200 mm thick Double Layered Reinforced Concrete (DLRC) target as a secondary ballistic objective in order to evaluate the multipurpose characteristics of the railgun projectile. All modern IFV armor penetrators can easily perforate this target [11]. Army weapons researchers normally cite the perforation hole-diameter as an important ballistic effect in concrete targets [19]. Most IFV armor-piercing projectiles are long-rod penetrators. They are less than 20 mm in diameter, and therefore, leave small holes in DLRC. A modern IFV can fire multiple bursts at the same point of aim to produce a greater penetration diameter [11]. This tactic is effective against a thin non-reinforced concrete structure. When IFV gunners attempt this action

against DLRC with armor piercing projectiles, they normally create a "jailed-window" effect in the concrete, shaped by the steel reinforcements [11]. In certain circumstances, ground combat commanders want to use an IFV to create breech-holes through buildings and reinforced bunkers [11]. For this reason, researchers want to develop IFV penetrators that will create the largest possible hole in concrete. Several experts agree that a 200 mm DLRC target is a realistic choice when the focus of research is to analyze penetration and perforation effects against urban concrete structures [19].

Throughout the 20th century, ballistic experts used both empirical and semi-empirical formulas to evaluate the penetration capability of solid cylindrical projectiles against armor targets [20]. Before the use of computers, some modern experts focused on the limit velocity to gage penetration effects. Researchers developed and refined a semi-empirical formula, the velocity ballistic limit, to estimate minimum penetration velocities in thick armor targets. Ballistic experts restrict the application of this formula to specific projectile geometries, armor thicknesses, and impact velocities. The parameters of the projectiles designed in this thesis satisfy the constraints for the formula and match the range of experimental data that researchers used for its validation. I compared the accuracy of the velocity ballistic limit against one set of equivalent experimental data [21]. The velocity ballistic limit agreed with the results of the external experimental data to within two percent. In this report, I initially used the velocity ballistic limit formula as the primary analytical method for analyzing RHA penetration effectiveness. The major utility of this formula is that it allows one to calculate the limit velocity or the minimum impact velocity required to create penetration in a particular armor target. I needed this estimate in order to conduct my analysis for aerodynamic stability and electromagnetic launch.

Ballistic experts turned their interest toward reinforced-concrete impact during the mid 1940s [22]. By 1946, the National Defense Research Committee (NDRC) developed a penetration, scabbing, and perforation thickness empirical formula.   In 1966, researchers adjusted these formulas to include the compressive strength of concrete. They refer to the new formulas as the modified-NDRC [22]. As recent as 2002, a study in the International Journal of Impact Engineering validated the use of these formulas for velocities up to 1 km/s [23]. Ballistic experts restrict the application of these formulas to

specific projectile geometries, concrete thickness to projectile diameter ratios, and impact velocities. The parameters in this thesis satisfy the constraints for the formulas and match the range of experimental data that researchers used for its validation. I used the modified-NDRC formulas as the primary analytical methods for estimating penetration, scabbing, and perforation effects in the 200 mm DLRC target.

In the absence of experimental testing, computer finite element modeling serves as the next best refinement to analytical estimates. For the purpose of validating ballistic estimates, I used the AUTODYN finite-element computer model to simulate impacts against RHA and DLRC. The modeling domain was two-dimensional (2D) axial-symmetric. I accounted for my design projectile's non-uniform diameter by adjusting this parameter to reflect an equivalent value. I reorganized the orthogonal steel-reinforcement structure in DLRC into circular rings in order to satisfy the axial-symmetric constraint in AUTODYN. My comparison of the RHA computer model to the velocity ballistic limit resulted in a greater penetration capability for the computer model. The AUTODYN stimulation for impacts into DLRC validated the modified-NDRC estimates for penetration, scabbing, and perforation. AUTODYN ballistic simulations are extremely useful in representing near realistic projectile impact scenarios. However, they cannot stand alone without agreement between theoretical estimates or experimental verification.

In order to better understand the discrepancy between the RHA computer model and the velocity ballistic limit formula, I concluded my analysis with a refined theoretical analysis. Using a variant analytical method of the Tate Model, which researchers commonly refer to as critical analysis, I found agreement with the RHA computer model. In conclusion, I am confident in the penetration effectiveness of the design projectiles against my primary ballistic objective, RHA. My analysis of the perforation effects in DLRC indicates that the design projectiles will create holes in this target as large as their primary diameters.

B. MODIFIED PROJECTILES

I created two modifications to the original configuration of the design projectile. These modifications were necessary to conduct theoretical estimates and computer model simulations. The first modification, MOD-1, pertains to calculations with the velocity

ballistic limit and the modified-NDRC formulas. The second modification, MOD-2, pertains to the AUTODYN finite element analysis. Both modifications are conservative adjustments to the original design and involve reasonable assumptions in the choice of each characteristic parameter for the two modifications.

When researchers use the velocity ballistic limit or the modified-NDRC formulas to evaluate ballistic effects, they can only conduct analysis on projectiles that have circular-cylindrical geometries with conical nose cones. Given this shape, the formulas at most require the characteristic diameter, length, mass, and nose fineness. If we consider the geometry and material composition of the design projectile in this thesis, we can assume that the tungsten portion of the projectile serves as the primary ballistic penetrator. Therefore, it is the only shape that one needs to consider in a ballistic analysis. The sides of the tungsten penetrator are shaved, and are the only geometric configurations that prevent it from being a perfect circular cylinder. In order to analyze the penetrator as a perfect cylinder, I modified the geometry to reflect a characteristic diameter, length and mass. I refer to this modified projectile as MOD-1.

It is important to define the characteristic diameter, length, and mass of MOD-1 in order to prevent any confusion in this ballistic analysis. The characteristic diameter is the equivalent diameter, d, of the tungsten penetrator's major body cylinder.   One can calculate the equivalent diameter by assuming that the cross-sectional surface area, S_{REF}, is equal to the area of a perfect circle, $S_{REF} = (\pi d^2 / 4)$.   The result of this calculation produces equivalent diameters of 29 mm and 38.8 mm for the respective 30mm and 40mm design projectiles (See Chapter III, Section C.1.b.).   I assumed that the characteristic length of MOD-1 is the distance from the tip of the nose to the end of the major body cylinder. This is a reasonable assumption since both the nose cone and major body cylinder are the only geometries that will force a perforation hole through an armor or concrete target. The characteristic mass of MOD-1 is the mass of the complete projectile, which includes materials that have no ballistic relevance. One must consider the total mass because both the velocity ballistic limit and the modified-NDRC formulas use relationships between impact kinetic energy, $MV^2/2$, and displaced target volume.

One can further examine the general shape of MOD-1 and the exact specifications for it with regard to both the 30mm and 40mm design projectiles in Figure 3.
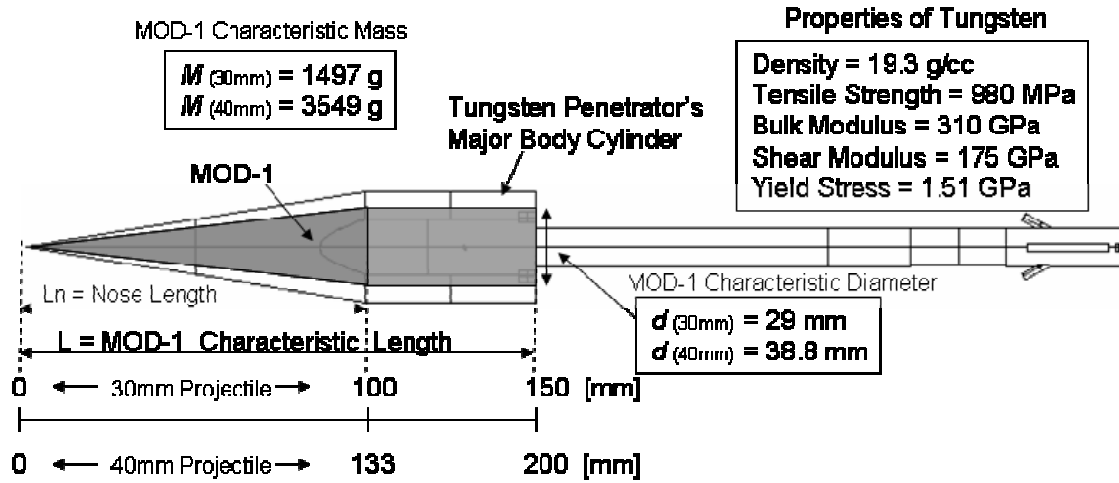
Figure 3.   Projectile Modification for Theoretical Analysis (MOD-1)

The AUTODYN modeling domains that I used in my computer simulations were two-dimension (2D) axial-symmetric. This modeling domain allowed the input of irregular 2D geometries. Using the same equivalent diameter from MOD-1, I developed a second modification for the AUTODYN analysis. With the ability to include more of the original projectile, I included the tungsten penetrator's rod cylinder up to the leading edge of the first tail fin slot, because the fin slot cuts directly through the center of the rod cylinder. The effective mass of MOD-2 is based upon the density of tungsten and the physical geometry of the modified projectile. MOD-2 has a mass that is 82 percent of the original design projectile (See Appendix B). Although the mass of MOD-2 is a significantly conservative value, the geometric constraints that I applied were necessary given the near realistic environment of the AUTODYN analysis. The general shape and parameter specification of MOD-2 are given in Figure 4.
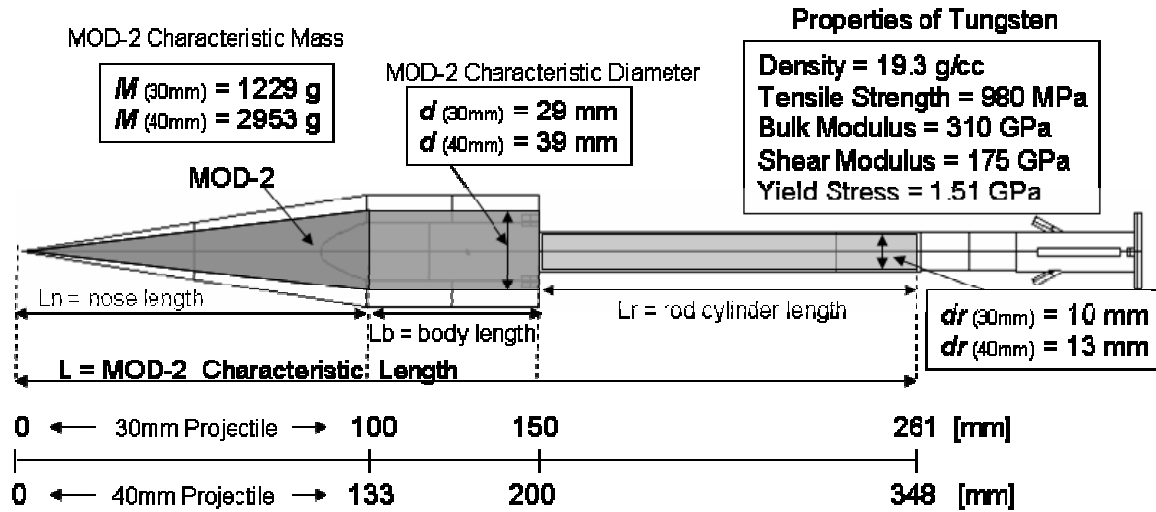
Figure 4.   Projectile Modification for Computer Modeling (MOD-2)

C.   TARGETS

1.   100 mm of Rolled Homogenous Armor

Both U.S. and international military ballistic laboratories use RHA as the standard by which to compare armor protection or ballistic penetration. In a time when new composite armor is multi-layered and complex, weapons researchers have found it useful to rate this armor in an equivalent RHA thickness. When rating a target, one must state the angle of obliquity, range to target, and RHA thickness. At a fixed target range, if we rate a piece of armor at an equivalent RHA thickness of 50 mm with a 60 degree angle of obliquity, we can approximately gage that same armor with an 85 mm thickness at normal incidence. One can understand the validity of this statement after examining the effects of the obliquity angle in the velocity ballistic limit formula, which I develop later in this chapter.

In an effort to select the appropriate RHA thickness for an IFV armor penetrator, I investigated the ballistic effectiveness of several medium-caliber Armored Fighting Vehicle (AFV) munitions. My information source, "Jane's International Defense Review," listed at least two modern 25mm-caliber projectiles with an RHA penetration capability of 31 mm. For both projectiles, the author listed an impact obliquity angle of 60 degrees and target range of 2 km. The author identified one modern 30mm-caliber projectile with an RHA penetration capability of 47 mm at an obliquity angle of 60

degrees and target range of 1 km. For that same caliber, the author also referenced a state of the art projectile with a 120 mm RHA penetration capability at normal incidence, given a target range of 1 km [17]. Using this information, I selected an RHA thickness of 100 mm, a zero degree or normal incidence obliquity angle, and a range to target of 2 km. I chose these target parameters in order to make the design of the Infantry Railgun Projectile competitive against other medium caliber penetrators. Figure 5 shows the target and its material properties. I made the diameter of this target sufficiently large such that the cross-sectional area of the impacting design projectile was less than 1% of the target area. This minimizes any radial expansion of the target during impact and properly reflects the surface area of a large armored vehicle.
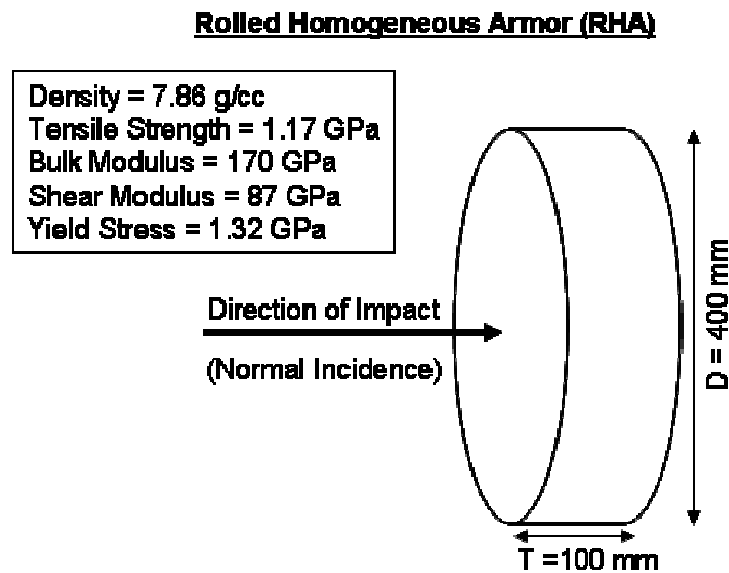
Figure 5.   RHA Target Diagram

2.   200 mm of Double Layered Reinforced Concrete

An Army Research Laboratory (ARL) report on hypervelocity penetration into concrete targets motivated my selection of a DLRC target. The ARL report stated that its DLRC target represents a typical concrete target in a modern urban battlefield [19]. The specifications of the Full Scale DLRC target are shown in Figure 6.
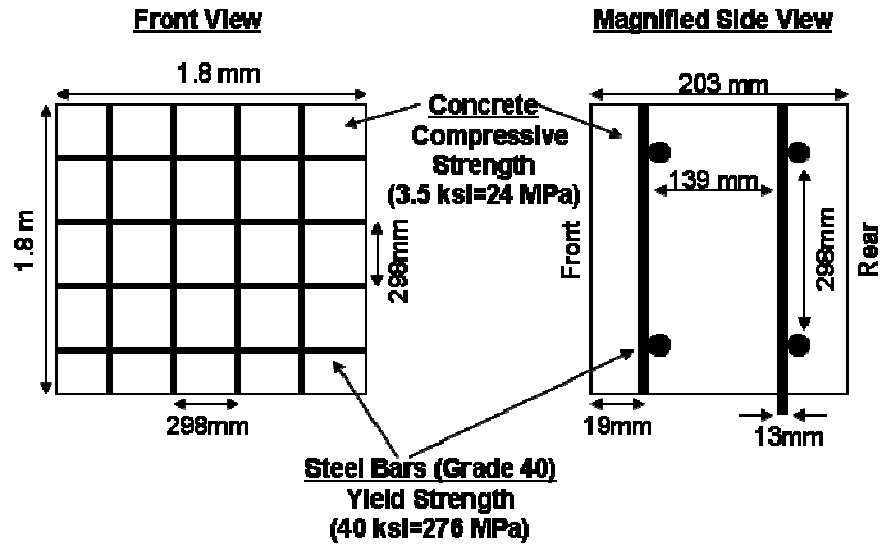
Figure 6.   Full Scale DRLC Target Diagram

The orthogonal reinforcement geometry in the DLRC target is not suited for the AUTODYN 2D axial-symmetric modeling domain. After consultation with my primary ballistics advisor, I modified the orthogonal structure into circular reinforcements [24]. I also decided to change the reinforcement material from Grade 40 to 4340 Steel. The motivation for this change came from the absence of Grade 40 steel as a selectable material in the AUTODYN Material's Library [25]. I increase the compressive strength of the DLRC to 34 MPa because that value better represents a concrete barrier that is designed to resists projectile penetration. As with the RHA target, I made the diameter of the modified DLRC target significantly larger than the diameter of the impacting design projectile. This minimizes any radial expansion of the simulated target and properly reflects a larger wall surface. The modified target is shown in Figure 7.

Front View

Side View

13mm

290 mm

400mm

Concrete
Compressive
Strength
(4.9 ksi = 34 MPa)

Direction of Impact

(Normal Incidence)

Steel Bars (Steel 4340)
Yield Strength
(141 ksi = 972 MPa)

200mm

400mm

139mm

20mm

Figure 7.   Modified DLRC Target Diagram
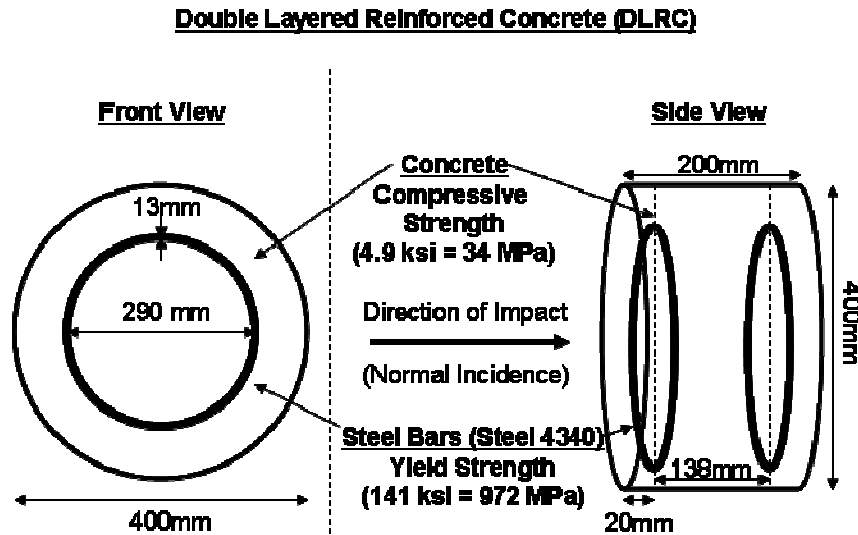
I selected a maximum range to target of 500 m in order to represent a realistic engagement situation within an urban environment. If we compare the impact velocities that I used in the RHA analysis against those used for DLRC then we will find larger velocities for the concrete impacts. This difference comes from my estimate of impact velocities. I made these estimates by using an aerodynamic drag analysis, which I discuss later in this report (See Chapter III, Section F).

D.   THEORETICAL PREDICTIONS FOR IMPACTS INTO RHA

I used the velocity ballistic limit model to estimate minimum penetration velocities for both design projectiles into 100 mm of RHA. My estimates for the maximum allowable impact velocities are based upon constraints from my aerodynamic drag analysis (See Chapter III, Section F, and Table 9). The existence of known impact velocities enables one to compare these values against the ballistic limit and to simultaneously evaluate residual velocities after impact. The velocity ballistic limit model predicts that only the 40mm design projectile can penetrate the 100mm RHA target. The success of at least one of the proposed projectiles demonstrates a need for validation using comparable theoretical techniques or computer model simulations.

A scientist by the name of *de Marre* proposed the first version of the ballistic limit formula in 1886. He assumed that there was a physical relationship between the limit energy of an impacting projectile and the amount of target volume that it displaces.

17

The limit energy is the minimum kinetic energy of a penetrating projectile [20]. Although the formula that *de Marre* proposed was dimensionally awkward, its underlying assumption is that twice the limit energy is proportional to the perforation volume in the target. We can better examine this relationship in the following expression: $MV^2 \propto TD^2$; where M is the mass of the projectile, V is the limit velocity, T is the target thickness, and D is the projectile's characteristic diameter [20]. Throughout the early 20th century, several theorists and ballistics experts refined the original formula into the modern velocity ballistic limit model. They also used a semi-empirical momentum relationship between the penetrator and the ejected target material to devise a residual velocity relationship [20]. The residual velocity relationship makes estimates from the input parameters and the results of the velocity ballistic limit. Figure 8 shows a summary of the entire velocity ballistic limit model.

Velocity Ballistic Limit

$$V_l = \sqrt{\alpha \left[\frac{L}{D}\right]^c f(z)\frac{D^3}{M}}$$

Residual Velocity

$$V_r = \begin{cases} 0 : \left[V_s \le V_l\right] \\ a(V_s^p - V_l^p)^{1/p} : \left[V_s > V_l\right] \end{cases}$$

Parameter Functions

$$f(z) = z + e^{-z} - 1$$

$$z = \frac{T}{D}\sec^k(\theta)$$

$$M' = \rho_T \pi D^3 z / 4$$

$$a = \frac{M}{M + M'/3}$$

$$p = 2 + z/3$$

Description and Units

V_l = limit velocity [m / s]
V_r = residual velocity [m / s]
α = (4000)^2 for RHA targets
L = length of penetrator [cm]
D = diameter of penetrator [cm]
c = 0.3; for long rod penetrators
k = 0.75; for long rod penetrators
M = mass of penetrator [g]
T = target thickness [cm]
θ = obliquity angle [deg]
M' = projected impact mass of target, prior to impact [g]
ρ_T = density of target, 7.85 for RHA [g / cc]

Figure 8.   Velocity Ballistic Limit Model

There are several constraints that one must consider in order to properly use the velocity ballistic limit. The parameters *c* and *k*, listed in Figure 8, are only well defined for specific long-rod penetrators and target thicknesses. A researcher by the name of

Lambert empirically derived these parameters from an experimental data base of 200 impacts involving penetrators with the following characteristics: mass between 0.5 and 3630 grams; Length to Diameter (L/D) ratio between 4 and 30; impact obliquity angle between 0 and 60 degrees, and material density between 7.8 and 19 g/cc. The target thickness in Lambert's limit-velocity database was between 0.6 and 15 cm [20]. Ballistic experts who have analyzed Lambert's parameters against his database believe that the ratio of target thickness, T, to penetrator diameter, D, must satisfy the following relationship: $T/D > 1.5$. They have further added the following general constraints to the geometry and configuration of the penetrator. It should have a right-circular cylindrical body with a conical, hemi-spherical, or flat nose. There should be obvious values for the diameter, length and mass. If geometries are approximately cylindrical then one can use effective values to estimate the characteristic diameter, length and mass [20]. The 30mm and 40mm design projectiles and the 100mm RHA target fit all of the constraints listed above, and one should have confidence in the reliability of limit-velocity estimates for this design.

In order to gain a higher level of confidence in the velocity ballistic limit, I tested the formula against one set of external data that also fit within the aforementioned restrictions for penetrator and target dimensions. This experimental data comes from the 1971 Graberek database [21]. I searched for an experimental data point that gave the best match to the type of RHA impact in my design. The closest data point was a 20 gram tungsten penetrator, with a 4 mm diameter and an L/D ratio of 20, impacting a 50mm RHA target. The experimental impact was at normal incidence, and the reported limit velocity was 1260 m/s. Given these specifications and results, I solved explicitly for the parameter α, which for RHA should be $(4000)^2$. My result for α is $(4057)^2$. This gives a percent error of 1.4 %. There were no other similar data points in Garabrek's database. I assume that this agreement with external data further validates the reliability of the velocity ballistic limit formula.

I applied the velocity ballistic limit model to an impact involving the modified penetrator, MOD-1, and the 100mm RHA target. Given the input parameters for MOD-1 and the RHA target, I calculated limit velocities of 1028 m/s and 844 m/s for the

respective 30mm and 40mm design projectiles. My aerodynamic analysis imposed a launch velocity constraint of 1100 m/s (See Chapter III, Section D). The impact velocities for the 30mm and 40mm projectiles based upon in-flight velocity reduction due to drag is discussed in the aerodynamics section (See Chapter III, Section F, and Table 9). An examination of these impact velocities shows that the 30mm projectile's limit velocity is higher than the aerodynamically calculated impact velocity; whereas, the 40mm projectile's limit velocity is lower. Therefore, the velocity ballistic limit model predicts that only the 40mm projectile will penetrate the RHA target. Using the impact velocity and the remaining portion of the model, I calculate a 413 m/s residual velocity after penetration for the 40mm projectile. The results from the velocity ballistic limit model require further validation through a comparable theoretical method or computer model simulation. The input parameters for the model and results are given in Table 1.

Variable	Units	Description	30mm Projectile	40mm Projectile
L	cm	Length of MOD-1	15	20
D	cm	Diameter of MOD-1	2.90	3.88
M	g	Mass of MOD-1	1497	3549
T	cm	Thickness of RHA Target	10	10
θ	deg	Obliquity Impact Angle	0	0
z	-----	V_L & V_r Parameter	3.45	2.57
$f(z)$	-----	V_L Parameter	2.48	1.65
V_L	m/s	Calculated Limit Velocity	1028	844
V_s	m/s	Estimated Impact Velocity	828	890
M'	g	Mass of Ejected Target	519	926
a	-----	V_r Parameter	0.90	0.92
p	-----	V_r Parameter	3.15	2.86
V_r	m/s	Calculated Residual Velocity	0	413

Table 1.   Penetration Estimates for Projectile Impact into RHA

E.   THEORETICAL PREDICTIONS FOR IMPACTS INTO DLRC

The modified-NDRC's concrete penetration, scabbing, and perforation formulas are the primary analytical methods that I use to estimate ballistic effects in the DLRC target. The results of the NDRC formulas predict penetration, scabbing and perforation for impacts involving both design projectiles and the 200mm DLRC target.

In the last half of the 20th century, before the use of finite element computer codes, ballistic researchers developed empirical formulas to estimate military ballistic effects against reinforced concrete. There are multiple empirical formulas that estimate penetration depths and perforation diameters from the normal impact of solid cylindrical projectiles against light to moderately reinforced concrete targets [22]. Researchers have conducted critical comparisons of the penetration formulas as recent as 2001. A research report in the International Journal of Impact Engineering states that the modified-NDRC penetration formula gives the best agreement with experimental data over a broad range of projectile geometries and impact velocities up to 1 km/s [23]. American military researchers originally developed the NDRC scabbing and perforation formulas from an experimental database that included high velocity impacts of steel cylindrical missiles, with diameters of between 39 mm and 155 mm into reinforced concrete with *T/D* ratios between 3 and 18 [22]. Ballistics experts restrict the use of the NDRC formulas to the following impact parameters: impact velocities greater than 152 m/s, the impacting projectile is non-rotating, and impacts are at normal incidence. The proposed impacts of the 30mm and 40mm railgun projectiles into the 200mm DLRC target approximately fit the parameter range that the NDRC used to develop its formulas and also meet the impact parameter restrictions just mentioned. Therefore, one should have confidence in any predictive estimates from the application of the NDRC formulas in this design. The modified-NDRC formulas for penetration, scabbing and perforation are show in Figure 9.

Modified-NDRC Penetration

$$x = \frac{180NW}{\sqrt{f_c}}\left(\frac{V}{1000d}\right)^{1.8} + d \qquad \left\{\frac{x}{d} > 2\right\}$$

Modified-NDRC Scabbing

$$t_s = 2.12d + 1.36x \qquad \left\{0.65 \le \frac{x}{d} \le 13.5\right\}$$

Modified-NDRC Perforation

$$t_p = 1.32d + 1.24x \qquad \left\{1.35 \le \frac{x}{d} \le 13.5\right\}$$

Description and Units

x = penetration depth [inch]
d = projectile diameter [inch]
N = nose shape factor;
     = 1.4 for very sharp noses
W = projectile weight [lbs]
V = impact velocity [ft/s]
f_c = concrete compressive
     strength [psi]
t_s = concrete thickness to resist
     scabbing [inch]
t_p = concrete thickness to resist
     perforation [inch]

Figure 9.   Modified-NDRC Formulas (British Units)

American military researchers developed the NDRC formulas in order to estimate required concrete thickness to prevent penetration, scabbing and perforation from ballistic missiles. I use these formulas to show that the proposed 30mm and 40mm railgun projectiles can penetrate and produce scabbing and perforation on the 200mm DLRC target. If we apply the input parameters from MOD-1 projectile, for impact velocities that I calculated in my aerodynamic analysis, then we can calculate the required thickness of the DLRC target to prevent penetration, scabbing, and perforation. Table 2 shows the input parameters for the NDRC formulas and the resulting concrete thickness needed to prevent penetration, scabbing and perforation. All of the calculated concrete thicknesses are at least eight times the thickness of the 8 inch or 200 mm DLRC target. The required thickness to prevent scabbing and perforation are larger than the required thickness to prevent penetration. The expectation of needing larger concrete thickness to prevent scabbing or perforation, given that the projectile does not penetrate, comes from shock wave and shear concrete plug pushed forward by the impacting projectile. The combination of the shock wave and concrete plug can create scabbing and perforation even though a projectile does not completely penetrate. The results of the NDRC formulas predict that both design projectiles will penetrate and produce scabbing and perforation on the DLRC target.

Variable	Description	30 mm Projectile		40 mm Projectile	
		Metric	*British*	*Metric*	*British*
d	Diameter of MOD-1	29 mm	1.14 in	38.8 mm	1.53 in
V	Impact Velocity	1024 m/s	3359 ft/s	1043 m/s	3421 ft/s
W	Weight of MOD-1	1497 g	3.29 lbs	3549 g	7.81 lbs
N	Nose Shape Factor	1.14	1.14	1.14	1.14
fc	Compressive Strength DLRC	34 MPa	4900 psi	34 MPa	4900 psi
x	DLRC Thickness to Prevent Penetration	1742 mm	68.6 in	2514 mm	99.0 in
ts	DLRC Thickness to Prevent Scabbing	2431 mm	95.7 in	3502 mm	137.9 in
tp	DLRC Thickness to Prevent Perforation	2199 mm	86.6 in	3169 mm	124.8 in

Table 2.   Input Parameters and NDRC Results

Although reinforcement does not explicitly appear as an input parameter in the NDRC formulas, these formulas inherently consider concrete reinforcement in their calculations. The NDRC developed its formulas from experimental data using non-deformable solid cylindrical projectiles against light to moderate reinforced concrete targets. The modified-NDRC goes one step closer to a semi-empirical formula by including the compressive strength of concrete, fc, which the original formula did not do until its modification in 1966. A researcher that is associated with the American Society of Civil Engineers (ASCE) evaluated the NDRC formulas for their lack of specificity with regard to the amount of concrete reinforcement. He concluded, from the analysis of experimental data, that the amount of reinforcement is a negligible concern unless the projectile diameter is equivalent to the reinforcement bar spacing [22]. Ballistic experts generally accept the fact that steel reinforcement within concrete serves to maintain structural integrity after impacts or explosions. Heavy reinforcement may restrict the perforation hole to the diameter of the impacting projectile. Reinforcement bars are not designed to prevent penetration [19]. Both design projectiles have significantly smaller diameters than the bar spacing of the DLRC target. From the conclusions of the report from the ASCE, one should be able to neglect the amount of reinforcement when considering NDRC estimates in this design. The fact that the 200mm DLRC target has heavy reinforcement suggests that the impacting 30mm and 40mm design projectiles will create holes in the concrete that are slightly larger than their primary diameters.

F. BALLISTIC MODELING

In order to refine or validate my theoretical estimates, I simulated the design projectiles impacting into the RHA and DLRC targets at their calculated impact velocities. I used the AUTODYN version 5.0 interactive non-linear dynamic analysis software for all simulations [25]. The AUTODYN program offers planar or axial symmetric coordinates in two or three dimensions. It also allows the user to choose between Eulerian or Lagrangian reference frames, each with their own advantages or disadvantages to a particular model. The equation of state that a user chooses to represent materials in the modeling domain is an important consideration. Given the sub-hydrodynamic impact scenarios of solid cylindrical tungsten projectiles approaching their solid targets at normal incidence, with expected deformation of both projectile and target

during impact, I choose to operate the AUTODYN simulation in a Lagrange, 2D axial symmetric coordinate system with linear equations of state for materials.

The normal incidence direction of impact and the inherent axial symmetry of the projectile allows for 2D axial-symmetry. The only problem with this coordinate system, as it applies to the proposed impact scenarios, is for the original DLRC target. The modification of the DLRC target into an axial symmetry representation was a necessary but reasonable change. AUTODYN allows users to map the 2D axial symmetric solution onto a circular three dimensional (3D) representation of the impact scenario. Although this is a computational shortcut, it adequately represents the 3D interactions of materials in computer simulation models.

The Lagrange reference frame follows the interaction of each mass particle in the modeling simulation. The Euler reference frame calculates the flow of mass through static cells. It is important to follow the interaction of individual mass particles for sub-hydrodynamic or less than 3 km/s impacts. In this impact regime, mass particles remain solid and respond to interaction based upon elastic or plastic response patterns. Solid materials respond in a plastic or deformable manner within the shock front created by a high velocity impact. The AUTODYN equations that calculate interaction, based upon the Lagrange reference frame, ensure the conservation of mass, momentum, and energy. AUTODYN's ability to ensure these conditions are met, while allowing each particle to deform, creates the most realistic modeling simulation for this design.

When a mass particle is allowed to deform, it is important to consider the zoning that one applies to mass particles. The amount of zoning that one chooses directly influences computational memory and the time steps taken by a computer simulation. In all simulations, the zoning was set to two cells per unit millimeter. Therefore, one square millimeter had four zones. This zoning was applied to the entire model except for the nose cone of the projectile. The base of the projectile was set to two zones per unit millimeter. However, the zoning increased towards the tip of the nose. The type of geometry that AUTODYN allowed for a triangular configuration set the structure of the zoning in the nose. Given the high level of deformation that a nose cone experiences

during impact, the AUTODYN zoning in the projectile's nose was both reasonable and necessary.

The equation of state that one chooses for materials is also a selectable modeling characteristic, and needs to properly represent the range of interactions within a particular model. The equations of states for all materials were linear Von Mises, except for the concrete and the steel reinforcement bars. The linear Von Mises model evaluates mass particles for any violation of their material-specific ultimate yield stress. If the model finds a violation of the Von Mises yield criterion, it linearly adjusts cells to satisfy appropriate boundary conditions [25]. The proper equation of state for the concrete is one that represents a porous material.   This is a selectable equation of state in AUTODYN [25]. The 4340 steel that I used to represent the reinforcement material had a default linear Johnson-Cook model. This model allows a simulation to calculate the effects of compression with temperature. Since the reinforcement bars did not interact directly with the impacting projectiles, their equation of state was not an important design parameter. The default Johnson-Cook model was adequate. Overall, the materials in RHA and DLRC simulations start out as solid and remain solid. Their response to pressure and physical interaction is either elastic or plastic based upon their proximity to the shock front created by the impact.

When using the AUTODYN modeling software, users most consider the effects of reference frames and material interactions. I ensured that the impact scenarios between the tungsten penetrator and both the RHA and the DLRC targets were setup to reflect the proper interaction of mass particles. A summary of the program set-up for each impact scenario is listed in the appendix (See Appendix D).

1.   AUTODYN Simulation of MOD-2 Impacting into RHA

I executed individual AUTODYN modeling simulations to predict the ballistic effects of the 30mm and 40mm design projectiles impacting into the 100mm RHA target. AUTODYN's 2D axial symmetrical modeling domain required the use of projectile modification MOD-2 for each projectile. I did not change the specification of the 100mm RHA target that I previously identified in the Targets section.   The 30mm and 40mm MOD-2 projectiles impacted the RHA target at their respective impact velocities of 828 m/s and 890 m/s. The results of the modeling simulations predict that both MOD-2

projectiles will perforate the RHA target. The residual velocities of the 30mm and 40mm projectiles are 758 m/s and 847 m/s, respectively.

The AUTODYN results for the 30mm projectile differ significantly from the estimate of the velocity ballistic limit, which predicts no penetration or residual velocity. The result for the 40mm projectile agrees with penetration prediction of the velocity ballistic limit. The AUTODYN residual velocity prediction for the 40mm projectile is over two times larger than the 413 m/s estimate of the velocity ballistic limit. The disagreement between the AUTODYN models and the velocity ballistic limit estimates requires further theoretical or experimental analysis. The velocity plots and final graphical images of the two impacts are shown in Figures 10-13, under the subsections for each projectile.

a.   *30mm MOD-2 Impact into RHA*
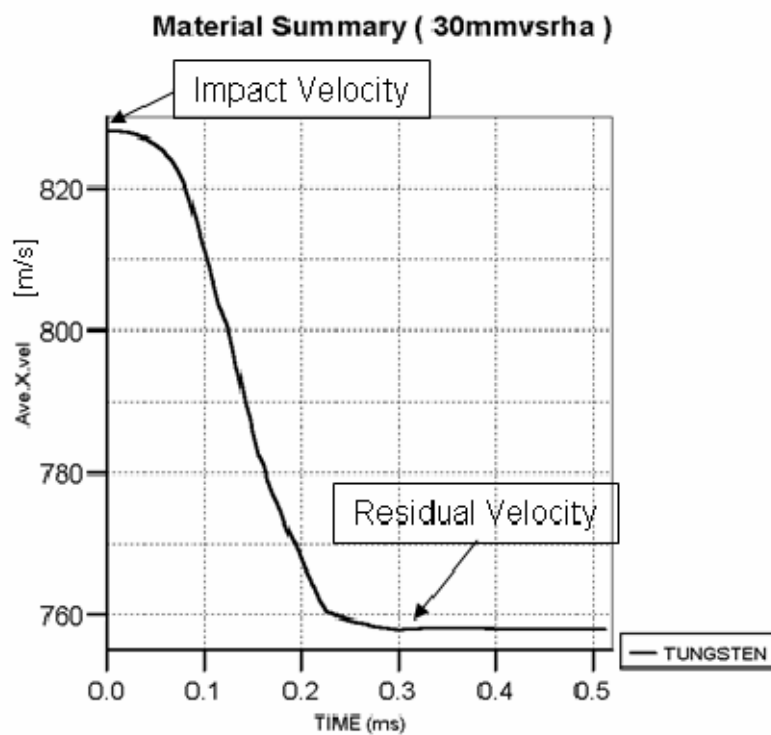
Figure 10.   Simulation Velocity of 30mm Projectile During Impact with RHA Target
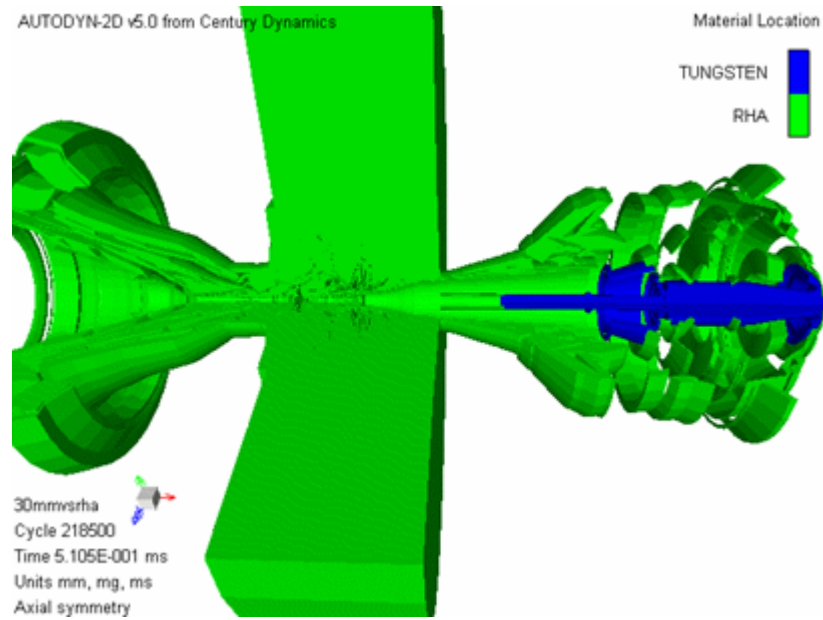
Figure 11.   Simulation Image of Projectile and RHA Target 5 ms After Impact

b.   *40mm MOD-2 Impact into RHA*
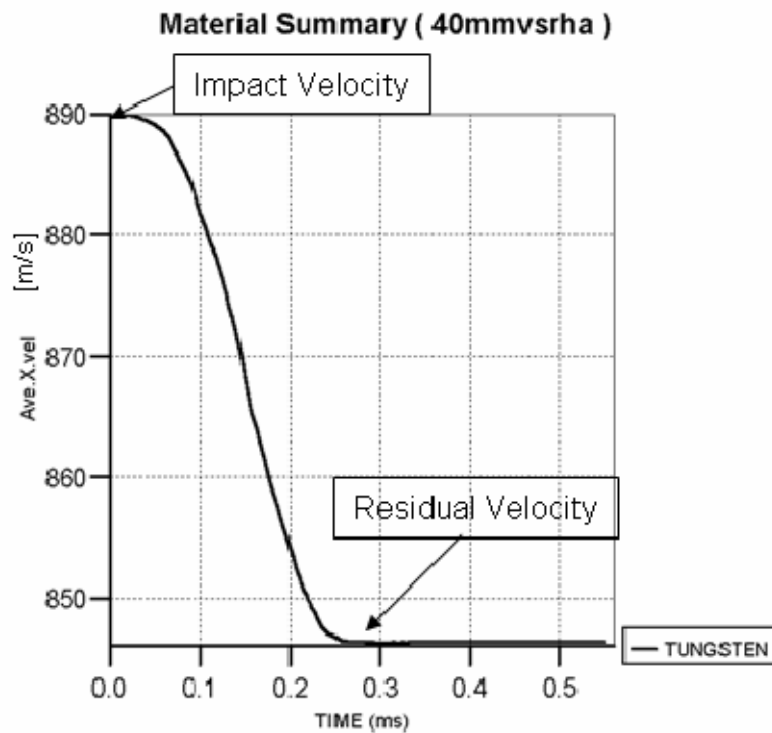
Figure 12.   Simulation Velocity of 40mm Projectile During Impact with RHA Target
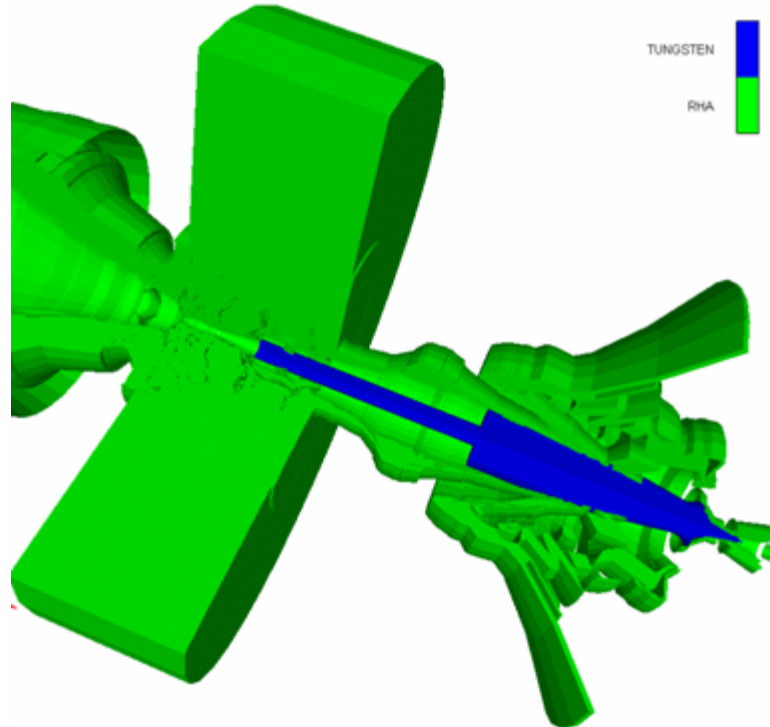
Figure 13.   Simulation Image of Projectile and RHA Target 4 ms After Impact

2.   AUTODYN Simulations of MOD-2 Impacting into DLRC

Using the AUTODYN finite element software, I simulated the individual impacts of the 30mm and 40mm design projectiles against the 200mm DLRC target.   The 2D axial symmetrical modeling domain within AUTODYN required the use of projectile modification MOD-2 for each projectile.   The original DLRC target that I previously specified in the Targets section required a modification into a proportionate 2D axial symmetric geometry.   The modified DLRC target is also discussed and graphically represented in the Targets section.   The 30mm and 40mm MOD-2 projectiles impacted the DLRC target at their respective impact velocities of 1024 m/s and 1043 m/s.   The results of the modeling simulations predict that both projectiles will penetrate and produce perforation and scabbing in the DLRC target.   The residual velocities of the 30mm and 40mm projectiles are 997 m/s and 1023 m/s, respectively.   However, the residual velocities have no relevance toward estimates from the modified-NDRC formulas. The graphical AUTODYN results match the predictions from the modified-NDRC formulas.   The simulations do not show the formation or backside ejection of a concrete plug.   The ratio of the length of the nose to the base diameter, or nose fineness, of each projectile is 3.4.   This is a high value for nose-fineness and causes a higher lateral

28

distribution of the normal shock front. If the noses of the projectiles were blunt then we would expect to see the formation of a concrete plug. The minimum perforation thickness in each simulation was approximately 2 mm larger than each projectile's body diameter. The NDRC formulas do not allow for a predictive estimate of this value. Therefore, one can only conclude that the minimum perforation holes created by these projectiles in DLRC will be no smaller than their primary diameters. The velocity plots and final graphical images of the two impacts are shown in Figures 14-17, under the subsections for each projectile.

a.   30mm MOD-2 Impact into DLRC
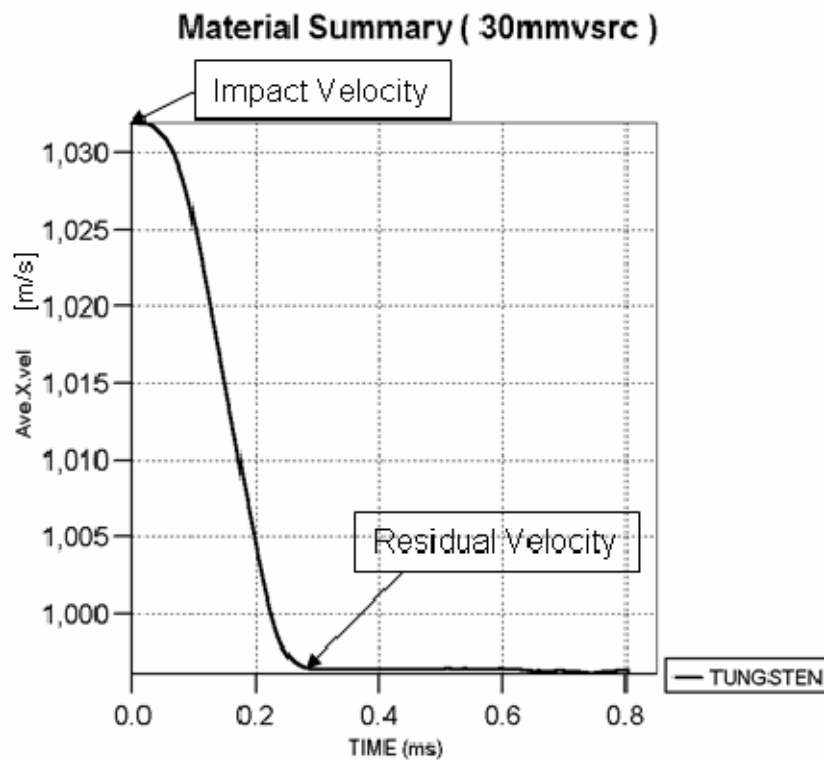
Figure 14.   Simulation Velocity of 30mm Projectile During Impact with DLRC
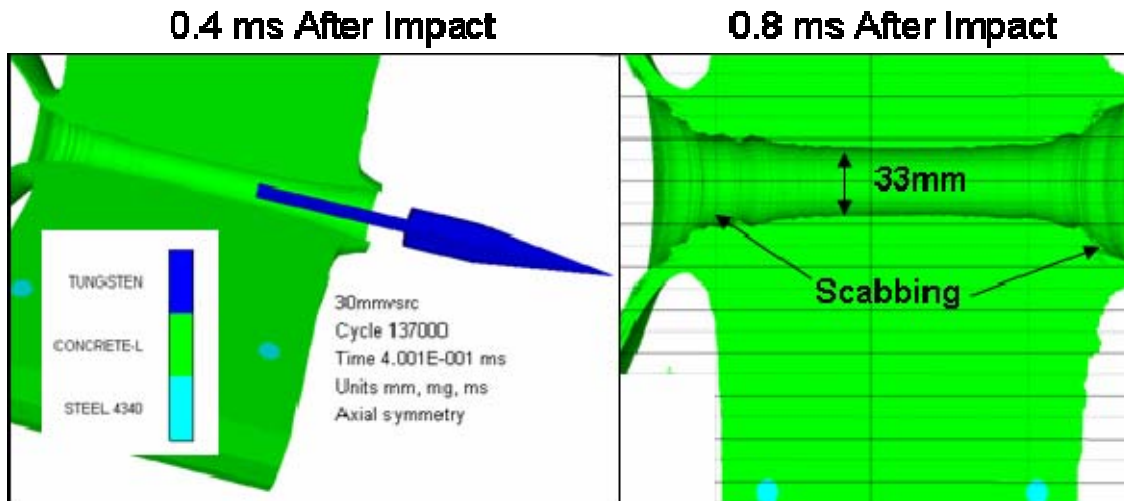
Figure 15.   Simulation Images of 30mm Projectile and DLRC Target

b.   *40mm MOD-2 Impact into DLRC*
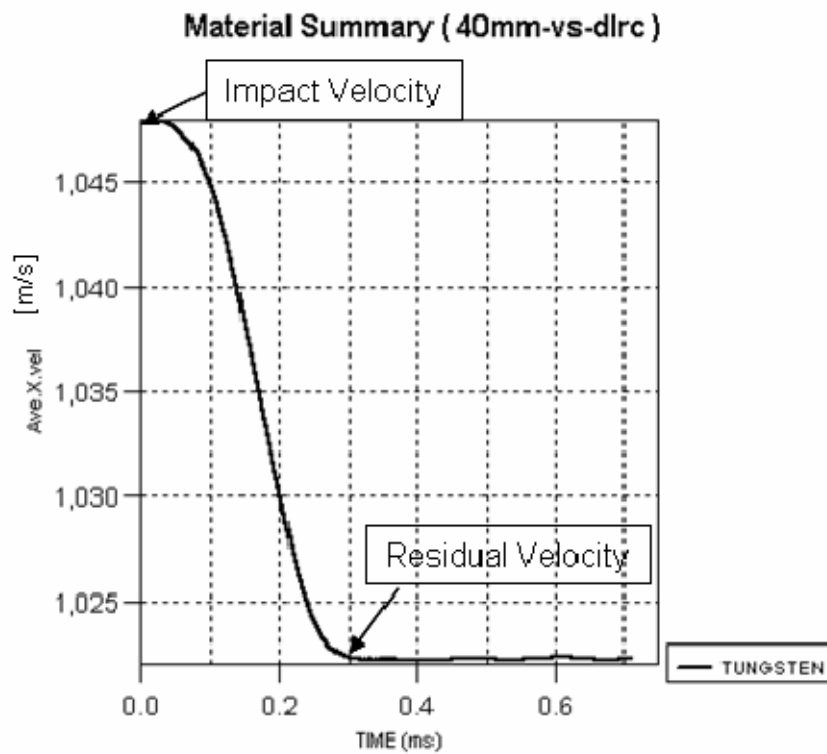
Figure 16.   Simulation Velocity of 40mm Projectile During Impact with DLRC
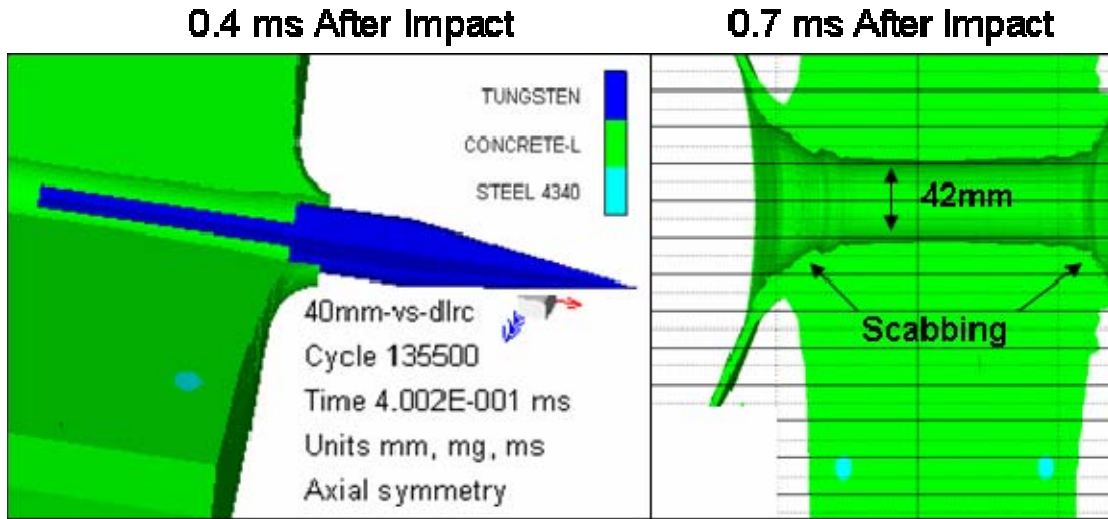
Figure 17.   Simulation Images of 40mm Projectile and DLRC Target

G.   CRITICAL ANALYSIS

The disagreement between the RHA impact estimates of the velocity ballistic limit and the results of the AUTODYN simulation required that I make further investigations into either theory or modeling. A variant of the Tate Model, called critical analysis, fit the sub-hydrodynamic impact scenario of a rod penetrator traveling at less than 3 km/s into a solid metal target [26].   The theoretical foundations of the Tate Model come from the pressure balance equation at the stagnation point between an impacting projectile and the target, as shown in Figure 18. Furthermore, this model assumes that the elastic response regions of both the projectile and target material provide residual strength to counter deformation. A physical description of this equation is shown in Figure 18.
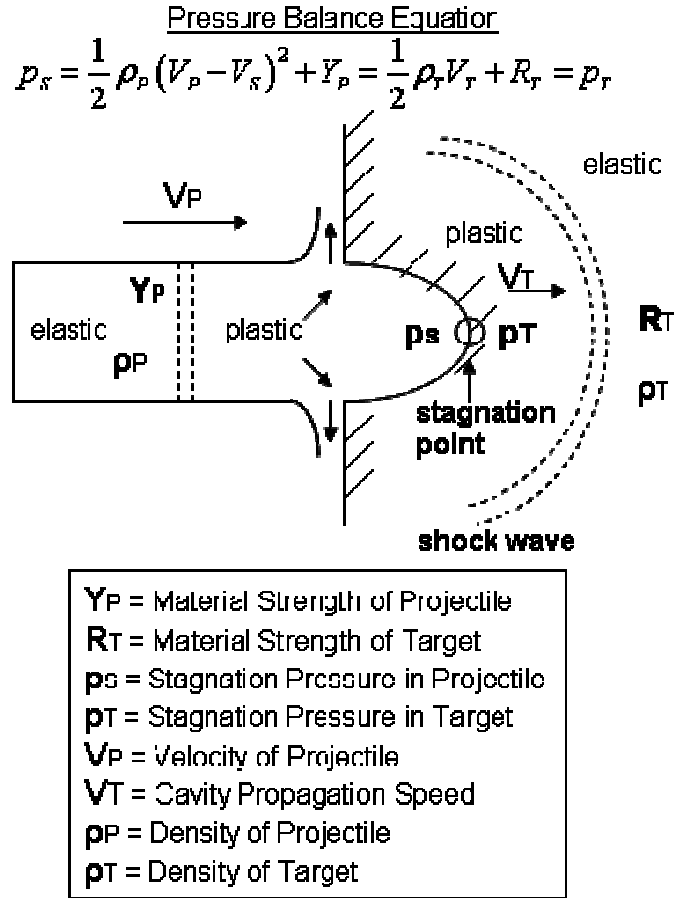
Figure 18.   Sub-hydrodynamic Penetration Model

The Tate Model assumes that the velocity of the projectile does not significantly change during penetration. Specifically, it assumes that difference between the velocity of the projectile and the cavity propagation speed is a constant for a penetrator that has a relatively small longitudinal shock wave velocity. The critical analysis method diverges from the Tate Model in that it assumes the projectile's velocity changes during impact. It focuses calculation around a critical velocity, V_C. This is the point in the impact where the velocity of the projectile, V_P, equals the cavity propagation speed, V_T.   One can apply this method to two different impact scenarios in which the material strength of the projectile is either greater than or less than the material strength of the target. Applying the critical analysis method to the impact of a tungsten projectile, with a material strength of $Y_P = 1.51$ GPa, against a RHA target, with a material strength of $R_T = 1.32$ GPa, the appropriate case is where the strength of the projectile is greater than the strength of the target, $Y_P > R_T$ [26], [27].

Given the situation in which the strength of the projectile is greater than the strength of the target, one can solve for the cavity propagation speed, V_T. The analytical expression for the cavity propagation speed is complicated, and I have decided to reference it and further important relationships in the appendix (See Appendix D). As I stated earlier, the projectile's critical velocity is approximately the cavity propagation speed. One can develop a relationship for the penetration depth per length, $P(V_C)/L$, of the projectile for the portion of the impact where the projectile's velocity is greater than the critical velocity. When the projectile is less than the critical velocity, we can assume that it continues to penetrate the target as a rigid projectile with depth P_{rigid}/L. For rigid projectile penetration, the projectile continues to slow down until it either passes through the target or reaches a velocity of zero. One can calculate the total penetration depth by summing the both components of the penetration per unit length of the projectile, $\frac{P_{tot}}{L} = \frac{P(V_C)}{L} + \frac{P_{rigid}}{L}$ [26]. Again, the relationships and equation manipulations for this analysis are complicated and left to the appendix (See Appendix D).

The results of the critical analysis for both the 30mm and 40mm design projectiles impacting the RHA target indicate a successful penetration for each impact scenario. The total penetration depth of the 30mm projectile is 1.24 times the projectile length. The total length of the nose and major body cylinder of the 30mm projectile is 150 mm. If one includes the rod cylinder then the total length is 261 mm. It is important to analyze just the nose and major body cylinder because these aspects of the projectile have the largest characteristic diameter. If they do not have enough length to penetrate the RHA target then it is likely that they will plug the impact path and not allow the smaller diameter rod cylinder to continue penetrating. Considering just the nose and major body cylinder of the projectile, the total penetration depth is estimated to be 186 mm, which is greater than the 100 mm thickness of the RHA target. The calculated penetration depth of the 40mm projectile is 1.3 times its length. Again, considering the total length of the nose and major body cylinder which is 200 mm, then one should calculate a total penetration depth of 260 mm. This is significantly larger than the thickness of the RHA target.

Although the critical analysis does not yield a comparative limit velocity, it does indicate that the projectiles have enough length to successfully penetrate the 100mm RHA target. An implied conclusion from the critical analysis is that both projectiles will have a significant residual velocity. One can only approximate the residual velocity by assuming that it is close to the cavity propagation speed. This value is 523 m/s for the 30mm projectile and 562 m/s for the 40mm projectile. Assuming that the cavity propagation speeds represent the residual velocities from the critical analysis, we can compare them to the AUTODYN predictions of 758 m/s and 847 m/s for the respective 30mm and 40mm design projectiles. The percent difference for the 30mm projectile is 31% and for the 40mm projectile it is 33.5%. Overall, the critical analysis gives better agreement with the AUTODYN simulation for RHA impact, than does the velocity ballistic limit

H. CONCLUSIONS OF BALLISTIC EFFECTS

The multilevel ballistics analysis in this thesis shows that both design projectiles can successfully perforate the 100mm RHA target and the 200mm DLRC target. These results meet or exceed the ballistic design expectations of the railgun projectiles. The minimum expectation for the RHA target was penetration, and both projectiles clearly perforate it. An IFV projectile that is able to perforate 100mm of RHA at 2 km is at the forefront of other similar caliber armor piercing projectiles. Based upon the AUTODYN simulations for reinforced concrete impacts, the design projectiles will create perforation holes no smaller than their primary diameters. The primary diameters of the design projectiles are larger than the maximum primary diameters of American IFV armor piercing projectiles, which are no greater than 10 mm.

I cannot conclude, based upon single shot perforation thicknesses, that the railgun projectile is more effective than an American IFV armor piercing projectile at creating the largest possible breach hole in concrete. The Bradley Fighting Vehicle has a sustained rate of fire of 100 rounds per minute; whereas, the railgun is only expected to achieve a rate of fire of 10 rounds per minute [11]. One would have to conduct a physical experiment between the two systems, allowing for sustained rates of fire, in order to decide which projectile had better overall perforation effect against concrete. In

conclusion, the proposed design projectiles demonstrate competitive ballistics effects against realistic Infantry battlefield targets.

THIS PAGE INTENTIONALLY LEFT BLANK

III. AERODYNAMIC STABILITY AND DRAG

A. AERODYNAMICS OVERVIEW

During the development of any unguided kinetic energy projectile, researchers must thoroughly analyze in-flight stability and drag to ensure their design meets intended trajectories and impact velocities. In the development of the projectiles for this design, I performed an aerodynamic analysis as the second step in a recursive design loop that also considered ballistic effects and electromagnetic launch. My aerodynamic analysis is purely analytical, and relies principally on methods presented in <u>Tactical Missile Design</u> by Dr. Eugene Fleeman and one of his primary references, NACA Report 1307 [28], [29]. After ensuring that my design met the constraints of the aforementioned sources, I successfully calculated and proved both pitch and yaw neutral stability with a static margin of at least two percent. Continuing to use Dr. Fleeman's analytical methods to calculate the Coefficient of Drag, C_D, I concluded my analysis by developing an equation of velocity verses flight distance for each projectile. This final equation created a continuity link between the ballistic analysis and the electromagnetic launch by equating a particular launch velocity to an impact velocity.

B. CONSTRAINTS AND ASSUMPTIONS

The approach that aerodynamic experts use for the evaluation of subsonic, transonic, and supersonic flow is different for each flow regime. My design of the Infantry Railgun Projectile is constrained to supersonic flow and to trajectories that are strictly line-of-sight. The design's lowest calculated velocity, at the limit of the furthest possible trajectory, is 828 m/s (See Table 9). Given a constant speed of sound at 343 m/s, this velocity equates to a Mach number of $M=2.4$. The highest possible velocity in the design is constrained to the launch velocity of 1100 m/s, resulting in a Mach number of $M=3.2$ (See Chapter III, Section D). The geometric shape of the design projectile is approximately a right-circular cylinder with a right-circular nose cone. The length to diameter ratio for both projectiles is approximately 11.2 ± 0.1 (See Appendix B2). Considering the geometric shape and the L/D ratio, the design projectile is a slender body, and is applicable to slender body theory [28]. My only aerodynamic wings in both

design projectiles are triangular tail fins. These fins are not banked, in a fixed position after launch, and in-line with the body axis [29]. One should consider these fins to be slender because their ratios of thickness, t, to mean aerodynamic chord, C_{MAC}, are much less than one, $t/C_{MAC} \square 1$ (See Section C.3.) [28]. The aspect ratio, A, for these fins is approximately 3.85 ± 0.02 (See Section C3). This would allows one to apply slender wing theory because the wing is thin and the aspect ratio is low or on the order of $A \approx 3$. A problem with the application of slender wing theory is that it is only relevant for Mach numbers less than 1.53. The more appropriate theory is linear wing plus Newtonian impact theory. The constraint of this theory is satisfied by the following relationship: $M > \sqrt{1+(8/\pi A)^2}$; where M is the Mach number and A is the aspect ratio [29]. Evaluating the right hand side of the argument, one should find a value of 1.2, which is lower than the minimum design Mach number of 2.4. From the discussion above, one can realistically constrain the aerodynamic analysis to slender body theory and linear wing plus Newtonian impact theory in the limit of the supersonic flow.

Throughout the aerodynamic analysis, I had to make certain assumptions about the performance of the design projectile. For instance, while the projectile is in the electromagnetic launcher, its tail fins are folded inside the body. One must assume that these fins reliably deploy upon launch and lock into position. Although this design includes possible geometries and locations of fin-deployment pistons, I have intentionally emitted discussion of reliable deployment mechanisms. I also assume that the projectile does not roll upon launch or during flight. Although the current tail configuration is prone to an unstable rolling moment derivative, I would have to perform a wind-tunnel test or simulate the projectile in a finite element model to accurately analyze the rolling moment [28]. Taking a simplistic approach, I assume that the railgun does not impart spin to the projectile during launch, and that the projectile continues to travel to its target without any roll. One should consider these reasonable, but simplistic, assumptions given the vertical and horizontal plane symmetries of the railgun projectile. Since aerodynamic flow is symmetric in each of these planes, the appropriate stability fins can act in their respective planes to counter the nose-body normal force. The last assumption that one needs to make is that flow interference between the body cylinder and tail fins,

as well as between the yaw fins and the pitch fins, has no significant impact on stability calculations. In Tactical Missile Design, Dr. Fleeman states that for conceptual design analysis it is reasonable to isolate the normal force of distinct geometries on the projectile [28]. Although he agrees that interference calculations are needed for a more thorough analysis, he states that in conceptual design one can assume wing-body or wing-wing interferences are small compared to the effective normal force of the isolated geometries [28]. Overall, the assumptions that I discuss above are appropriate and necessary for the concept-level of analysis that I performed in this research.

C. AERODYNAMIC STABILITY PARAMETERS

In order to analyze pitch and yaw stability for the design projectile, I had to first calculate several aerodynamic parameters from the geometric specifications of my design. The theoretical development and specification of these parameters are found in Tactical Missile Design by Dr. Eugene Fleeman [28]. A secondary reference which Dr. Fleeman cites and that I also use is "NACA Report 1307" [29].

1. General Body Parameters

a. Surface Reference Area

The reference surface area, S_{REF}, of an aerodynamic body is the cross sectional area with respect to flow. For the case of a long rod projectile that has a cylindrical geometry with diameter D, the reference surface area is: $S_{REF} = \pi D^2/4$. For cylindrical geometries, the reference surface area is also the reference body area ($S_{REF} = S_{BODY}$). The design projectile falls into the category of a right circular cylinder, with the exception of its shaved sides. In Figure 19, one can find the geometric relationships needed to account for the exact cross section area of the design projectile. The areas denoted by A1 and A2 are exactly equal and represent the missing cross-sectional area due to the projectile's shaved sides. The parameter D1 is the primary body diameter of the projectile. Parameters W1 and W2 represent the body width and height with respect to the projectile's shaved sides. I have specified the measurements of parameters D1, W1, and W2 for each projectile in the Appendix (See Appendix B2). Using the relationships for the reference area described under the Figure 19, I calculated

the following surface reference areas for the two projectiles: $S_{REF}(30mm) = 665.5mm^2$ and $S_{REF}(40mm) = 1183.0mm^2$.

Design Projectile's Body Cross-section
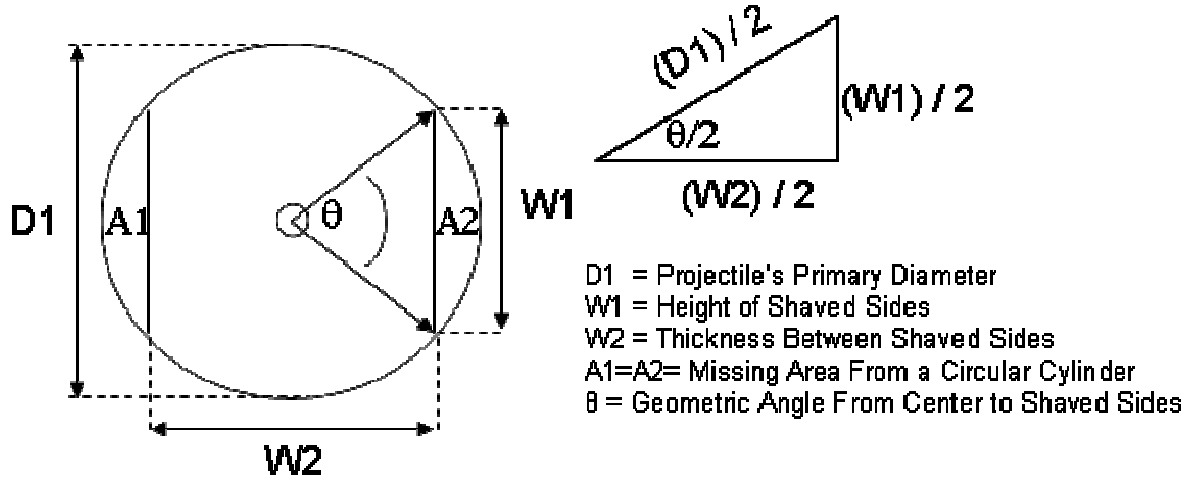
Figure 19.   Surface Reference Area

$$S_{REF} = \frac{\pi}{4}D_1^2 - (A_1 + A_2) = \frac{\pi}{4}D_1^2 - 2A_2$$

$$A_1 = A_2 = \frac{1}{2}\left(\frac{D_1}{2}\right)^2(\theta - \sin\theta) = \frac{D_1^2}{8}(\theta - \sin\theta)$$

$$\theta = 2\arcsin\left(\frac{W_1}{2}\frac{2}{D_1}\right) = 2\arcsin\left(\frac{W_1}{D_1}\right)$$

b.   *Equivalent Diameter*

One can calculate an equivalent diameter, *d*, for the design projectiles from the surface reference area. If one assumes the surface reference area represents a perfect circle, then the following relationship is true: $S_{REF} = \pi d^2/4$. Solving for the equivalent diameter, *d*, I calculated the following equivalent diameters for each projectile: *d(30mm)* = 29.0 mm and *d(40mm)* = 38.8 mm.

c.   *Reference Chord and Center of Gravity*

The reference chord length, $\bar{c}$, is the mean geometric centerline that runs from the nose tip to the base of the projectile. The two projectiles have the following reference chord lengths: $\bar{c}(30mm) = 325mm$ and $\bar{c}(40mm) = 433mm$ (See Appendix B2).

40

The center of gravity for each projectile is $\overline{X}_{CG}(30mm) = 139.7mm$ and $\overline{X}_{CG}(40mm)$ $= 186.2mm$ (See Appendix B7).

2. Nose-Body Parameters

The nose cone of a slender aerodynamic body is the primary geometry that separates the flow of air around the rest of the projectile. At supersonic speed, the shape of the nose can significantly impact the amount of energy lost to the creation of a primary Mach cone surrounding the body. The optimum aerodynamic nose shape is a perfect right circular cone that comes to a sharp point at the tip. The nose-fineness, f_N, which is the ratio of the nose length to the base diameter, L_N / d, is a parameter that represents the quality of the nose. The general rating of common nose-fineness ratios are high, medium, and low. The value of each rating is 5, 2, and 0.5 respectively. For the Infantry Railgun Projectile, where I have scaled the 40mm projectile from the 30mm projectile, the nose-fineness is 3.44. This is between medium and high nose fineness and is a good value for limiting drag-loss to the primary Mach cone. Since the nose is the most significant geometry that separates flow, it is also where the body center of pressure is located in the limit of small angles of attack. This circumstance accounts for the position of the normal lifting force on the body. Therefore, the center of pressure for the nose is also the center of pressure for the body. I describe the semi-empirical relationships for calculating the nose-body center of pressure and normal force coefficient with respect to angle of attack in the following subparagraphs.

a. Nose-Body Center of Pressure

For slender bodies with right circular nose cones, the center of pressure for low angles of attack is at least one body-diameter from the nose tip [28]. NACA Report 1307 defines a more exact relationship for the nose-body center of pressure, $(X_{CP})_N$, and is given by the following: $(X_{CP})_N = L_N \left[1 - V_N / \left(\pi r_N^2 L_N\right)\right]$, where L_N is the nose length, r_N is the radius of the nose base, and V_N is the volume of the nose [29]. For a perfect right circular nose cone, this relationship reduces to:

$$(X_{CP})_N = L_N \left[1 - \frac{1}{3}\left(\pi r_N^2 L_N\right) / \left(\pi r_N^2 L_N\right)\right] = 0.67 L_N \, .$$

Using a nose length of 100.0 mm for the 30mm projectile and 133.3 mm for the 40mm projectile, I calculated the following nose-body center of pressure for each projectile: $(X_{CP})_N[30mm] = 67.0mm$ and $(X_{CP})_N[40mm] = 89.3mm$.

b.   Nose-Body Normal Force Coefficient

The nose-body normal force coefficient that I use in stability analysis is actually called the coefficient derivative, $(C_{N\alpha})_N$, due to the angle of attack measured in radians. For slender bodies, this coefficient for the nose-body is approximately 2 per radian.   As with the center of pressure calculation, NACA Report 1307 specifies a more exact relationship.   The coefficient is related to the reference surface area and base diameter by the following: $(C_{N\alpha})_N = 2\pi r_N^2/S_{REF} = \pi d^2/2S_{REF}$.   Using this relationship, the equivalent diameter, and the surface reference area for each projectile, I calculated the following nose-body normal force coefficient derivatives: $(C_{N\alpha})_N[30mm] = 2.0[1/radian]$ and $(C_{N\alpha})_N[40mm] = 2.0[1/radian]$.

3.   Tail Fin Parameters

a.   Tail Fin Planform Area

The schematics in Figure 20 show relevant parameter specifications for the tail fins. The exact dimensions for each set of tail fins are shown in Appendix B5.
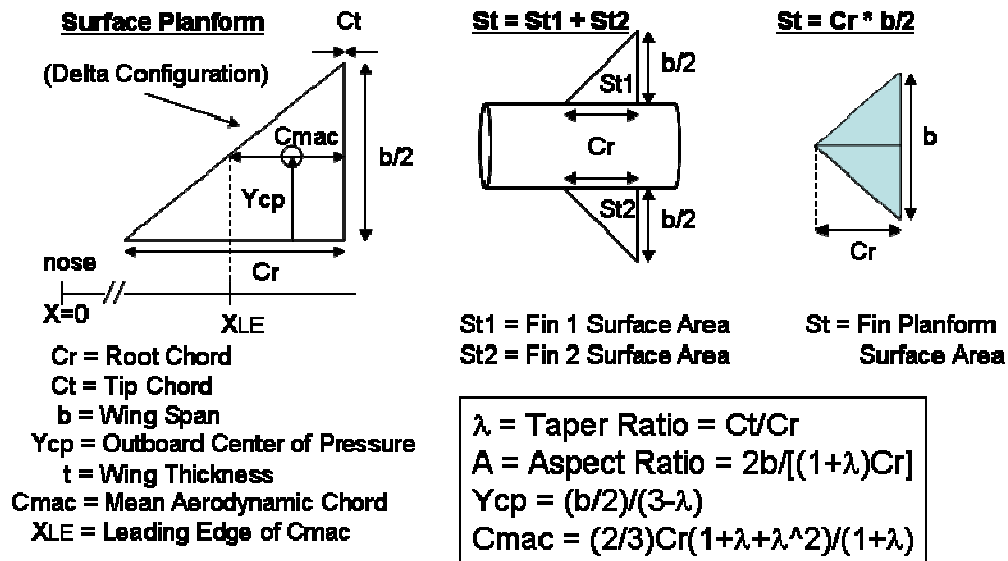
Figure 20.   Tail Fin Planform Diagram

Two axial symmetrical tail fins represent one surface planform area. Both design projectiles have one yaw fin (YF) planform and one pitch fin (PF) planform. All fins on the projectile are delta configurations. This configuration is characterized by a right triangle, with no tip chord or taper ratio ($\lambda = Ct = 0$). The following table summarizes the parameters identified in Figure 20.

Variable	Units	30mm Projectile		40mm Projectile	
		Yaw Fin	Pitch Fin	Yaw Fin	Pitch Fin
Cr	mm	26.4	22.4	35.3	30.0
b/2	mm	25.5	21.5	34.0	28.7
b	mm	51	43	68	57.4
Ycp	mm	8.5	7.17	11.3	9.57
t	mm	1.0	1.0	1.3	1.3
CMAC	mm	17.6	14.9	23.3	20.0
A	----	3.86	3.84	3.85	3.83
St1,St2	mm^2	336.6	240.8	600.0	430.5
St	mm^2	673.2	481.6	1200	861.0
XLE	mm	271.4	304.0	361.8	405.4

Table 3.   Tail Fin Planform Parameters

b.   *Tail Fin Center of Pressure*

The center of pressure for any planform varies with the Mach number, M. The Mach number is the ratio of the dynamic flow velocity to the speed of sound, $M=U/c$. The design projectile is intended to fly at low altitudes where the speed of sound is approximately 343 m/s. The dynamic flow velocity is no greater than the launch velocity of 1100 m/s. From design constraints in the electromagnetic launch, I set the launch velocity at 1100 m/s (See Chapter IV). Using a dynamic flow velocity of 1100 m/s and speed of sound of 343 m/s, I calculated a Mach number for both projectiles of $M = 3.2$.

Using linear wing theory plus Newtonian impact theory, Dr. Fleeman specifies an empirical formula to calculate a wing planform's center of pressure with respect to its mean aerodynamic chord. One can examine this empirical formula in the following equation: $(X_{CP})_{TF} = C_{MAC}(A\beta - 0.67)/(2A\beta - 1) + X_{LE}$; where A is the aspect ratio, β is $\sqrt{M^2 - 1}$, C_{MAC} is the fin's mean aerodynamic chord, and X_{LE} is the leading edge of the

C_{MAC} with respect to the nose tip [28]. Table 4 shows my calculations for each planform on both projectiles. It is important for one to note that for all calculations, β is a constant. This follows from the definition of β and the fact that I have assumed the Mach number, M, is at a constant value of 3.2. This assumption is a conservative estimate because the aerodynamic efficiency of a wing or fin decreases with increasing Mach number. If one assumes the launch velocity Mach number for all calculations involving the fin's center of pressure, then this will produce the lowest normal force coefficient for the fins.

Variable	Units	30mm Projectile		40mm Projectile	
		Yaw Fin	Pitch Fin	Yaw Fin	Pitch Fin
A	----	3.86	3.84	3.85	3.83
C$_{MAC}$	mm	17.6	14.9	23.3	20.0
X$_{LE}$	mm	271.4	304.0	361.8	405.4
(X$_{CP}$)$_{TF}$	mm	280.0	311.3	373.3	415.3

Table 4.   Tail Fin Center of Pressure

c.   Tail Fin Normal Force Coefficient

The tail Fin Normal Force Coefficient, $(C_{N\alpha})_{TF}$, has the same quantitative definition as $(C_{N\alpha})_N$, where it is a derivative due to angle of attack. For linear wing theory, Dr. Fleeman specifies the following relationship for calculating this coefficient: $(C_{N\alpha})_{TF} = 4/\sqrt{M^2 - 1} = 4/\beta$ per radian [28].   Using the highest possible Mach number as a constant, M=3.2, I calculated a value of 1.33 per radian, which I use in all future stability calculations. As I stated earlier, when we use the highest Mach number then we are making a conservative estimate because a wing's aerodynamic efficiency degrades for increasing dynamic flow velocities.

D.   PITCH STABILITY

In the pitch stability analysis of the design projectile, I must sum two moments that act in the vertical plane and that rotate about the center of gravity. Using Figure 21, one can reference both moments from the center of gravity, which I have intersected with the pitch axis of rotation.
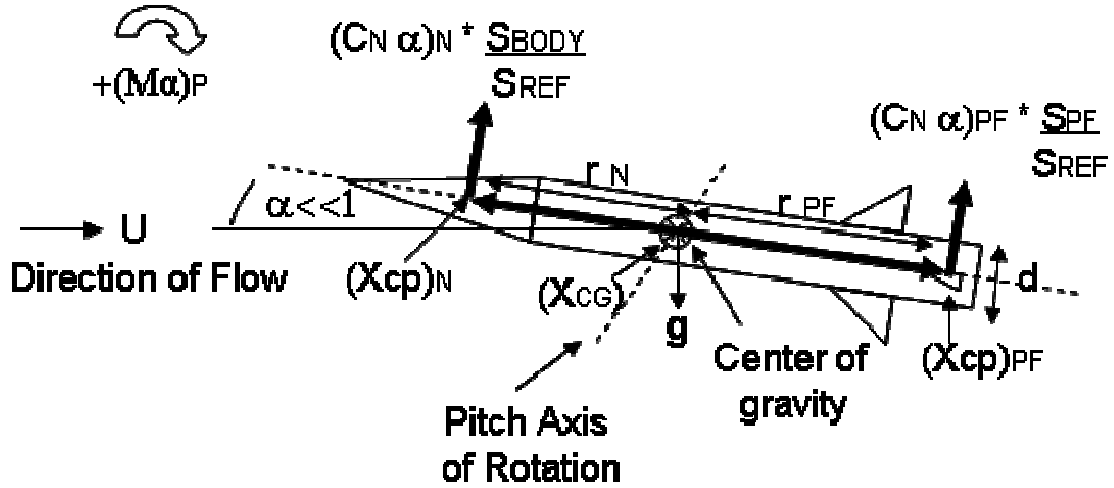
Figure 21.   Pitch Stability Concept Sketch

The   nose-body   moment   is   formed   by   the   effective   normal   force, $(C_{N\alpha})_N (S_{BODY}/S_{REF})$,   and   the   corresponding   effective   moment   arm, r_N/d $= [X_{CG} - (X_{CP})_N]/d$ [28]. As one can understand from the sign convention in Figure 21, the nose-body moment acts in the positive direction, $+(M_\alpha)_P$. I can further simplify the effective nose-body normal force by evaluating the ratio between the surface areas, S_{BODY}/S_{REF}. The body surface area is equal to the reference surface area. Therefore, the ratio is equal to one, and I can use $(C_{N\alpha})_N$ to represent the effective normal force.   The pitch-fin moment is formed by the effective normal force, $(C_{N\alpha})_{PF}(S_{PF}/S_{REF})$, and the corresponding moment arm, $r_{PF}/d = [X_{CG} - (X_{CP})_{PF}]/d$ [28].   This moment acts in the negative direction to oppose the nose-body moment. I can apply the negative sign convention to the pitch-fin moment based upon its direction of rotation, or I can let the relationship between the center of gravity and center of pressure produce the negative sign analytically. One must note that I have referenced the center of gravity, X_{CG}, and the center of pressure, $(X_{CP})_{PF}$, from the tip of the nose where $X=0$.   Therefore, the relationship of the center of gravity minus the center of pressure will yield a negative sign.   One can further examine the summation relationship with the following equation, and the input parameters with calculated moments are quantitatively given in Figure 22 and Table 5.

$$\sum (M_\alpha)_P = (C_{N\alpha})_N \left(\frac{r_N}{d} \right) + (C_{N\alpha})_{PF} \frac{S_{PF}}{S_{REF}} \left(\frac{r_{PF}}{d} \right)$$
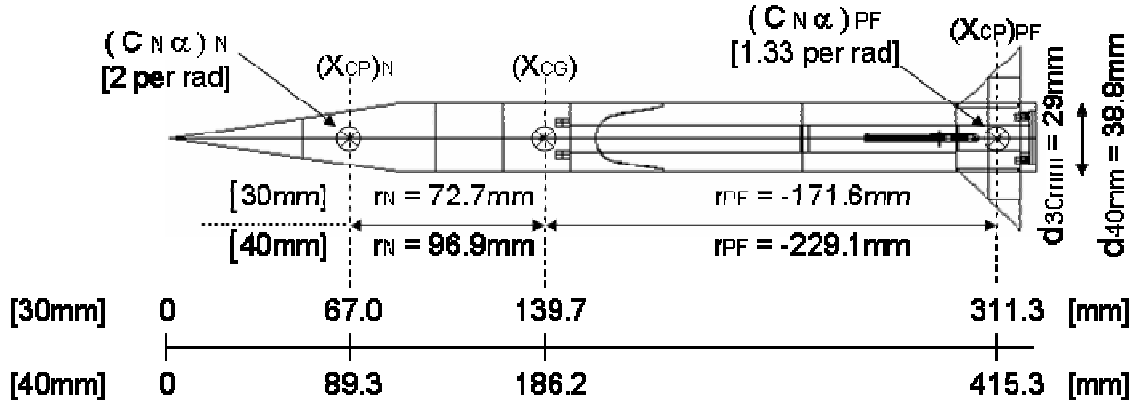
Figure 22.   Pitch Stability Projectile Diagram

Variable	Units	Description	30mm Projectile	40mm Projectile
$(C_{N\alpha})_N$	1/rad	Nose-body Normal Force Coefficient Derivative with respect to α	2.0	2.0
$(C_{N\alpha})_{PF}$	1/rad	Pitch-Fin Normal Force Coefficient Derivative with respect to α (M=3.2)	1.33	1.33
$(C_{N\alpha})_{PF}$	1/rad	Pitch-Fin Normal Force Coefficient Derivative with respect to α (M=2.4)	1.82	1.82
S_{PF}	mm^2	Pitch-Fin Planform Surface Area	481.6	861.0
S_{REF}	mm^2	Cross-sectional Surface Reference Area	665.5	1183
r_N	mm	Nose-body Effective Moment Arm	72.7	96.9
r_{PF}	mm	Pitch-Fin Effective Moment Arm	-171.6	-229.1
d	mm	Body Effective Diameter	29	38.8
$\sum (M_\alpha)_P$	1/rad	Sum of Pitching Moments due to Angle of Attack, α, at Mach 3.2	- 0.68	- 0.72
$\sum (M_\alpha)_P$	1/rad	Sum of Pitching Moments due to Angle of Attack, α, at Mach 2.4	-2.78	-2.83

Table 5.   Pitching Moment Input and Results

The concept sketch in Figure 21 shows an exaggerated schematic of a stable projectile. The amount of rotation that a projectile undergoes in the vertical plane or about the pitch axis must be extremely small in order for it to maintain its intended trajectory. As the projectile travels against the direction of flow, the nose-body pitching

46

moment creates a torque about the center of gravity that is opposed by the pitch-fin moment. If the nose-body moment is greater than the pitch-fin moment, then the sum of the moments will be a positive value. In this situation, without active control, the angle of attack, α, continually increases and causes the projectile to spin off trajectory. If the sum of the two moments is zero then the projectile will have neutral static stability. Although neutral static stability is sufficient for the conceptual design of a rocket-powered missile with maneuverable wings and fins, it is inadequate for an unguided projectile. The pitch-fin moment must be larger than the nose-body moment in order for the projectile to reduce its angle of attack and turn back into the direction of flow. If the pitch-fin moment is just slightly larger, the projectile will exhibit oscillatory motion about the direction of flow. This type of motion will not allow a projectile to maintain its intended trajectory, and precision will be poor.

Aerodynamic experts rate a projectiles ability to maintain static stability by calculating its static margin (SM). The general definition of the pitch static margin, SM_P, is the difference between the pitch aerodynamic center, $(X_{AC})_P$, and the center of gravity, X_{CG}, divided by the projectile's reference chord length, $\bar{c}$, which is given by $SM_P = \left[(X_{AC})_P - X_{CG} \right] / \bar{c}$ [30]. Just as the center of gravity represents the point at which the gravitational force acts on an object, the pitch aerodynamic-center, $(X_{AC})_P$, represents the point at which the combined normal lift-force acts on an aircraft or projectile in the vertical plane. In order for a projectile to have static stability and a positive static margin, the aerodynamic center must be behind the center of gravity when one references these points with respect to the nose. For that case, the aerodynamic center will have a larger magnitude than the center of gravity. Before I can calculate the static margin, I must first calculate the aerodynamic center.

I can calculate the pitch aerodynamic-center by refining the equation for the sum of the moments. By replacing the individual effective moment arms with the combined total moment arm, $\left[X_{CG} - (X_{AC})_P \right] / d$, I can represent the sum of the moments with the aerodynamic center. When I include the aerodynamic center in the equation for the sum of the moments, I can solve for it explicitly. The pertinent equations are the following:

$$\sum (M_\alpha)_P = \left[(C_{N\alpha})_N + (C_{N\alpha})_{PF} \frac{S_{PF}}{S_{REF}} \right] \frac{\left[X_{CG} - (X_{AC})_P \right]}{d}$$

$$(X_{AC})_P = X_{CG} - \frac{d \sum (M_\alpha)_P}{\left[(C_{N\alpha})_N + (C_{N\alpha})_{PF} (S_{PF}/S_{REF}) \right]}.$$

Given the final form of the equation for the pitch aerodynamic-center and the relationship for the static margin, I can conclude the analysis of pitch stability. The results of the static margin calculations will define each projectile's pitch stability. For both projectiles, the static margin is approximately 2 percent, which is lower than the acceptable static margin of 10 percent for ballistic projectiles [31]. One must also understand that the static margins I calculated for the design projectiles are for the highest Mach number. This result provides two pieces of additional information. First, I cannot set the launch velocity any higher than 1100m/s. A higher launch velocity will decrease the effectiveness of the tail fins and result in a lower static margin. At a speed of approximately 1200m/s, both projectiles have a total pitching moment of roughly zero. The pitch stability analysis has set an implicit constraint in the design for the maximum launch velocity. Second, the static margin will improve throughout the projectile's flight as drag naturally slows it to lower velocities. For instance, the 30mm projectile's static margin will improve to 7.5 % when it is traveling at its impact velocity of 828 m/s. The input variables and the results of the aerodynamic center and static margin calculations are summarized in Table 6.

Variable	Units	Description	30mm Projectile	40mm Projectile
X_{CG}	mm	Center of Gravity	139.7	186.2
$(X_{AC})_P$	mm	Aerodynamic Center, M=3.2	146.4	195.6
$(X_{AC})_P$	mm	Aerodynamic Center, M=2.4	164.0	219.2
$\bar{c}$	mm	Reference Chord	325	433
SM_Y	%	Static Margin at Mach 3.2	2.1	2.2
SM_Y	%	Static Margin at Mach 2.4	7.5	7.6

Table 6.   Pitch Static Margin Results

E.   YAW STABILITY

As one can observe from Figure 23, the concept sketch for yaw stability is almost an exact representation of the pitch stability sketch from the previous section. In this new orientation, I must analyze two moments in the horizontal plane or about the yaw axis of rotation.   With the assumption that one can understand the previous discussion on pitch stability, I will reference that section for the yaw stability analysis.
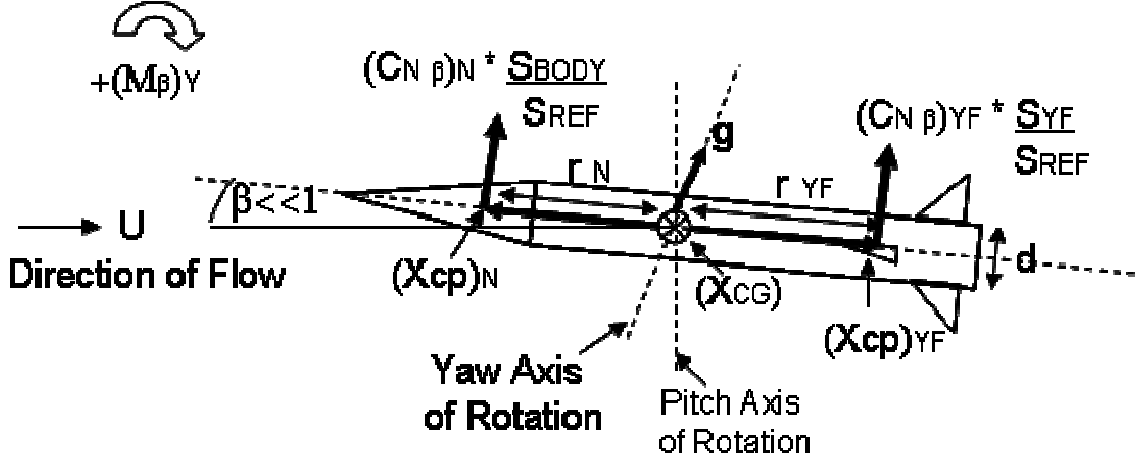
Figure 23.   Yaw Stability Concept Sketch

The effective nose-body normal force coefficient, $(C_{N\beta})_N \left(S_{BODY}/S_{REF} \right)$, and the corresponding effective moment arm, $r_N/d = [X_{CG} - (X_{CP})_N]/d$, are the same magnitude and dimensions as one finds in the pitch analysis [28]. Whether the projectile deviates from the direction of flow in the vertical or horizontal plane, it will experience the same nose-body normal force with respect to angle of attack.   From the concept sketch in Figure 23, one can see that the nose-body moment is positive, according to the clockwise sign convention, $+\left(M_\beta \right)_Y$.   The moment that opposes the nose-body, in the counterclockwise direction, comes from the effective yaw-fin normal force coefficient, $(C_{N\beta})_{YF} \left(S_{YF}/S_{REF} \right)$, and its corresponding moment arm, $r_{YF}/d = [X_{CG} - (X_{CP})_{YF}]/d$ [28]. The summation of the two moments and the development of critical-parameters follow the same method that I covered in the pitch stability section.   The yaw moment summation relationship is given by following equation:

$$\sum \left(M_{\beta} \right)_Y = (C_{N\beta})_N \left(\frac{r_N}{d} \right) + (C_{N\beta})_{YF} \frac{S_{YF}}{S_{REF}} \left(\frac{r_{YF}}{d} \right).$$

The input parameters and resulting moment calculations are given by Figure 24 and Table 7.
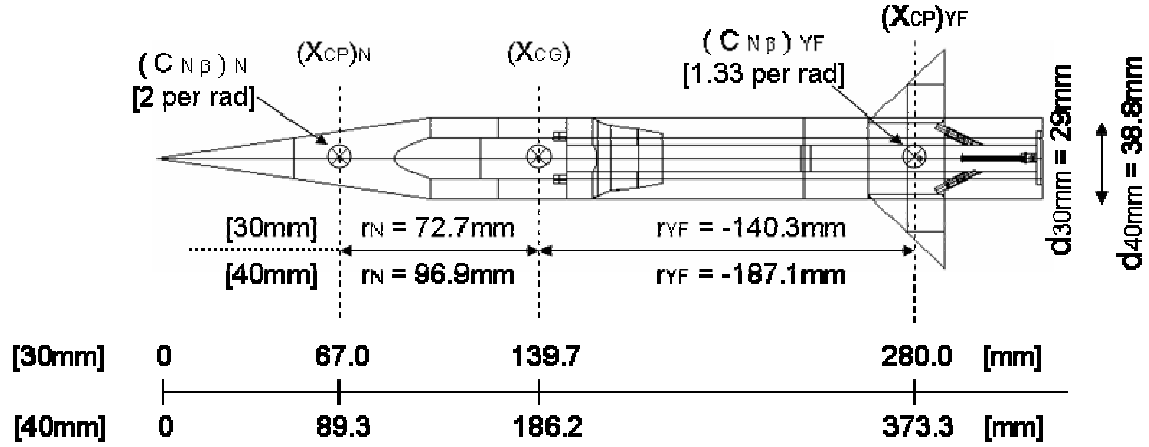
Figure 24.   Yaw Stability Projectile Diagram

Variable	Units	Description	30mm Projectile	40mm Projectile
$(C_{N\beta})_N$	1/rad	Nose-body Normal Force Coefficient Derivative with respect to β	2.0	2.0
$(C_{N\beta})_{YF}$	1/rad	Pitch-Fin Normal Force Coefficient Derivative with respect to β (*M*=3.2)	1.33	1.33
$(C_{N\beta})_{YF}$	1/rad	Pitch-Fin Normal Force Coefficient Derivative with respect to β (*M*=2.4)	1.82	1.82
S_{YF}	mm^2	Pitch-Fin Planform Surface Area	673.2	1200
S_{REF}	mm^2	Cross-sectional Surface Reference Area	665.5	1183
r_N	mm	Nose-body Effective Moment Arm	72.7	96.9
r_{YF}	mm	Pitch-Fin Effective Moment Arm	-140.3	-187.1
d	mm	Body Effective Diameter	29	38.8
$\sum (M_{\beta})_Y$	1/rad	Sum of Pitching Moments due to Angle of Attack, β, at Mach 3.2	- 1.50	- 1.51
$\sum (M_{\beta})_Y$	1/rad	Sum of Pitching Moments due to Angle of Attack, β, at Mach 2.4	- 3.89	- 3.90

Table 7.   Yaw Moment Inputs and Results

During the pitch stability analysis, I developed and defined the relationship needed to calculate the pitch static-margin. I use the same relationship for evaluating the

yaw static margin, which is given by the following equation: $SM_Y = \left[(X_{AC})_Y - X_{CG}\right]/\bar{c}$;

where SM_Y is the yaw static margin, $(X_{AC})_Y$ is the yaw aerodynamic center, X_{CG} is the projectile's center of gravity, and $\bar{c}$ is the projectile's reference chord length. Accordingly, I need to calculate the yaw aerodynamic-center. Although an axial-symmetric missile or projectile will have the same aerodynamic center in different evaluation planes, this is not true for projectiles that have irregular geometries or non-symmetric planforms. The design projectile is not axial-symmetric and does not have symmetric planforms. In the horizontal evaluation plane, the total yaw moment is larger in magnitude than the total pitch moment in the vertical plane. The design projectile has a yaw static margin of 4 % at Mach 3.2. At Mach 2.4, the static margin increases to 9 %. As I stated in the pitch stability analysis, aerodynamic experts consider static margins above 10 percent as acceptable [31]. The relationship I used to calculate the yaw aerodynamic center is given by the following equation. The input parameters and resulting calculations for the yaw static margin are given in Table 8.

$$(X_{AC})_Y = X_{CG} - \frac{d\sum(M_\beta)_Y}{\left[(C_{N\beta})_N + (C_{N\beta})_{YF}\left(S_{YF}/S_{REF}\right)\right]}$$

Variable	Units	Description	30 mm Projectile	40 mm Projectile
X_{CG}	mm	Center of Gravity	139.7	186.2
$(X_{AC})_Y$	mm	Aerodynamic Center, M=3.2	152.7	203.7
$(X_{AC})_Y$	mm	Aerodynamic Center, M=2.4	169.1	225.5
$\bar{c}$	mm	Reference Chord	325	433
SM_Y	%	Static Margin at Mach 3.2	4.0 %	4.0 %
SM_Y	%	Static Margin at Mach 2.4	9.0 %	9.1 %

Table 8.   Yaw Static Margin Results

F.   AERODYNAMIC DRAG

The evaluation of the effects of drag on a projectile is necessary to determine realistic target impact velocities from an initial launch velocity. I used drag analysis techniques from Dr. Fleeman's Tactical Missile Design to develop an equation for the

coefficient of drag with respect to velocity at a zero angle of attack [28]. Using this relationship, I then conducted a curve fitting analysis to represent the coefficient of drag as a simple function of a constant divided by the velocity. Finally, I used fundamental physics relationships to create an equation of each projectile's velocity with respect to flight distance. These equations are my desired outcome for the aerodynamic drag analysis. They link the ballistics effects to the electromagnetic launch by producing an estimated impact velocity for targets at specific distances, given a fixed launch velocity.

The zero angle-of-attack drag force, D_0, on a slender body projectile is the product of the coefficient of drag, C_{D_0}, the dynamic pressure, q_∞, and the cross-sectional surface reference area, S_{REF}. The expression for the drag force is given by $D_0 = C_{D_0} q_\infty S_{REF}$ [28]. For the design projectiles, the total coefficient of drag is the summation of contributions from the nose-body, $(C_{D_0})_{BODY}$, the yaw-fin planform, $(C_{D_0})_{YF}$, and the pitch-fin planform, $(C_{D_0})_{PF}$. The total coefficient of drag relationship is given by $C_{D_0} = (C_{D_0})_{BODY} + (C_{D_0})_{YF} + (C_{D_0})_{PF}$ [28]. I develop each of these contributing coefficients in following paragraphs. The dynamic pressure takes the same form that one can find in the Bernoulli Equation, where is it the product of one half the density of the fluid, $\rho/2$, and the square of the dynamic flow velocity, U_∞^2. The specific expression is given by $q_\infty = (\rho/2) U_\infty^2$ [32]. For all analytical calculations, I use the density of air at sea level or $\rho = 1.20 \ kg/m^3$. This assumption is reasonable because the intended trajectories of the design projectiles are for line-of-sight engagements at sea level. The dynamic flow velocity, U_∞, is the relative velocity of the projectile, u, along the flight path. For example, the dynamic flow velocity is the muzzle velocity at launch, and it decreases during flight because of drag. From the discussion above, one can start to see that zero angle of attack drag force is proportional to the square of the projectile's velocity, $D_0 \propto u^2$. By the end of the drag analysis, I will show an approximation expression of the drag force, where it is proportional to the projectile's velocity, $D_0 \propto u$.

The body drag coefficient, $(C_{D_0})_{BODY}$, is the sum of three components that involve the primary Mach cone, $(C_{D_0})_{BODY,WAVE}$, the pressure drag from the base, $(C_{D_0})_{BASE,COAST}$, and the natural drag from skin friction, $(C_{D_0})_{BODY,FRICTION}$. The form of the expression for the body drag coefficient is given by $(C_{D_0})_{BODY} = (C_{D_0})_{BODY,WAVE} + (C_{D_0})_{BASE,COAST} + (C_{D_0})_{BODY,FRICTION}$ [28]. The first coefficient, $(C_{D_0})_{BODY,WAVE}$, represents the drag loss from the projectile's nose cone as it separates the dynamic flow around the rest of the body. For supersonic velocities or Mach numbers greater than one, a primary Mach cone forms and represents the flow discontinuity between the exterior dynamic flow and the interior flow around the projectile's body. We can represent this coefficient for supersonic Mach numbers with the following relationship involving the nose fineness, L_N / d, and the Mach number, M: $(C_{D_0})_{BODY,WAVE} = 3.6 / \left[(L_N / d)(M-1) + 3 \right]$ [28]. The second coefficient, $(C_{D_0})_{BASE,COAST}$, represents the drag loss from base pressure for an unpowered projectile. The parallel body flow at the end of the projectile does not immediately close behind the flat base; rather, a low-pressure area forms causing rearward suction, which contributes to drag. The relationship for this coefficient at supersonic velocities is simply 0.25 divided by the Mach number, $(C_{D_0})_{BASE,COAST} = 0.25 / M$ [28]. The last coefficient, $(C_{D_0})_{BODY,FRICTION}$, characterizes the skin friction that we are most accustomed to thinking about when analyzing drag. Dr. Fleeman represents this coefficient with the following relationship: $(C_{D_0})_{BODY,FRICTION} = 0.053(L / d)[M / (q_\infty L)]^{0.2}$; where L is the total length of the projectile [28]. A problem will occur if someone tries to calculate values using *mks* units because Dr. Fleeman explicitly uses British units in his calculations. One needs to multiply this function by a factor of 1.7 in order to correctly calculate values in *mks* units [33]. The correct form of the function that I use in this analysis is the following: $(C_{D_0})_{BODY,FRICTION} = 0.09(L / d)[M / (q_\infty L)]^{0.2}$. The description of this last coefficient concludes the development of the body-drag coefficient.

The drag analysis for the yaw-fin planform and the pitch-fin planform is the same. I will use the description for a tail fin to develop this analysis. One can equally apply this

analysis to the yaw-fin and pitch-fin without changing any forms of the relationships. The coefficient of drag for a tail fin is the sum of contributions from wave drag, $(C_{D_0})_{TAIL,WAVE}$, and skin friction, $(C_{D_0})_{TAIL,FRICTION}$. The complete form of the relationship is given by $(C_{D_0})_{TAIL} = (C_{D_0})_{TAIL,WAVE} + (C_{D_0})_{TAIL,FRICTION}$ [28]. The first coefficient, $(C_{D_0})_{TAIL,WAVE}$, represent the supersonic drag loss from the tail fin's creation of a subordinate shock wave inside the primary Mach cone. Dr. Fleeman states that this coefficient is based upon modified Newtonian theory in which it incorporates the calculation of the pressure across the fin's normal shock as a function of Mach number [28]. The analytical relationship for this coefficient has a complicated form. One can find this relationship and physical parameter definitions in Figure 25. The last coefficient, $(C_{D_0})_{TAIL,FRICTION}$, represents the skin friction. It takes a similar form to what I introduced for the body friction coefficient, mentioned previously. Just as with the body friction coefficient, it is necessary to multiply by a factor of 1.7 in order to adjust calculations for *mks* units [33]. The relationship describing the tail friction coefficient is also shown in Figure 25.
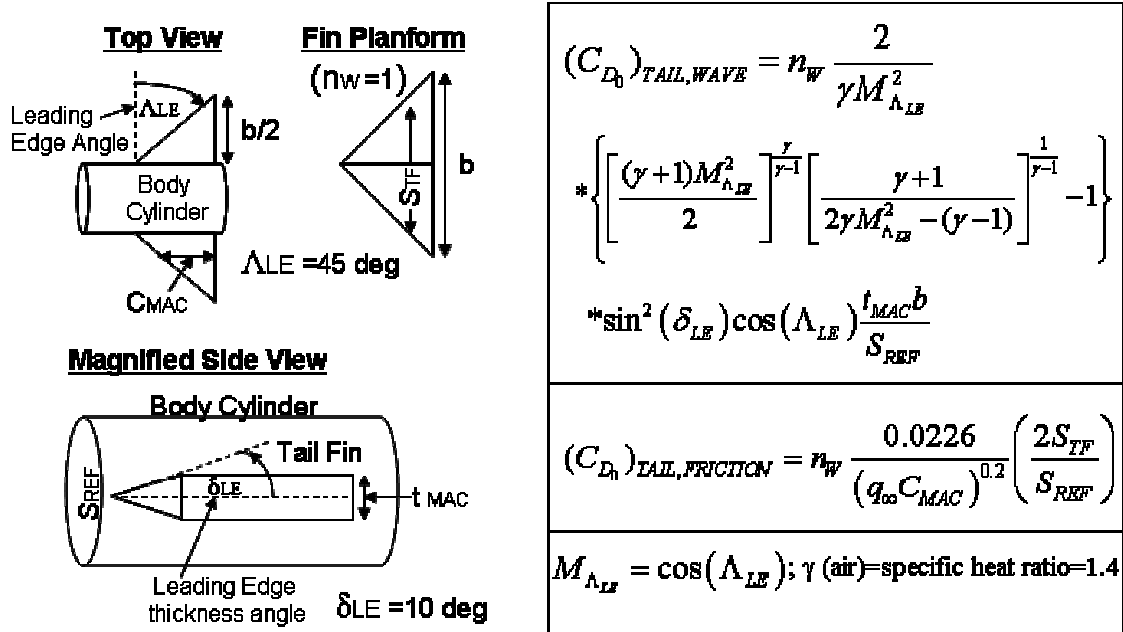
Figure 25.   Tail Fin Drag Coefficients

The only input parameters, which I have not discussed thus far, are two tail-fin angles, the number of wings, and the specific heat ratio specified in Figure 25. The leading edge angle, Λ_{LE}, describes the amount of sweep for a planform. The angle is referenced from the body cylinder's surface normal vector at the planform's leading edge. All fins in this design are swept at approximately 45 degrees. The leading edge thickness angle, δ_{LE}, corrects the coefficient of drag functions for the sharpness of the fins. I have not specified this value anywhere else in the design because of the complications with drawing that type of geometry. I have assumed a leading edge thickness angle of 10 degrees for all fins. The number of wings, n_W, corrects the coefficient of drag functions for the number of planforms. In the case of the yaw-fins and pitch-fins there is only one planform for each set of fins. I have further specified the number of wings in Figure 25. The specific heat ratio, γ, is the quotient of the specific heat capacity for air at constant pressure, c_P verses constant volume, c_V, and is given by $\gamma = c_P/c_V$. For the sea-level flow regime, this value is $\gamma = 1.4$.

Using a Maple computer worksheet, I was able to develop an equation for the coefficient of drag as a function of the projectile's velocity, $C_{D_0}(u) = (C_{D_0})_{BODY}$ $+ (C_{D_0})_{YF} + (C_{D_0})_{PF}$ [34]. I created a continuous plot of this function for velocities between 343 m/s and 1100 m/s. Finally, I developed a best fit function in the form of a constant divided by velocity. Both projectiles had the same plot for their respective coefficient of drag functions. This is a reasonable expectation since both projectiles are equally scaled. One can find the Maple computer code for both projectiles in the Appendix (See Appendix E). The effectiveness of the curve fits for both projectiles are shown in Figure 26.
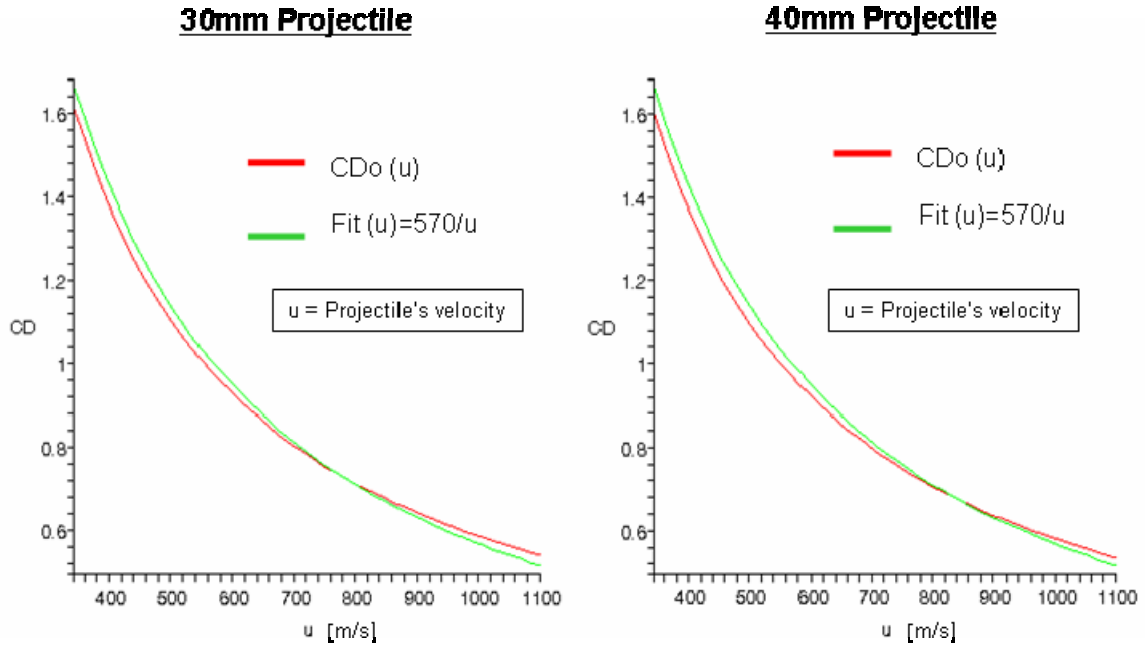
Figure 26. Curve Fit of the Coefficient of Drag for Both Design Projectiles

From the results of the curve fit, I developed an equation for each projectile's velocity as a function of flight distance. Using basic Newtonian physics, one can say that the sum of the forces in the x-direction, the direction of flight, is equal to the negative drag force, $\sum F_x = M\left(du_x/dt\right) = -D_0 = -C_{D_0}q_\infty S_{REF} = -\left(\rho/2\right)u_x^2 C_{D_0}S_{REF}$. The result of the curve fit gives us a coefficient of drag that is approximately equal to: $C_{D_0} = 570/u_x$. If I substitute this relationship into the force equation then I am left with the following differential equation: $\left(du_x/dt\right) = -\left(285\rho S_{REF}/M\right)u_x$. One can manipulate the left side of the equation by separating the differential into the following form: $\dfrac{du_x}{dt} =$

$\dfrac{du_x}{dx}\dfrac{dx}{dt}^{u_x} = u_x\dfrac{du_x}{dx}$. This last step should enable one to see that the velocity will cancel from both side of the differential equation. If I take the differential dx to the right side and integrate both sides of the equation over the limits of the flight path then I will have the final form of the equation for velocity as a function of distance. I already stated that this equation links ballistics to electromagnetic launch. The constrained launch velocity is 1100m/s, and from the ballistics analysis, I intend to impact targets at 2 km and 500 m

56

(See Chapter II). Given these input parameters and the velocity equation, I can solve explicitly for the impact velocity. One can examine the integration limits, the final form of the velocity equation, and a summary of results in the following equations and Table 9. In Table 9 I list two sets of impact velocities for each target. I previously calculated a coefficient of drag that had the form of $C_{D_0} = 525/u_x$. This value produced slightly higher impact velocities. For my ballistics analysis, I used these velocities as input parameters in my ballistic simulations. Considering the effectiveness of the Infantry Railgun Projectile against both targets, I consider the influence of this miscalculation to be negligible (See Chapter II).

$$\int_{1100m/s}^{u} du_x = -\frac{285\rho S_{REF}}{M}\int_{0}^{x} dx \rightarrow u(x) = 1100 m/s - \frac{285\rho S_{REF}}{M} x \quad [mks]$$

Variable	Units	Description	30mm Projectile	40mm Projectile
ρ	kg/m^3	Density of air	1.20	1.20
S_{REF}	m^2	Surface Reference Area	6.65×10^{-4}	1.18×10^{-3}
M	kg	Total Mass of Projectile	1.50	3.55
u(2 km)	m/s	RHA at 2000 m	828	890
u(2 km)	m/s	RHA at 2000 m (Corrected)	797	872
u(500 m)	m/s	DLRC at 500 m	1032	1048
u(500 m)	m/s	DLRC at 500 m (Corrected)	1024	1043

Table 9.   Estimated Impact Velocities from Drag Analysis

G.   AERODYNAMIC CONCLUSIONS

The concept-level analysis that I conducted for the design projectiles in the area of aerodynamic stability and drag satisfactorily achieved the overall design constraints (See Appendix A3). Using Dr. Fleeman's analytical methods, I successfully proved neutral stability for both projectiles with static margins of at least 2 percent. Although the static margin results are not within an acceptable range for ballistic projectiles, I am confident that certain design modification will yield acceptable results. For instance, one could replace both the pitch and yaw stability fins with a cruciform lattice-fin design. This type of planform is appropriate for both the design constraint of being folded inside the railgun and the high supersonic Mach numbers that one can find in my design.   I

successfully achieved the second objective that I set out to complete. My secondary objective was to create an equation of velocity with respect to flight distance; my curve-fitting method results in reasonable impact velocities. In conclusion, the aerodynamic analysis of both design projectiles shows favorable characteristics for future research.

IV.   ELECTROMAGNETIC LAUNCH (EML)

A.   EML OVERVIEW

The results of the combined ballistic and aerodynamic analysis require a muzzle velocity of 1100 m/s in order to defeat the RHA target proposed in this thesis.   I considered the required muzzle velocity for the development of both the 30mm and 40mm railguns. From the design constraints in Appendix A, the lengths of both railgun barrels must be set at 3 meters. Barrel lengths shorter than 3 meters will require higher effective currents to attain the necessary launch velocity; higher current are undesirable. The rail separations in both railgun barrels are fixed based upon the thicknesses of their respective design projectiles. Given these specifications, there are a range of possible solutions for the heights and widths of the conducting rails.   One can reference the dimensions of height, *h*, and width, *w*, in Figure 27. Matched with appropriate effective currents, each solution to the rail geometry can produce an 1100 m/s muzzle velocity.
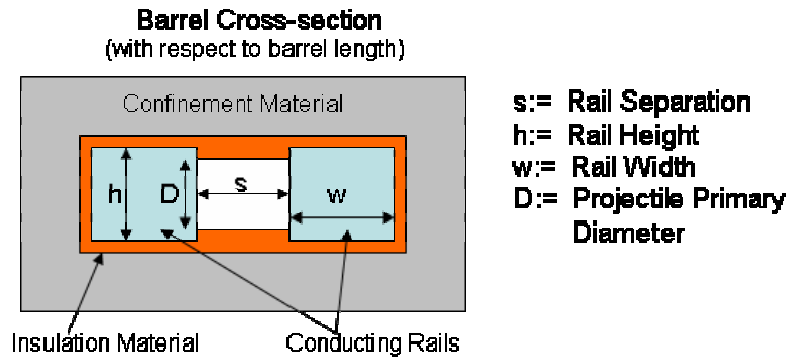
Figure 27.   Dimensions for Conducting Rails

The design constraint of maximum temperature rise in the rails dominated this analysis and limited the number of solutions (See Appendix A9). The cross-sectional area of the conducting rails was the dominant factor in meeting the temperature requirement. Considering realistic guiding surfaces based upon each design projectile's primary diameter, I selected the smallest possible values of *h* for both the 30mm and 40mm rails. I then found the most favorable designs for both railguns by specifying *w*. Using fixed values for the rail geometry, I obtained appropriate effective currents in each railgun. These values were less than the design constraint of 2 MA (See Appendix A7).

Next, I made rough estimates on possible melting conditions for both projectiles. I used multiple finite element computer models to improve my rough estimates. The results of my analyses show that both design projectiles paired with their respective optimized railgun barrels will theoretically allow for a launch velocity of 1100 m/s without melting.

B. THEORETICAL CONSIDERATIONS

In ideal electromagnetic launch conditions, given by constant current and solid electrical contact, one can make reasonable estimates of the electromagnetic force induced by rectangular conducting rails. Over the past half-century, railgun researchers have developed theoretical relationships that allowed them to make reasonable estimates for the inductance gradient and the electromagnetic force [7]. These researchers have also developed thermodynamic relationships to estimate the electrical heating for all major components of a railgun [7], [8]. In realistic experimental conditions, there are several explicit and implicit factors that can significantly change the result of a launch with respect to the theoretical estimates. These factors include the exact pulse shape of the current, the loss of solid electrical contact between the projectile and the conducting rails, and unusual armature configurations. In order to address these issues adequately, one would either have to perform physical experimentation or computer modeling that included a transient current analysis with sliding contact. Realistic experiments and computer models with sliding contact are outside of the scope of this thesis research, and I have left them to future work on this design. Throughout my analysis of electromagnetic launch, I only consider theoretical relationships that are applicable to ideal conditions.

The underlying theoretical principal that fully describes both the magnitude and direction of the electromagnetic force inside a railgun is the Lorentz force law. This fundamental physics principal allows one to calculate the magnetic force, $\vec{F}_{mag}$, on a projectile by integrating the cross product of the volume current density, $\vec{J}$, and the magnetic flux density, $\vec{B}$. It is represented in the following mathematical relationship: $\vec{F}_{mag} = \iiint_V (\vec{J} \times \vec{B}) d\tau$; where $d\tau$ is the volume integrand that depends on the coordinates system. To evaluate this integral over a simple projectile geometry, one would either

have to use a finite element code or assume that the current and magnetic flux density are both uniform and unidirectional. A fact of electromagnetic launch is that the current does not distribute itself uniformly as it passes through a projectile. Furthermore, the magnetic flux density through the projectile is not uniform. As the current approaches the conductive portion of the projectile, it bends along paths of lower electrical potential and resistance. Circular "Eddy Currents" form near the interface of the conducting rail and the first cross contact surface on the projectile [7]. Overall, the evaluation of the electromagnetic force on a projectile from the Lorentz force relationship is complicated. Railgun researchers have developed a single formula that is equivalent to the Lorentz force law, commonly known as the railgun force law [7].

$$F = L'I^2/2$$

I is the effective current through the projectile. The inductance gradient, L', has units of Henry per meter, or inductance per unit length. The value of the inductance gradient depends upon the geometry of the conducting rails, to include their separation distance. The Kerrisk method is a valid semi-empirical model for calculating L' in square or rectangular conducting rails [7], [35]. One can find the complete expression for the Kerrisk method in Figure 48 of Appendix C.

Considering a constant or effective current, I, railgun researchers have used the railgun force law to develop a relationship for the conducting rail length, x_L, in terms of an intended muzzle velocity, v_L. The first step in obtaining this relationship is to express the force law in a form that describes the railgun projectile's acceleration, a_p. Since the mass of the projectile, M_p, times its acceleration is equal to the railgun's force, F, then $a_p = dv_p/dt = L'I^2/(2M_P)$; where v_p is the instantaneous velocity. If I is constant then the muzzle velocity, v_L, is given by

$$v_L = \int_0^{v_L} dv_p = \frac{L'I}{2M_P} \int I dt = \frac{L'IQ}{2M_P} .$$

Since $I = dQ/dt$, then the charge that has passed through the projectile is $Q = \int I dt = 2v_L M_P/(L'I)$. Solving for the projectile's final position, x_L, along the conducting rails at the muzzle velocity, v_L, one finds

$$x_L = \int_0^{x_L} dx = \frac{L'}{2M_P}\int QI dt = \frac{L'}{2M_P}\int Q dQ = \frac{L'Q^2}{4M_P}.$$

If one substitutes the expression for charge in terms of muzzle velocity, $Q = 2v_L M_P/(L'I)$, into the solution above, then the following final form for the rail length is given by

$$x_L = \frac{M_P}{L'}\left(\frac{v_L}{I}\right)^2.$$

This result contains parameters that can be used to solve for a required rail length.

One can derive three subsequent relationships from the expression for required rail length, $x_L = \frac{M_P}{L'}\left(\frac{v_L}{I}\right)^2$. If the rail length is a fixed parameter, then a simple manipulation of the relationship above will produce an expression for the final muzzle velocity,

$$v_L = I\sqrt{L'x_L/M_P}.$$

One can also rearrange these variables to produce an expression for the required effective current,

$$I = v_L\sqrt{M_P/(x_L L')}.$$

Using the identity for current, $I = dQ/dt$, one can solve for the final launch time, t_L.

$$t_L = \int_0^{t_L} dt = \frac{1}{I}\int dQ = \frac{Q}{I} = \frac{2x_L}{v_L}.$$

All of these expressions, to include the Kerrisk Method, allow one roughly to match conducting rail geometry, projectiles, power supplies, and barrel lengths.

The average temperature rise in the conducting rails after an electromagnetic launch is a practical consideration when considering the ability of a railgun to sustain multiple shots. Railgun researchers have developed a heat relationship that allows for estimates on the average temperature rise, ΔT, in the conducting rails. This relationship is shown in the following expression:

$$\Delta T = \left[\rho_e / \left(\rho_m C_p \right) \right] G / A^2 \ ;$$

where ρ_e is the electrical resistivity, ρ_m is the mass density, C_p is the heat capacity, $G = \int I^2 dt$ is the electrical action, and A is the cross-sectional area through which current flows [8]. The resistivity, density, and heat capacity depend upon the material properties of the conducting rails. The electrical action, G, is proportional to the electrical energy dissipated in a material in the form of heat, and has units of *Ampere²-seconds* or $\left[A^2 s \right]$.

From $a_p = \dfrac{dv_p}{dt} = \dfrac{L'I^2}{2M_P}$, it follows that

$$v_L = \int_0^{v_L} dv_p = \frac{L'}{2M_P} \int I^2 dt = \frac{L'}{2M_P} G,$$

or

$$G = \frac{2M_p v_L}{L'} \ .$$

This relationship for the electrical action, allows one to make reasonable estimates for the average temperature change in the conducting rails.

Another practical consideration involving electrical heating is the ability of a projectile to withstand a maximum effective current over a particular launch time. There are limits on how much current can pass through conductive materials before they melt. One must consider two important parameters when evaluating potential melting situations in railgun projectiles: the electrical action, $G = \int I^2 dt$, and the cross-sectional area, A, of the solid conductive portion of a projectile that interfaces with the conducting rails. Using these parameters, railgun researches have developed a quantifiable material characteristic called the specific action to melt (SAM) [7]. One can calculate the specific action, g, of a conductive material by using the following relationship: $g = G / A^2$ [7].

The SAM for aluminum, tungsten, and copper have respective values of 2.52×10^4, 2.43×10^4, and 8.05×10^4 in units of $\left[A^2 s / mm^4 \right]$ [7]. Recent research on the analysis of electrical heating in conductive armatures has shown that aluminum and copper can be used right up to their SAM without diminishing the performance of their conduction ability or structural integrity [7]. The three materials mentioned above and their respective SAMs are important in this analysis because my design involves copper conducting rails and aluminum-tungsten projectiles.

Each of the theoretical considerations mentioned above has specific relevance to the analysis that I conducted on the two design railguns. This analysis involves an ideal projectile launch with a constant effective current, *I*.

C.   BARREL OPTIMIZATION

The temperature rise in the copper rails of my initial 30mm and 40mm railgun designs resulted in values near the melting point for copper. These initial designs involved optimizing the inductance gradient and the effective current. Successive attempts with this method consistently resulted in temperature changes above the design constraint of the 20 °C (See Appendix A9). These results indicated that the electrical heating in the copper rails was the dominate factor in this analysis.

To eliminate any concerns about the temperature rise in the copper rails, I approached the design by setting the temperature change to 20 °C. The railgun relationship, $\Delta T = \left[\rho_e / \left(\rho_m C_p \right) \right] G / A^2$, was used to give the temperature rise. One can eliminate the electrical action, *G*, in this relationship by substituting its ideal form, $G = 2 M_p v_L / L'$, to obtain

$$\Delta T = \frac{\left[\rho_e / \left(\rho_m C_p \right) \right] 2 M_p v_L}{L' A^2} \,.$$

The ratio in the square brackets, consisting of the electrical resistivity, mass density and heat capacity, has a value of 0.005 $[K - mm^4 / A^2 s]$ for copper. This value remains approximately constant for copper below its melting point [8]. The mass of the

projectile, M_p, and the muzzle velocity, v_L, are constant in both railgun designs. Applying the Kerrisk method to solve for the inductance gradient, L', one will find that it is a function of the *s*, *h*, and *w* (See Figure 27 and Appendix C). The values of *s* are constant in 30mm and 40mm railguns because they depend upon the respective thickness of their design projectiles. The last term in the thermodynamic relationship is the cross-sectional area, $A = hw$.

During any optimization process, it is important to limit the number of variables. From the expression for ΔT and the dependence of L' on *h* and *w* in the Kerrisk method, I found that an increase in *h* past the minimum required contact surface for each projectile had a negative impact on the design solution. Thus *w* was selected to reduce ΔT. In order to eliminate the rail height as a variable, I considered a practical launch situation involving the generic railgun barrel in this thesis (See Figure 27). Rails in the generic railgun are separated by ceramic insulators that also serve as a guiding surface for the projectile during launch. I made an assumption that a ceramic insulator extension of 2.5 mm was sufficient to hold the conducting rails in position. This is a reasonable assumption, considering that the Lorentz force acts to push the conducting rails apart during a launch. I did not consider whether or not the 2.5mm ceramic insulator extension was sufficient to allow for tension on the rails before or after a launch. Given an overall extension of 5 mm, from above and below the rails, the minimum required *h* is the primary body diameter of the projectiles plus the extension. This results in $h = 35$ mm for the 30mm railgun and $h = 45$ mm for the 40mm railgun. With a fixed *h*, the optimization process was reduced to a single variable, *w*.

I found the appropriate values of *w* for each railgun by adjusting this parameter in the thermodynamic relationship until the temperature change for the copper rails was approximately 20 °C. The resulting *w* for the 30mm railgun was 40 mm, and for the 40mm railgun it was 50 mm. During the thermodynamic optimization, it was necessary to calculate L' as an intermediate step. Given the respective parameters in Figure 28, the Kerrisk method yields L' = 0.38 µH/m for the 30mm railgun and L' = 0.39 µH/m for the 40mm railgun. One can then calculate *I* and *G* from $I = v_L \sqrt{M_P/(x_L L')}$ and $G = 2M_p v_L/L'$. Having known values for L' and *I*, one can estimate the resulting

Lorentz force on the projectiles using the railgun force law, $F = L'I^2/2$. This concludes the optimization of the conducting rails. Figure 28 shows the configuration of both railgun barrels, and Table 10 summarizes the input values and the results of this analysis.
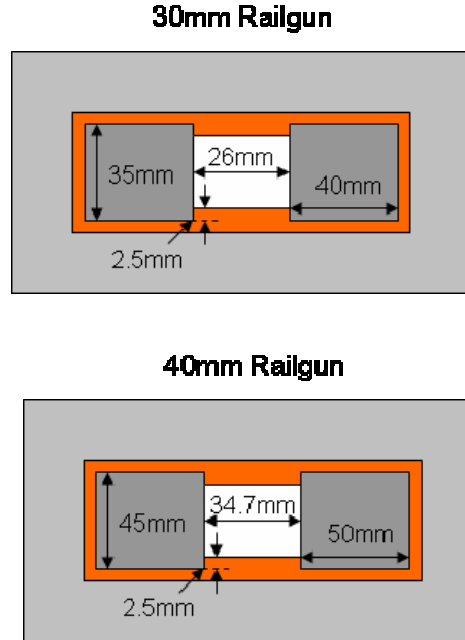
Figure 28.   Optimized Railgun Barrels

Variable	Units	Description	30mm Projectile	40mm Projectile
Mp	kg	Mass of Projectile	1.50	3.55
x_L	m	Length of Conducting Rails	3.0	3.0
v_L	m/s	Muzzle Velocity	1100	1100
t_L	ms	Launch time	5.45	5.45
L'	μH/m	Inductance Gradient	0.380	0.389
ΔT	°C	Temperature Change in Rails	21.8	19.5
I	MA	Effective Current	1.28	1.92
G	A^2s	Electrical Action	8.68×10^9	2.10×10^{10}
F	kN	Force on Projectile	311	719

Table 10.   Inputs and Results for Railgun Optimization

D.   PROJECTILE HEATING

With the temperature rise in the conducting rails constrained to a nominal level, I focused my analysis on the susceptibility of melting in the design projectiles. To estimate the effects of electrical heating, I compared my estimates for the specific action,

$g = G / A^2$, of each material to its SAM. The railgun barrel optimization produced values for G, which are listed in Table 10. The cross-sectional areas, A, are difficult to define for these projectiles because of their complicated volumetric structures, as indicated in Figure 29. In order to apply the specific action relationship to this design, I had to make conservative estimates on cross-sectional areas. Furthermore, I had to analyze the conductive properties of the tungsten (W) and aluminum (Al) materials in order to appropriately adjust the electrical action to realistic values. My rough estimates indicate that g exceeds SAM for the aluminum armatures in both design projectiles. If the electrical energy dissipated as heat in the armature is averaged over the whole volume of the aluminum then g exceeds SAM for the 30mm projectile but not for the 40mm projectile. The difference between these two techniques indicates a need for further refinement.

Figure 29.   Conductive Portions of the 30mm and 40mm Projectiles

A conservative estimate for the conductive cross-sectional area, A, in each design projectile consists of the W and Al rail interfaces that have solid continuous volumes between the conducting rails. These areas are shown in Figure 29 as $A1$ and $A2$, respectively. The vertical lengths of the two areas are equal. Therefore, one can use the
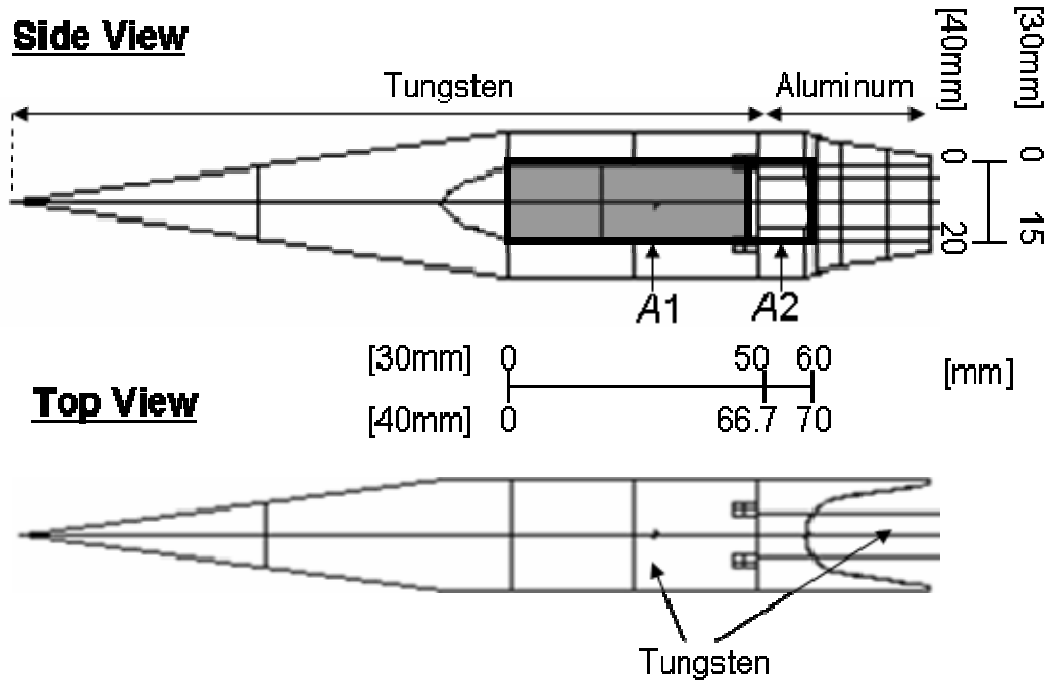
horizontal lengths to make a comparison. The length of the aluminum area is one-sixth or approximately 16 % of the total length along $A1$ and $A2$. If W and Al were to have similar conductive properties, then one might expect that approximately 16 % of the total current would flux through area $A2$, but in fact their resistivities differ.

A comparison of the conductive properties between W and Al is necessary to estimate the current distribution across areas $A1$ and $A2$. The electrical resistivity, ρ_e, of W is 5.7 µΩ-cm and for Al it is 2.82 µΩ-cm [8]. At approximately 25 °C, $\rho_e(Al) \leq 0.5\rho_e(W)$. Since the resistivity in a conductive material is a function of temperature, it is necessary to examine these values at the first melting point in the projectile. The melting point of Al is 660 °C and the melting point of W is 3410 °C [7]. At the melting point of Al, the resistivity of W increases to 22.0 µΩ-cm and for Al the resistivity increases to 11.2 µΩ-cm [8], [35]. Therefore, the Al is still 50 percent less resistive or two times more conductive than W.

Considering the area ratio and the difference in conductivity between areas $A1$ and $A2$, one can make an assumption about the distribution of current. Since Al is consistently two times more conductive than W up to its melting point, the distribution of current in $A2$ should be 32 % or 0.32 of the total current (i.e., $I_2/I = 0.32$). Therefore, the remaining 68 % of the total current flows through the W in area $A1$ (i.e., $I_1/I = 0.68$). The initial relationship that describes electrical action is the following: $G = \int I^2 dt$. In this design analysis, the effective current, I, is a constant; therefore, one can assume that $G \propto I^2$. This assumption allows for the development of effective electrical action values for areas $A1$ and $A2$. These values are based upon the total electrical action in each railgun design and the square of the current distributions through each area. Therefore, the effective action in area $A1$ is $G_1 = G(I_1/I)^2$. Similarly, the effective action in area $A2$ is $G_2 = G(I_2/I)^2$. Using effective values for the electrical action and the specific areas of $A1$ and $A2$, one can calculate the specific action for W and Al. A summary of the inputs and results for these calculations are shown in Table 11.

68

Variable	Units	Description	30mm Projectile	40mm Projectile
G	$A^2 s$	Calculated Electrical Action	8.68×10^9	2.10×10^{10}
$A1$	mm^2	Cross-sectional Area for W	750	1334
$A2$	mm^2	Cross-sectional Area for Al	150	266
$G1$	$A^2 s$	Effective Action for $A1$ (W)	4.01×10^9	9.71×10^9
$G2$	$A^2 s$	Effective Action for $A2$ (Al)	8.89×10^8	2.15×10^9
$g1$	$A^2 s/mm^4$	Specific Action for $A1$ (W)	15431	11800
$SAM(W)$	$A^2 s/mm^4$	Specific Action to Melt (W)	24270	
$g2$	$A^2 s/mm^4$	Specific Action for $A2$ (Al)	39511	29679
$SAM(Al)$	$A^2 s/mm^4$	Specific Action to Melt (Al)	25240	

Table 11.   Inputs and Results for Projectile Heating

The resulting specific actions for the *Al* armatures, in both design projectiles, are higher than SAM(*Al*). The *Al* armature in the 30mm projectile has a specific action that is 57 % higher than SAM(*Al*) , and for the 40mm projectile it is 18 % higher. This result indicates that both armatures will melt during launch.

The conservative estimates that I made for the aluminum's cross-sectional area, do not account for the entire volumes of the two armatures. Taking the area *A*2 for each armature and multiplying by their respective rail separations produces volumes of 3.9 cm^3 for the 30mm projectile and 9.2 cm^3 for the 40mm projectile. In comparison with their total volumes in Appendix B3, these values account for 40 % of the armatures.

Another approach to this analysis is to create effective areas for each material that are based upon their actual volumes. For the *Al* armature, this method involves taking each armature's total volume in Appendix B3 and dividing by their respective rail separation. This will an produce effective area of 381 mm^2 for the 30mm armature and 677 mm^2 for the 40mm armature. Using these values for cross-sectional areas in conjunction with their effective actions will produce specific actions of 27624 $A^2 s/mm^4$ and 21171 $A^2 s/mm^4$ for the respective 30mm and 40mm aluminum armatures. In this case, only the 30mm projectile shows indications of melting based upon a SAM(*Al*) of 25240 $A^2 s/mm^4$. I must assume that the experimental values for the armatures are somewhere between the original conservative estimates and this other approach.

One cannot theoretically determine the actual current distributions along the conductive portions of the design projectiles. The complex 3D geometries of the projectiles require finite element modeling in order to properly predict current distribution and electrical heating.

E. EML FINITE ELEMENT MODELING

I used Comsol Multiphysics, Version 3.2, to develop three finite element computer models for each design projectile [39]. The primary objective of this modeling was to simulate the current distribution and the time dependent electrical heating in the aluminum armatures. The projectiles are stationary in all models. A direct current (DC) model was used to establish the distribution of the volume current density. The solution to this model served as an input to a magnetostatics solver. I used the magnetostatics solutions to calculate the Lorentz force on the projectile. The output from the DC model was used again to obtain a final transient conductive heat transfer model and to estimate the incremental temperature change of each projectile during a 5 ms current flux. The results of the final heat analysis indicate that neither armature will melt under launch conditions.

Computations of the electromagnetic launch included a portion of the copper conducting rails and an approximate version of the projectile for each design. The appropriate material properties of each component were used throughout the simulation process. I made the conducting rails long enough to contain the projectile. I placed the rails such that the aluminum armature was significantly more than four calibers past the current source, so that the computed Lorentz force could be compared with $F = L'I^2/2$. Limitations with Comsol's finite element mesh required a slight modification to the back end of the armature. The U-shaped curvature was approximated by four surfaces. A modeling environment surrounded the partial railgun structure in order to allow for magnetic flux density calculations. The geometric setup of each model is shown in Figure 30.

70
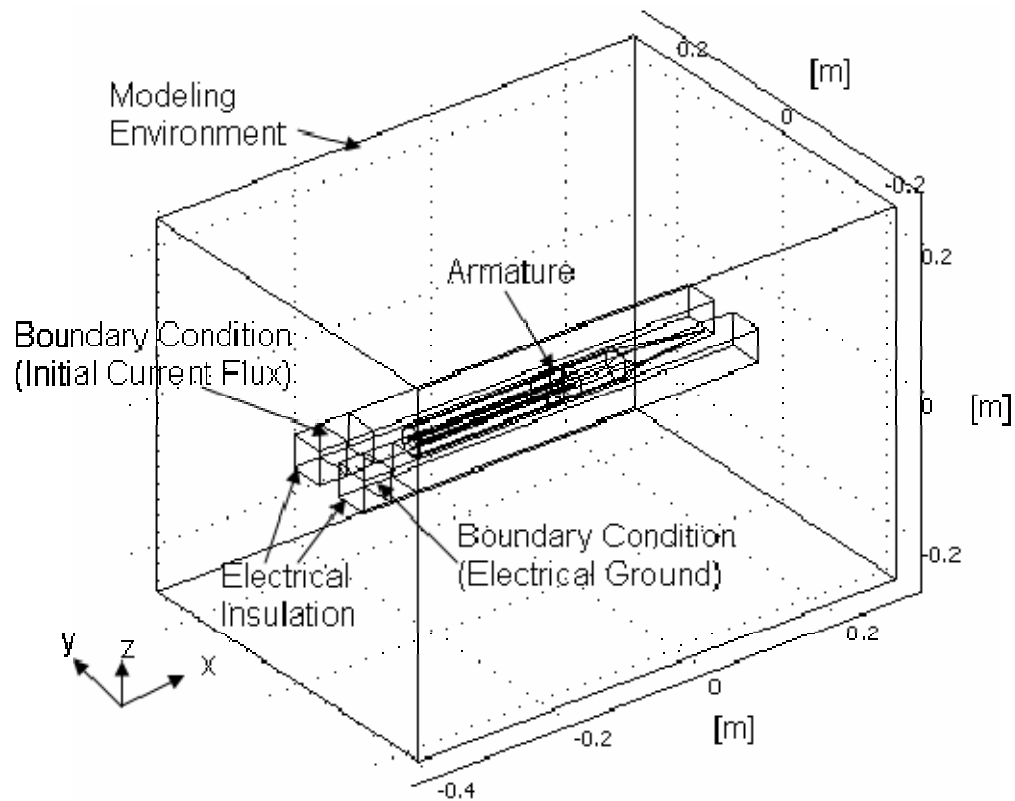
Figure 30.   3D Finite Element Model

The final six models, three for each design, were refinements to several previously investigated test models. The meshing of these models induced approximately 7×10^5 degrees of freedom, and the computer that I used for simulations had only a maximum random access memory (RAM) of 4 Gigabytes. During the execution of the initial DC test models, I observed that current arced between the conducting rails. Several attempts at eliminating this problem involved adding sufficient and non-disruptive electrical insulation to prevent arcing, but this problem persisted into the final set of models.   The current flux boundary condition that was supposed to induce an appropriate effective current in the test models did not create the same flux value at the projectile due to electrical arcing. However, I did observe a continuity of flux just after influx boundary and right before the electrical ground. I also observed a continuity of flux between both rails and the conductive contact surfaces of the projectiles. Therefore, I increased the value of the influx boundary to give the proper current through the projectiles. A summary of each model's setup parameters is given in Appendix F.

71

1.   Direct Current Model

The DC models for both designs show that current distributes itself throughout the tungsten and aluminum portions of the projectile. The modeling software allowed for post-processing of the final solutions. I was able to independently evaluate current flux through the contact surfaces of the aluminum armatures and the tungsten penetrators. Using Comsol's volume integration postprocessor, I was also able to evaluate the resistive energy lost to the aluminum armatures.   The volume integration evaluated the power dissipated to the armature in units of Watts.   In order to find the exact energy in Joules, I multiplied the volume integration results by the time of launch, $t_L = 5.45$ *ms*, and used basic thermodynamic relationships to estimate the average temperature rise in the armatures. The results of my analysis indicate an average temperature in the armature that is significantly below the melting point of aluminum.

Using Comsol's boundary integration postprocessor, I evaluated the current flux on each contact surface between the conducting rails and two design projectiles. The current through the 30mm projectile was 1.27 MA. Approximately 445 kA (35 %) of current passed through the aluminum armature and 825 kA (65 %) passed through the tungsten penetrator. My rough estimates for the current distribution were 32% and 68%, respectively.   The conductive portion of the 40mm projectile received a total current flux of 1.82 MA. The current distribution was 582 kA (32%) for the armature and 1.23 MA (68 %) for the penetrator. The 40mm projectile agreed exactly with the rough estimates for current distribution. Figure 31 shows the current distribution for the 30mm projectile, and Figure 32 shows a similar distribution for the 40mm projectile. The current distribution is shown with an arrow plot. Each arrow is a proportion of the magnitude of the current at its location. These figures also show the current densities on one *x-y* plane that cuts through the center of each projectile at *z=0*.
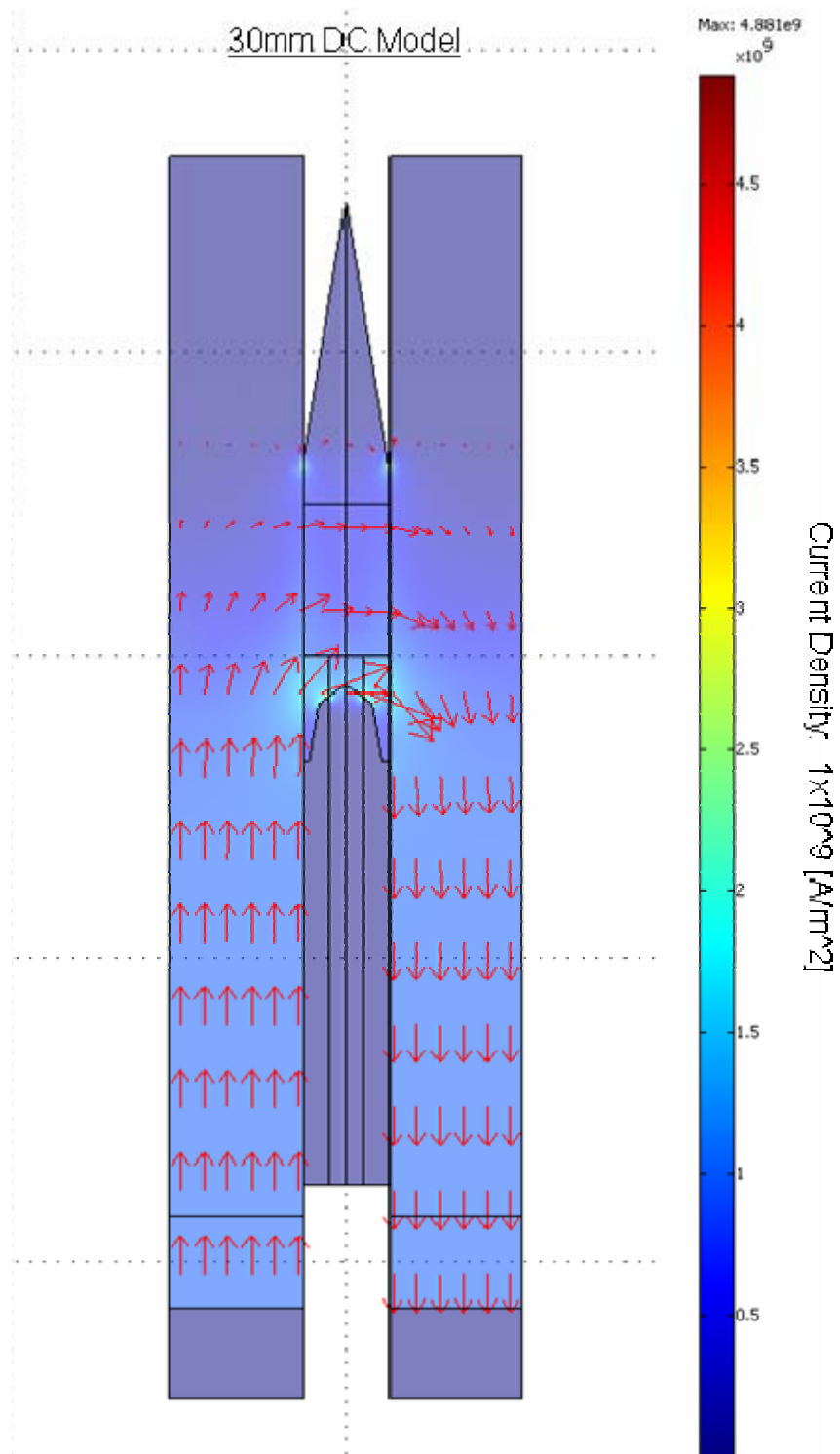
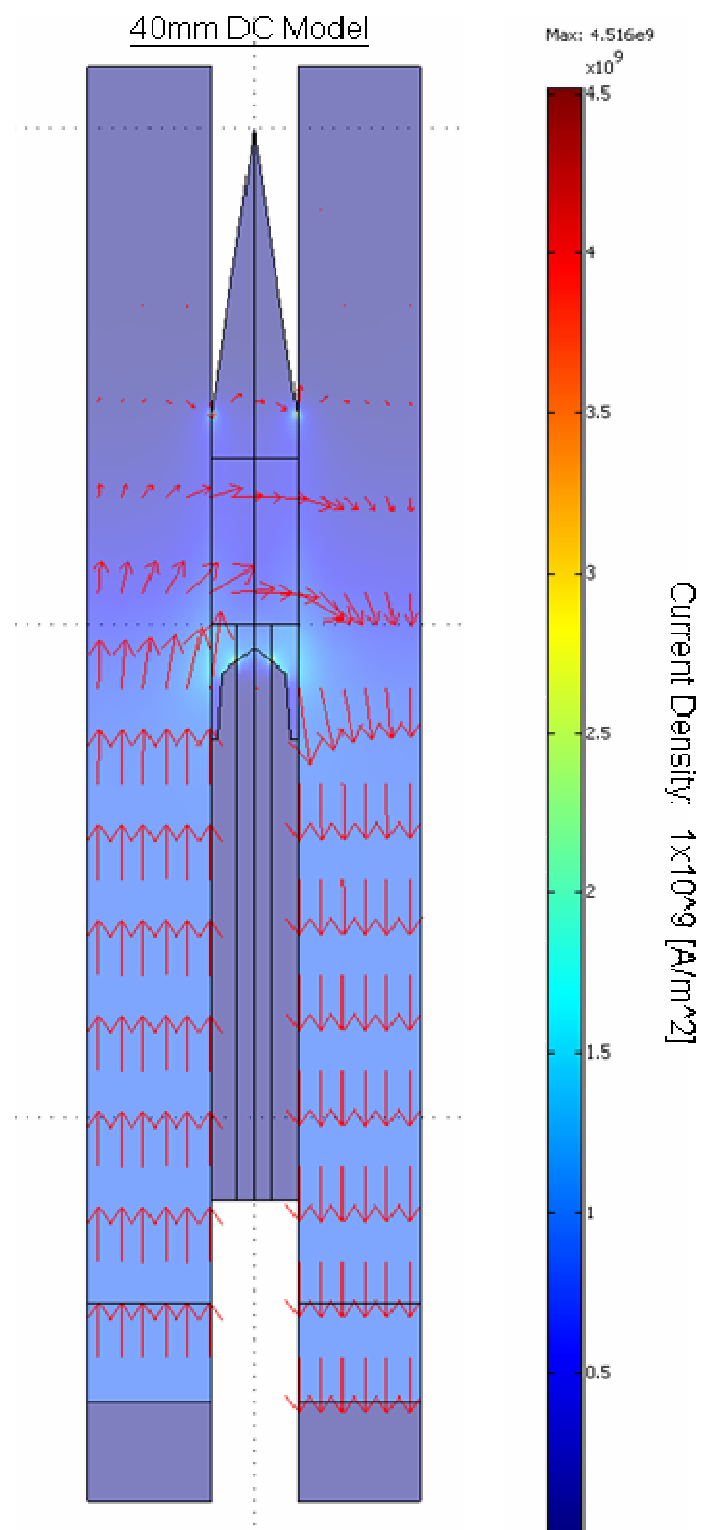Figure 31.   Current Distribution and Density in the DC Model (30mm Projectile)

Figure 32.   Current Distribution and Density in the DC Model (40mm Projectile)

I evaluated volume integrals with Comsol's postprocessor for the electrical power dissipated in the armatures. The dissipated power in the armatures was 668 kW and 1 MW for the 30mm and 40mm DC models, respectively. Multiplying these results by the theoretically estimated launch time of 5.45 ms, I was able to estimate the amount of energy, Q, lost to the armatures in the form of heat. This estimate shows that 3750 J of heat went into the 30mm armature, and that 5450 J went into the 40mm armature. The thermodynamic relationship for calculating the heat energy absorbed by solids or liquids is given by, $Q = c_p m \Delta T$; where c_p is the specific heat capacity, m is the mass, and ΔT is the average change in temperature. The specific heat capacity for the aluminum used in this design is 0.896 J/g-deg (See Appendix B1). The mass of the 30mm armature is 26.7 g, and for the 40mm armature it is 63.5 g (See Appendix B3). Using these values with the calculations for heat energy, I found that the ΔT in the 30mm armature was 157 °C and it was 96 °C in the 40mm armature. These values for ΔT are well below the melting point of aluminum.

2.   Magnetostatics Model

The purpose of the magnetostatics model was to test the validity of the distribution of current in the DC model. It used the output solution from the DC model to create a magnetic flux density, based upon the magnitude and direction of the volume current density within computational uncertainty. The resulting magnetic flux densities and field lines are in Figure 33 for the 30mm model and Figure 34 for the 40mm model. If the current distribution is correct, then the magnetostatics model should create a magnetic flux density that can induce a theoretical Lorentz force that is calculated from $F = L'I^2/2$, with L' from the Kerrisk method. The overall results for both railgun designs show agreement with L' to within 6%.

A quantifiable measure of validity is being able to produce the inductance gradient from the model's calculation for the Lorentz force. Using the railgun force law, one can solve explicitly for the inductance gradient with the following expression: $L' = 2F/I^2$. Comsol's postprocessor allows for a volume integral of $\vec{J} \times \vec{B}$ over any component of the railgun representation. Using the specific vector components of $\vec{J}$ and $\vec{B}$ that create a force in the launch direction, I evaluated the volume integration

function over the entire projectile. The results gave a force of 326 kN on the 30mm projectile and a force of 681 kN on the 40mm projectile. Again, the currents from the DC models were 1.27 MA and 1.82 MA, respectively. These remain unchanged and verifiable in the magnetostatics models. With the aforementioned values for force and current, I calculated $L' = 0.39$ μH/m for the 30mm railgun and $L' = 0.41$ μH/m for the 40mm railgun. These values indicate differences between the theory and the model of 2.6% and 5.1% within computational uncertainty for the respective railguns.
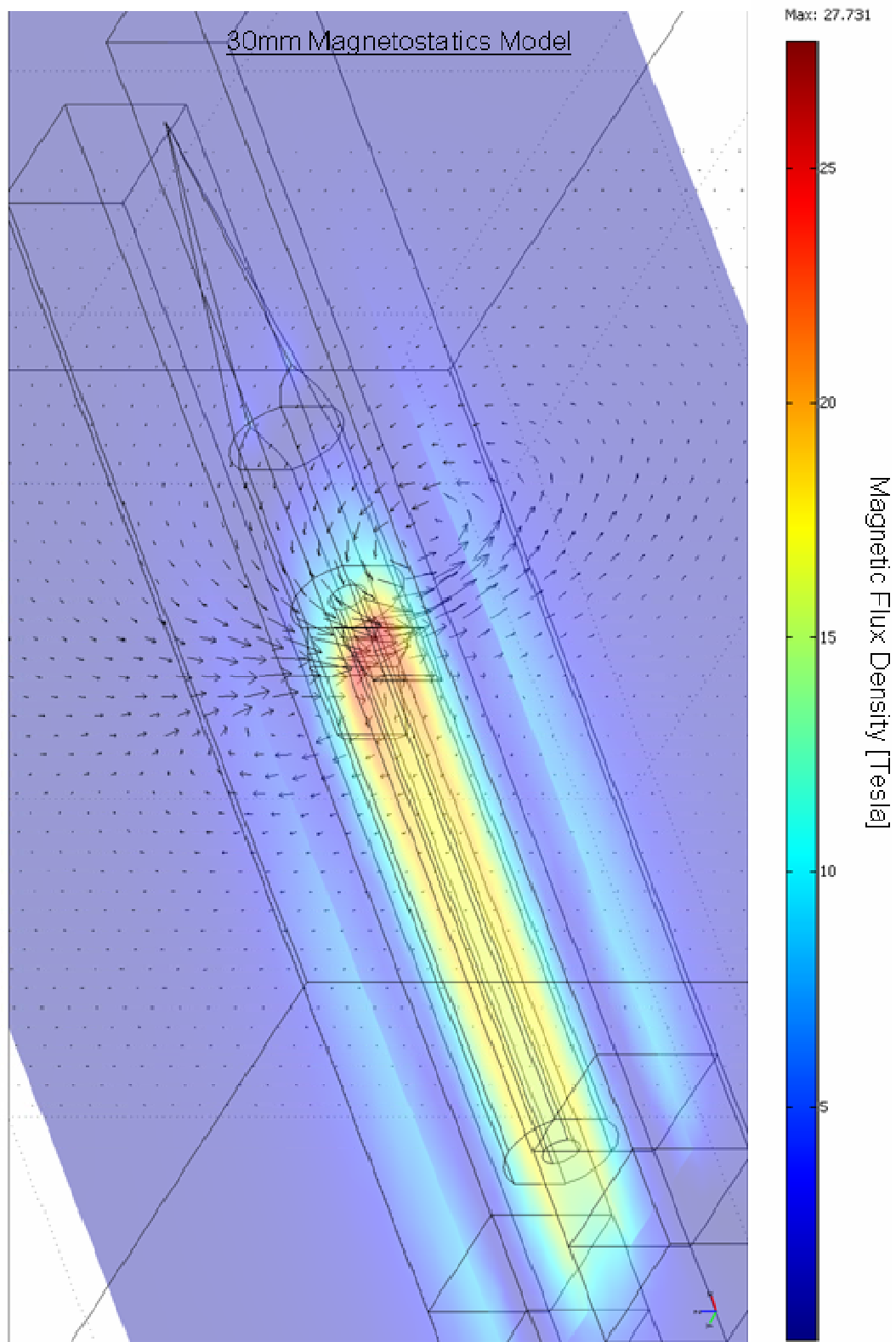
Figure 33.   Magnetic Flux Density and Field from the Magnetostatics Model (30mm)
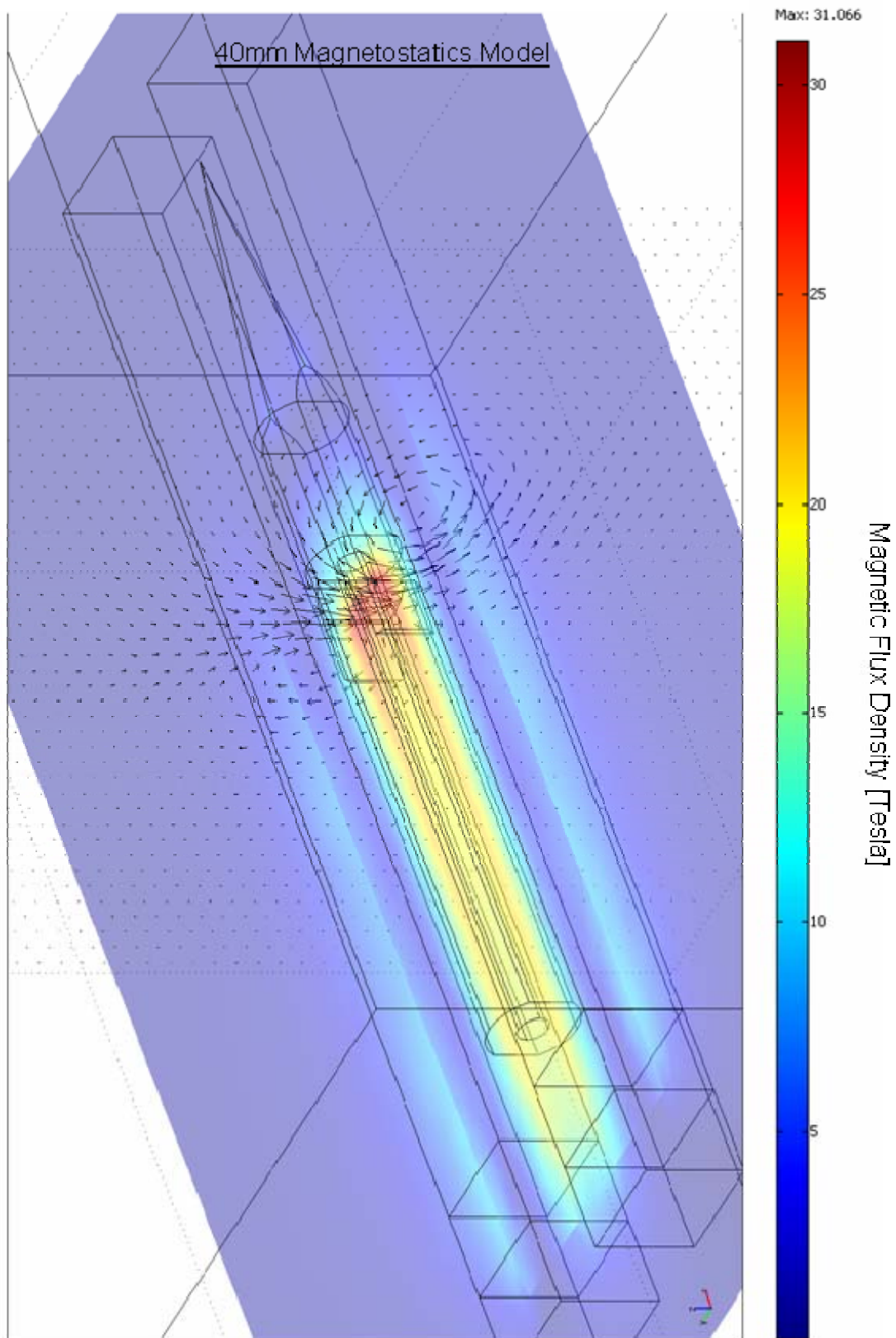
Figure 34.   Magnetic Flux Density and Field from the Magnetostatics Model (40mm)

3.   Transient Conductive Heat Transfer

The rough temperature estimates from DC model were not specific enough to show hot spots or areas of concern for the two armatures. I used the output solution from the DC model and an initial temperature of 30 °C to setup a transient model in order to calculate temperature increases over 5 ms. I also used a geometry isolation function within the Comsol modeling software to prevent any heat exchange between the rails and the projectile. This modeling analysis shows that a large majority of both armatures remain at temperatures well below the melting point for aluminum.

The required modification to the rear of the armature, in which I had to replace the smooth curvature with four surfaces, resulted in hot spots that exceeded the melting point of aluminum. It is reasonable to expect hot spots in situations involving current flow around edges. Overall, these hot spots only occur in roughly one percent of each armature's total volume. Taking into consideration the number of hot spots, their maximum temperature, and their location with respect to the surface modifications, I do not believe that they properly indicate melting in the armatures. The location of these hot spots, near the rear of the armatures, does produce a concern about the possible melting of the PBI insulator, which has a maximum service temperature of 500 °C. A design modification that could mitigate this concern would be to place a thin heat shield between the armature and the insulator. One can gain a better perspective on the hot spots and the general heating of the projectile by examining Figure 35 for the 30mm projectile and the Figure 36 for the 40mm projectile.
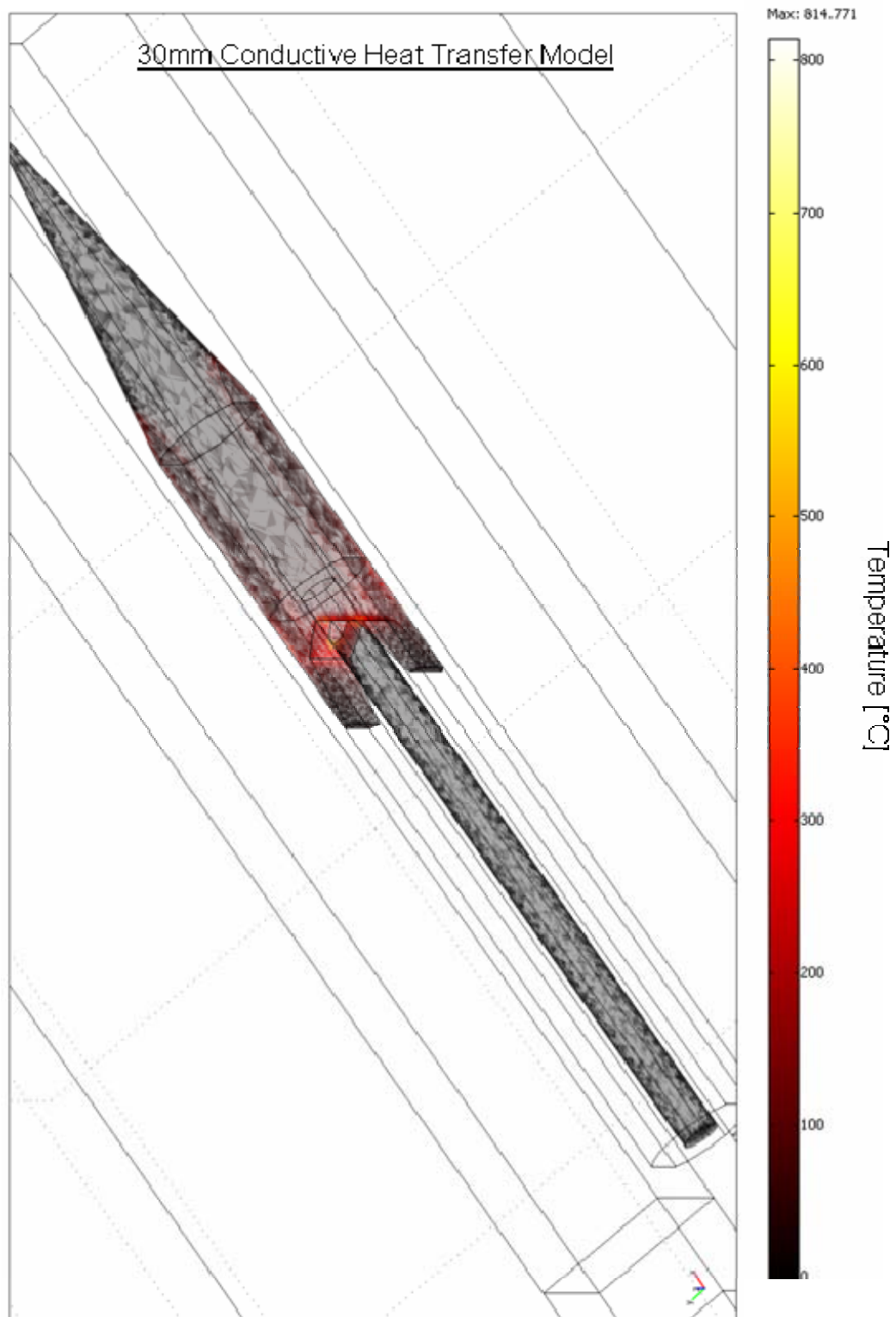
Figure 35.   Electrical Heating of 30mm Projectile after 5 ms
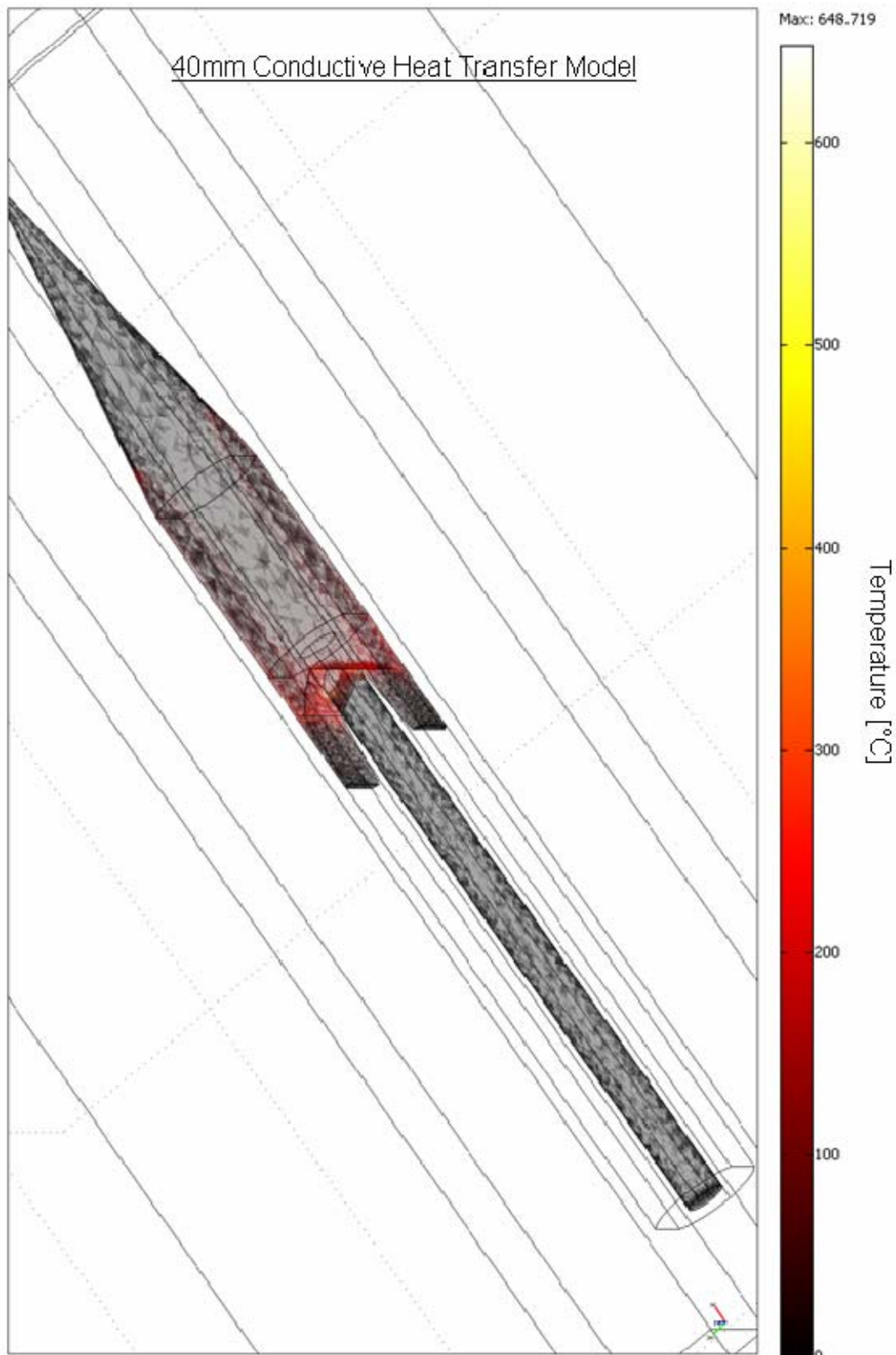
Figure 36.   Electrical Heating of 40mm Projectile after 5 ms

F.   EML CONCLUSIONS

The theoretical estimates and the temperature refinements from the computer modeling indicate that both design projectiles can conceptually achieve a launch velocity of 1100 m/s. This analysis shows that this velocity is attainable while satisfying the design constraints. There are specific details about the practicality of this design that need further consideration before full development and experimentation. This involves sliding contact and the achievability of the 40mm design's effective current. The sliding contact between a tungsten penetrator and the copper rails may induce quick barrel wear in this application. The tungsten penetrator does not have a mechanism to maintain contact. It must rely on barrel tension and contact with the aluminum armature to sustain a current flux. The estimated effective current required for the 40mm projectile is close to the design constraint of 2 MA. One needs to consider the achievability of this effective current with respect to the Army's version of the power supply for the FCS.   From a general perspective, the design concept for the electromagnetic launch of the two projectiles demonstrates the potential for a future system application.

V. DESIGN CONCLUSIONS

The research reported in this thesis shows the feasibility of designing a projectile suitable for use in urban warfare scenarios which does not produce potentially fratricidal components upon launch. The Infantry Railgun Projectile design concept creates a safer weapon for infantry forces. The most significant consequence of this self conducting projectile design is to create a deployable fin solution for aerodynamic stability. This thesis shows that the deployable fin design limits the maximum attainable velocity to 1100 m/s. The ballistics and electromagnetic launch analysis indicates that this velocity still allows for both projectiles to meet their design requirements. Only through future work and experimentation will all of these issues find more validity. Overall, the design presented is a rough concept, but as this analysis shows there are aspects of the projectiles that should interest Army weapons developers.

I was able to show the potential for design improvements throughout this analysis by maintaining a 30mm baseline projectile with a scaled 40mm version. One can identify how scaling affected each area in this design. In most weapons applications, the Army requires smaller and lighter equipment that performs just as well as larger and heavier versions. Between the two designs, the 30mm projectile is a more favorable choice because it met all the constraints of the design. However, there are areas where the 40mm projectile performed better. With the same launch velocity as the 30mm projectile, the 40mm projectile had less erosion and a higher residual velocity after penetrating the RHA target. It also suffered less aerodynamic drag because of its mass. The 40mm projectile showed less electrical heating during electromagnetic launch, even though it required a higher effective current. The benefits of the 30mm projectile are of a practical nature. Its effective current is 660 kA lower than the 40mm projectile, which requires less pulsing by the Army's CPA power supply. The 30mm projectile's size and effective current will allow for a thinner and lighter railgun barrel because those specifications require less containment material. If the Army chooses to conduct future development work on this design, the comparison of the two projectiles presented in this thesis should facilitate informed design improvements.

THIS PAGE INTENTIONALLY LEFT BLANK

APPENDIX

A. DESIGN CONSTRAINTS

1. The projectile penetrates medium armored vehicles

The projectile penetrates 100mm of Rolled Homogeneous Armor (RHA) with a normal incidence obliquity angle at a distance of 2 km. Using my own investigation of contemporary medium caliber munitions, I assume that a successful penetration of this target by an armor penetrator demonstrates that it is effective against medium armored vehicles [17].

2. The projectile is multipurpose

The projectile penetrates 200mm of Double Layered Reinforce Concrete (DLRC) with a normal incidence obliquity angle at a distance of 500 m, and creates a perforation hole diameter larger than 15mm. An ARL report states that a 200mm DLRC target represents a typical urban target [19]. In order for the design projectile to satisfy the perforation requirement, it needs to have a body diameter of at least 15mm. I derived the specification for the 15 mm perforation thickness from approximate body diameters of Bradley's M793 TP-T training round, which is shown in Figure 37. Bradley IFV gunners believe this round is the most effective against concrete [11].
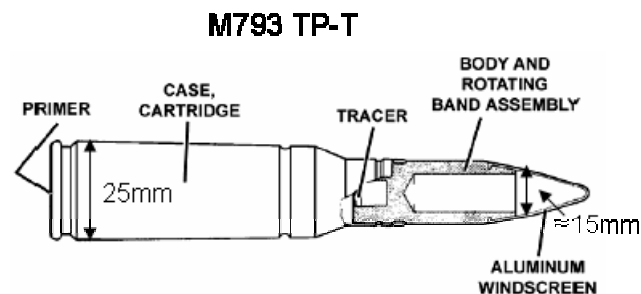
Figure 37. M793 (After Ref. [11])

3. The projectile is aerodynamically stable to provide precise trajectories

The projectile must have at least neutral pitch and yaw stability. This minimum requirement will allow for aerodynamic modifications to improve the static margin to acceptable values. Static margin values $\geq 10\ \%$ will create precise trajectories [31].

4. The projectile minimizes SDZs for forward dismounted infantry

No parasitic mass falls away from the projectile after launch. A projectile that does not eject any launch package components during flight will minimize Surface Danger Zones for forward positioned dismounted infantry. One can examine the impact of having fall-away launch components by examining the Army's restrictions for the Bradley's APFSD round in Figure 38.
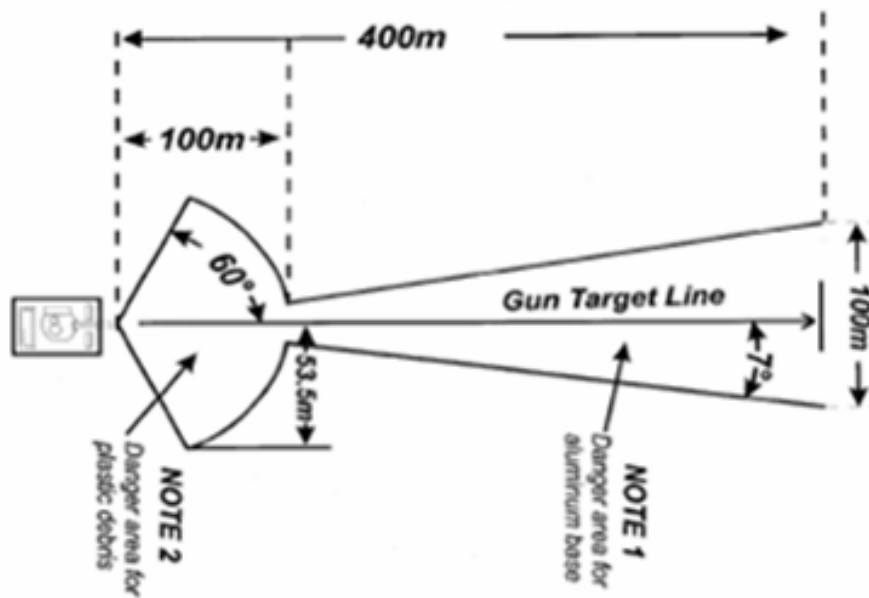
Figure 38.   SDZ Restrictions for a Bradley APFSD Projectile (From Ref. [12])

5. The projectile must have smooth and flat sides for the railgun

The physical design of the projectile must incorporates geometries to maintain electrical contact with rectangular conducting rails. The circular cylindrical geometry of the projectile has shaved sides to fit the rectangular configuration of the barrel. The aluminum armature has an inverted "U" shape cut into its base to allow the electromagnetic force to push the armature against the rails.

86

6. The projectile must allow for feasible auto-loading

Using an ARL concept for the FCS, shown in Figure 39, I have assumed that the maximum length of the ammunition storage compartment is 600mm. The ARL concept includes an autoloader. Therefore, the maximum length of the projectile can be no longer than 600 mm [2].
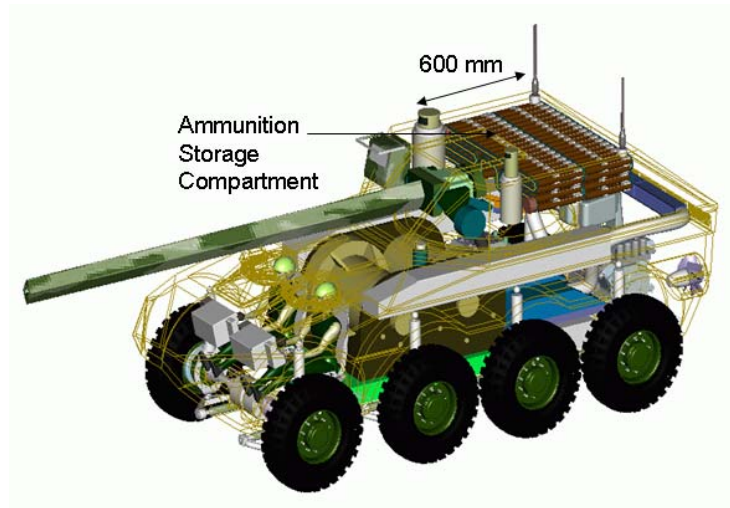
Figure 39.   ARL Concept for FCS (After Ref. [2])

7. The railgun's maximum average current is less than 2 Mega Amps

The primary power supply candidate for the Army's version of the FCS has one pair of Compensated Pulsed Alternators, shown in Figure 40. The individual peak current for each alternator is 1.08 MA. One could set the pulsing of the two alternators to get an effective current of approximately 2 MA.

Figure 40.   ARL Concept for CPA (After Ref. [2]).

8. The conducting rails maximum length is no longer than 3 meters

The barrel length restriction for the FCS is approximately 3 meters. This estimate is based upon a barrel that is roughly one-third the maximum vehicle length for the FCS, which is eight meters [5]. This FCS version comes from Armor Magazine and is shown is Figure 41.
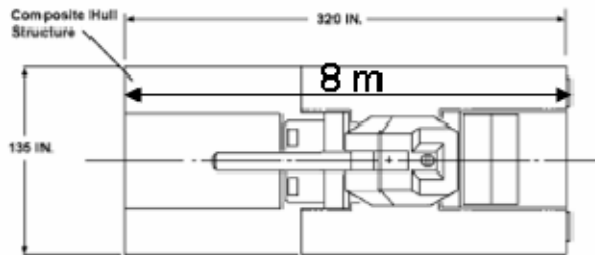
Figure 41.   Armor Concept for FCS (After Ref. [6])

9. The conducting rails can sustain 10 continuous shots without melting

A proposed rate of fire for the Navy's railgun design is 12 rounds per minute [9]. A naval railgun has the ability to eject heat into the ocean and can use large cooling systems. The Army's proposed design for the FCS does not include a cooling system and has a limited ability to eject heat [2]. A 20 degrees temperature change per shot in the copper conducting rails will keep the average temperature of the rails below 500 °C after 20 shots. The melting point of the aluminum armature is 652 °C, and the maximum service temperature for the PBI insulator is 500 °C. If the conducting rails reach temperatures above 500 °C, there is a possibility that the PBI insulator will melt while the projectile is being prepared for launch. These design characteristics limit the rate of fire to 10 rounds per minute for two minutes.

B.   PROJECTILES

The purpose of this appendix is to describe the 30mm and scaled 40mm design projectiles. The component overview identifies each major component with respect to design titles and material properties [15]. In following sections, I describe the geometric parameters and dimensional properties for each component. I design both projectiles with a Computer Aided Design software called Rhinoceros. This software allows for specific length and volume calculations [14]. This appendix ends with my calculations for the total mass and the center of mass of each design projectile.

1.   Component Overview
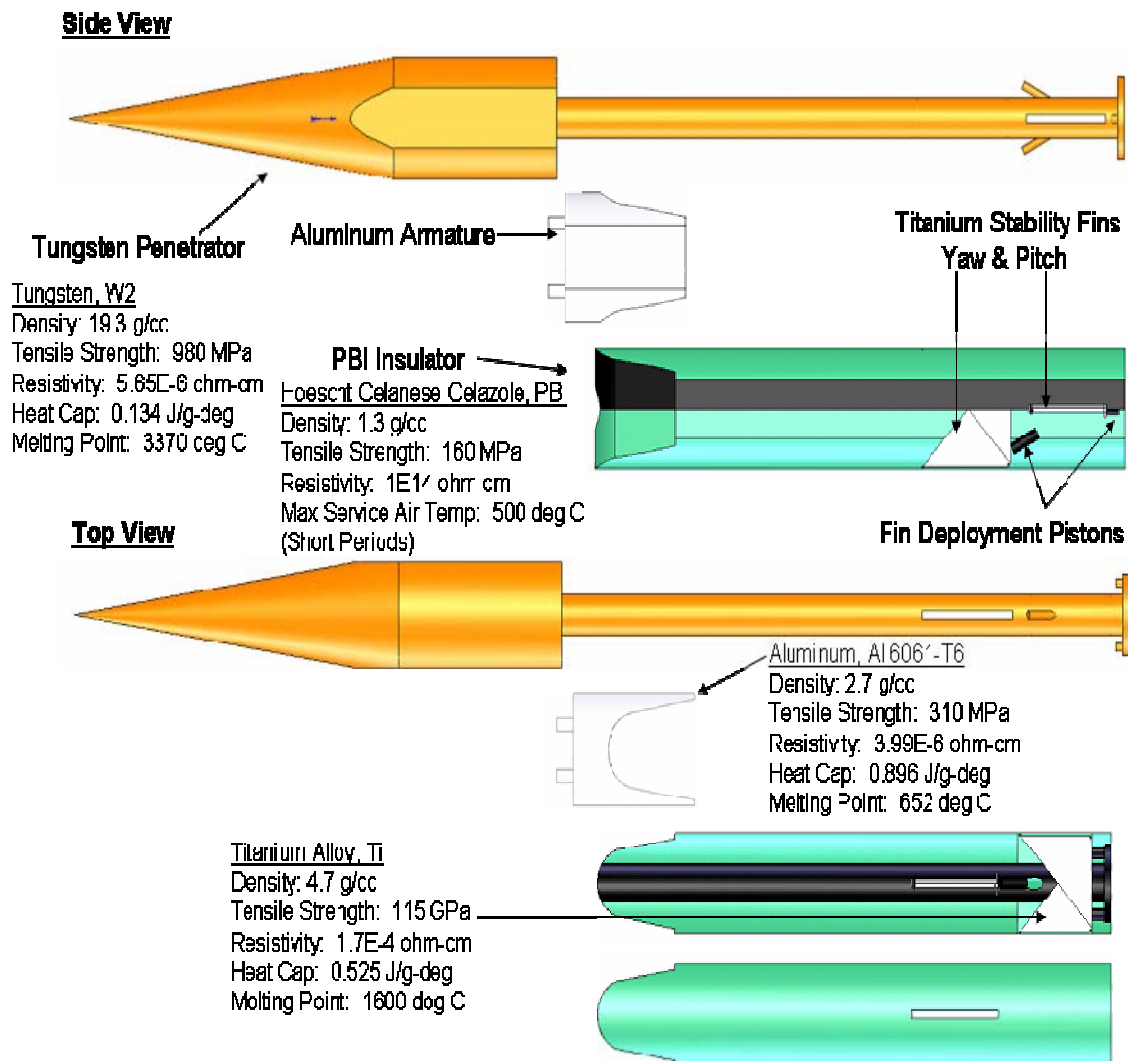
Figure 42.   Design Projectile Component Overview

2. Tungsten Penetrator
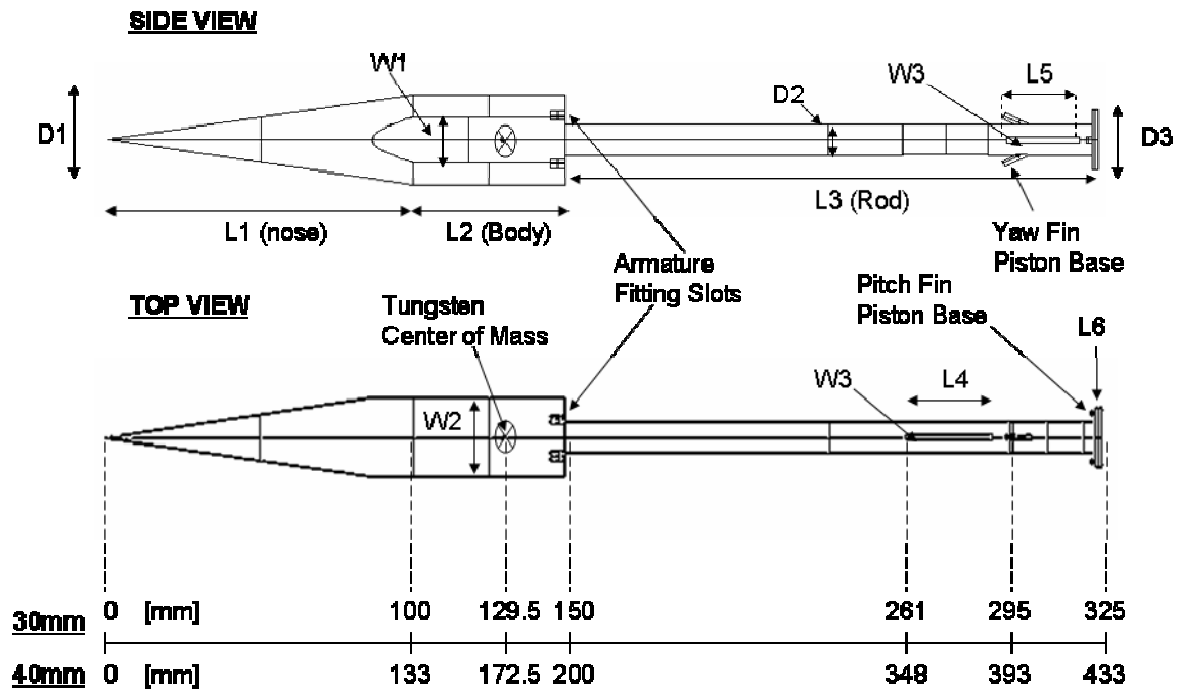
Figure 43.   Tungsten Penetrator

Variable	Units	Description	30 mm Penetrator	40 mm Penetrator
D1	mm	Primary Diameter	30	40
D2	mm	Rod Diameter	10	13.3
D3	mm	Base Plate Diameter	20	26.7
L1	mm	Nose Length	100	133.3
L2	mm	Body Length	50	66.7
L3	mm	Rod Length	175	233.3
L4	mm	Yaw Fin Slot Length	28	37.3
L5	mm	Pitch Fin Slot Length	24	32
L6	mm	Base Plate Thickness	2	2.7
W1	mm	Shave Side Height	15	20
W2	mm	Body Width	26	34.7
W3	mm	Fin Slot Width	2	2.7
V_W2	cm^3	Total Volume	69.76	165.4
M_W2	g	Total Mass	1346	3192
CM_W2	mm	Center of Mass	129.5	172.5

Table 12.   Penetrator Dimensions

90

3. Aluminum Armature
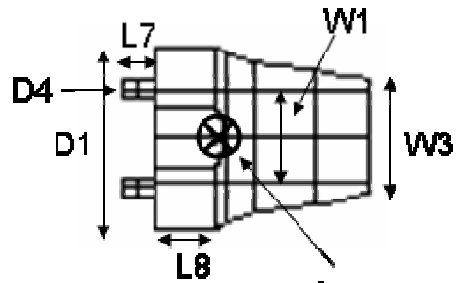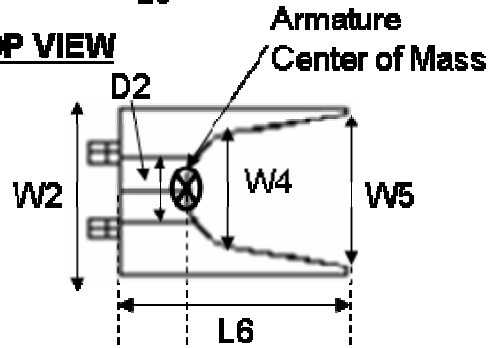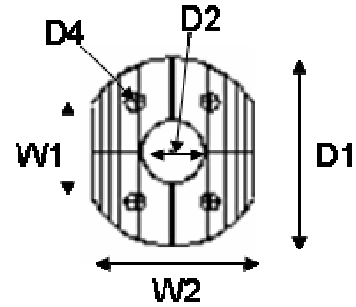
Figure 44. Aluminum Armature

Variable	Units	Description	30 mm Armature	40 mm Armature
D1	mm	Primary Diameter	30	40
D2	mm	Rod Diameter	10	13.3
D4	mm	Connector Diameter	3	4
L6	mm	Armature Length	35	46.7
L7	mm	Connector Length	5	6.67
L8	mm	Armature Thickness	10	13.3
W1	mm	Shaved Side Height	15	20
W2	mm	Body Width	26	34.7
W4	mm	Interior Minor Width	17.3	23
W5	mm	Interior Major Width	23.4	31.2
V_AL	cm^3	Total Volume	9.9	23.5
M_AL	g	Total Mass	26.7	63.5
CM_AL	mm	Center of Mass	160	213.3

Table 13. Armature Dimensions

4. Insulator
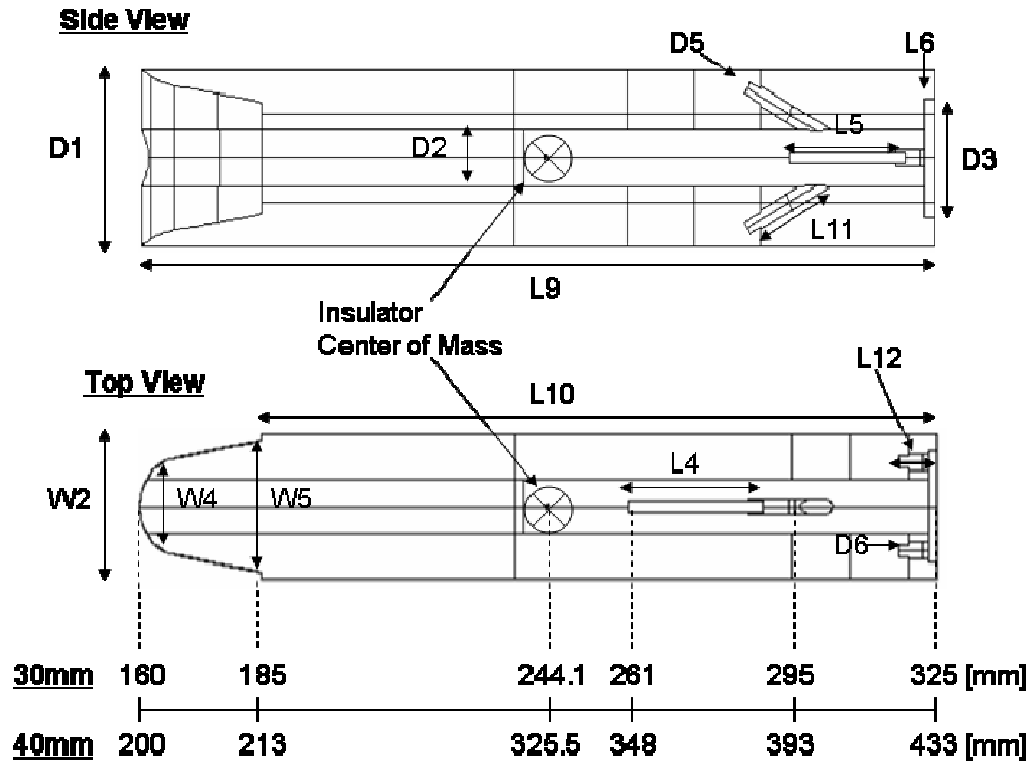
Figure 45.   Insulator Configuration

Variable	Units	Description	30 mm Insulator	40 mm Insulator
D1	mm	Primary Diameter	30	40
D2	mm	Rod Diameter	10	13.3
D3	mm	Base Plate Diameter	20	26.7
D5	mm	Yaw Piston Diameter	3	4
D6	mm	Pitch Piston Diameter	3	4
L4	mm	Yaw Fin Slot Length	28	37.3
L5	mm	Pitch Fin Slot Length	24	32
L6	mm	Base Plate Thickness	2	2.7
L9	mm	Insulator Length	165	220
L10	mm	Insulator Body Length	140	186.7
L11	mm	Yaw Piston Length	16	21
L12	mm	Pitch Piston Length	6	8
W2	mm	Body Width	26	34.7
W4	mm	Interior Minor Width	17.3	23
W5	mm	Interior Major Width	23.4	31.2
V_INS	cm^3	Total Volume	90.5	214.5
M_INS	g	Total Mass	117.7	278.9
CM_INS	mm	Center of Mass	244.1	325.5

Table 14.   Insulator Dimensions

5. Stability Fins
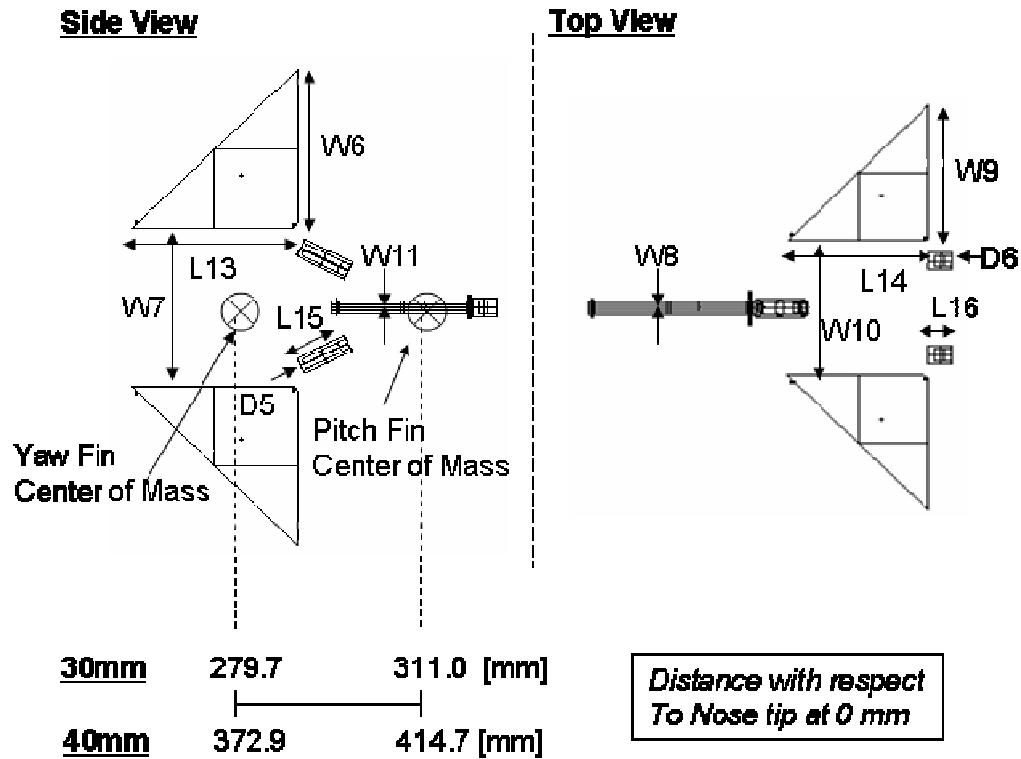
Figure 46. Stability Fin Configuration

Variable	Units	Description	30 mm Fins	40 mm Fins
D5	mm	Diameter Yaw Piston	3	4
D6	mm	Diameter Pitch Piston	3	4
L13	mm	Yaw Fin Length	28	37.3
L14	mm	Pitch Fin Length	24	32
L15	mm	Yaw Piston Head	8.9	11.9
L16	mm	Pitch Piston Head	4	5.3
W6	mm	Yaw Fin Width	27	36
W7	mm	Yaw Fin Separation	27	36
W8	mm	1 Yaw Fin Thickness	1	1.3
W9	mm	Pitch Fin Width	23	30.7
W10	mm	Pitch Fin Separation	23	30.7
W11	mm	1 Pitch Fin Thickness	1	1.3
V_YF	cm^3	Total Volume, Yaw	0.758	0.898
M_YF	g	Total Mass, Yaw	3.6	8.4
V_PF	cm^3	Total Volume, Pitch	0.553	0.655
M_PF	g	Total Mass, Pitch	2.6	6.2
CM_YF	mm	Center of Mass, Yaw	279.7	372.9
CM_PF	mm	Center of Mass, Pitch	311	414.7

Table 15. Stability Fin Dimensions

6. Total Mass

$$M_T = M_{W2} + M_{AL} + M_{INS} + M_{YF} + M_{PF}$$

30 mm Projectile: Total Mass = 1497 grams or 1.50 kg

40 mm Projectile: Total Mass = 3549 grams or 3.55 kg

7. Center of Gravity

$$\overline{X}_{CG} = \frac{1}{M_T}(M_{W2}CM_{W2} + M_{AL}CM_{AL} + M_{INS}CM_{INS} + M_{YF}CM_{YF} + M_{PF}CM_{PF})$$

30 mm Projectile: Center of Gravity = 139.7 mm

40 mm Projectile: Center of Gravity = 186.2 mm

C.   RAILGUN BARRELS

The purpose of this appendix is to describe the railgun barrels for this thesis research.   The general concept of the barrel comes from an Institute for Advanced Technologies presentation by Dr. Mark Crawford [8]. I have slightly modified the IAT generic design to include a ceramic insulator. The configuration of the barrel and material properties are shown in Figure 47 [15].
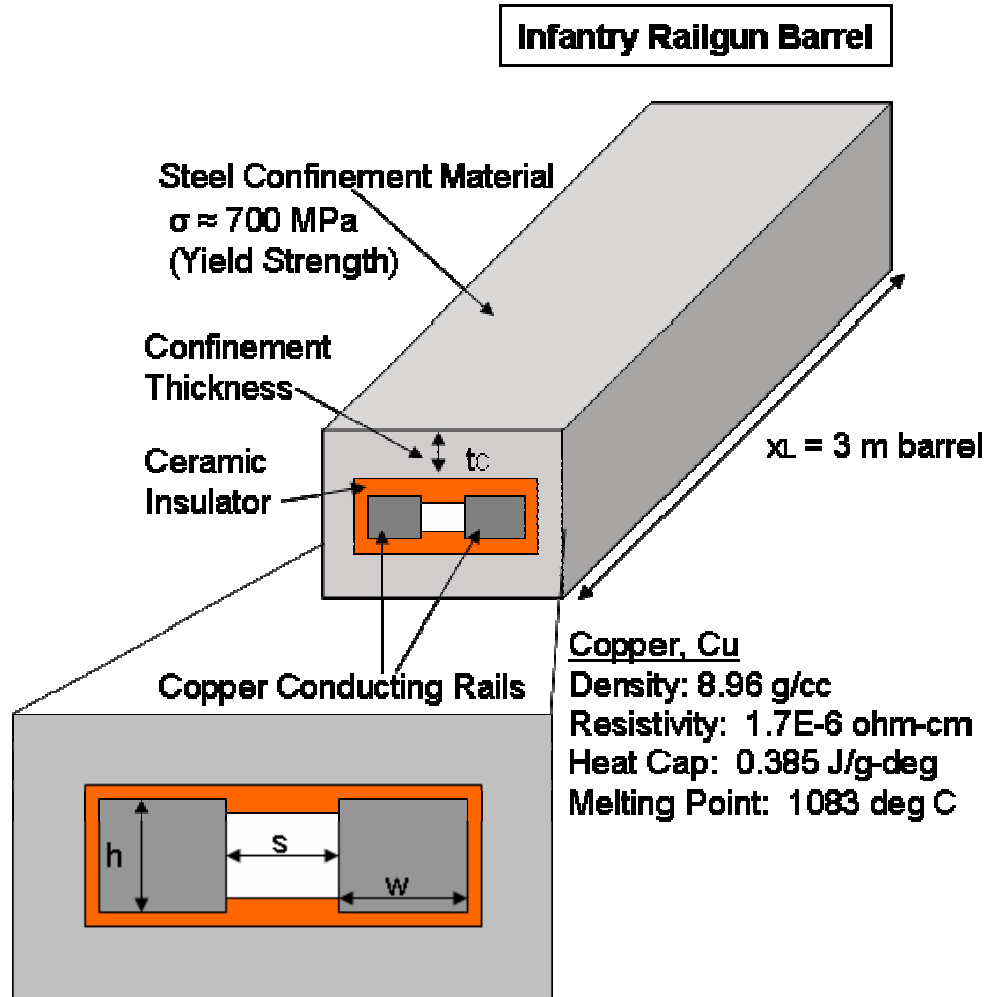
Figure 47.   Generic Rectangular Railgun Barrel

The railgun force law, a function of inductance gradient and effective current, allows one to calculate the theoretical force on a projectile. This equation is shown in the following expression: $F = L'I^2/2$; where L' is the inductance gradient and I is the effective current. Railgun designers commonly use the Kerrisk Method to calculate the

inductance gradient for a single pair of square or rectangular conducting rails [35]. The semi-empirical relationship for the Kerrisk Method is shown in Figure 48.

<u>Cross-section of Conducting Rails</u>

<u>Kerrisk's Parameters</u>

$$A := 0.44061$$
$$B := (-) 0.0771$$
$$a1 := 3.397143$$
$$a2 := (-) 0.06603$$
$$b1 := 1.007719$$

Vacuum Inductance Gradient Estimates, Kerrisk's Method, LANL report LA-9092-MS, NOV 1981:

$$b2 := 2.743651$$
$$b3 := 0.022093$$
$$b4 := 0.263739$$

$$L' = \left[A + B \ln \left(1 + a1\frac{w}{h} + a2\frac{w}{h}\frac{s}{h} \right) \right] \ln \left[b1 + b2\frac{s}{h} + b3\frac{w}{h} + b4\frac{s}{h}\frac{w}{h} \right]$$
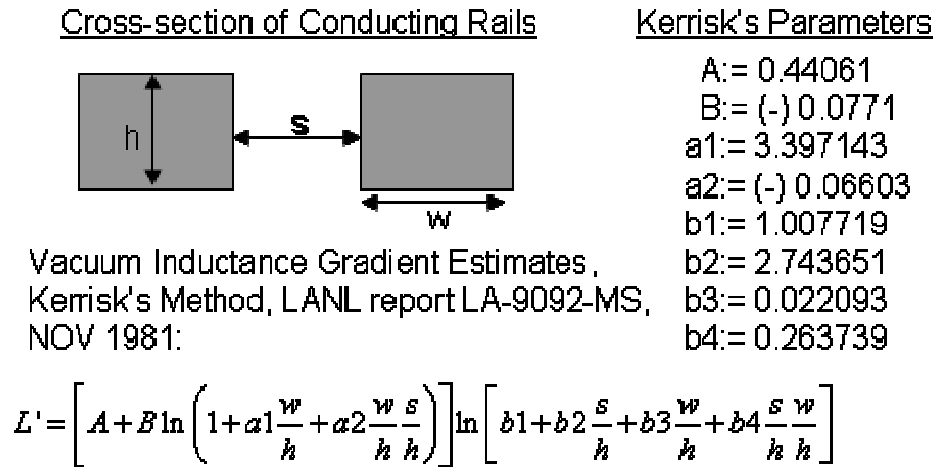
Figure 48.   Kerrisk Method for Calculating Inductance Gradients

96

D. BALLISTIC ANALYSIS

1. AUTODYN 5.0 Modeling Set-up for MOD-2 Impacting RHA

I used the following AUTODYN model setup for the 30mm and 40mm MOD-2 projectiles impacting into the 100mm RHA target [25]. A general understanding of the AUTODYN graphical user interface is necessary to comprehend the setup summary. All input values for MOD-2 come from Figure 4 in Chapter II. All input values for RHA come from Figure 5 in Chapter II.

> ##### a. Modeling Domain

-Select the two-dimension (2D) modeling perspective.

{The x-axis is oriented from left to right, and the y-axis is oriented from bottom to top with respect to graphical images on a normal computer monitor}

> ##### b. Load Materials

> ###### [1] Tungsten

-Select tungsten from the material library.

-Ensure that the equation of state is "Linear-Von Mises."

-Change material density to 19.3 g/cc.

-Change Bulk Modulus to 3.1E8 kPa.

-Select Failure Model and input 0.005 for the Plastic Strain.

{The Plastic Strain is approximately the Yield Stress, 1.51E6 kPa, divided by the Bulk Modulus, 3.1E8 kPa.}

> ###### [2] RHA

-Select RHA from the material library.

-Ensure that the equation of state is "Linear-Von Mises."

-Change the Bulk Modulus to 1.7E8 kPa.

-Select the Erosion Model and input 2 for the Erosion Strain.

{A Century Dynamics AUTODYN technical advisor recommended the value of 2 for the Erosion Strain [39].}

-Select Failure Module and input 0.008 for the Plastic Strain.

{The Plastic Strain is approximately the Yield Stress, 1.32E6 kPa, divided by the Bulk Modulus, 1.70E8 kPa.}

> ##### c. Create Parts

> ###### [1] Block 1 and 2 (MOD-2 Rod Cylinder and Body Cylinder)

-Select the Block geometry and fill with Tungsten.

{One must select individual Blocks for the Rod Cylinder and Body Cylinder. One can identify these geometries from the MOD-2 reference figure. The placement of block with respect to the x,y origin depends upon the preference of the user. The user must ensure that the Rod Cylinder Block is to the left of the Body Cylinder Block, and that the inner boundaries of the two blocks make contact.}

-Input dimensions for length, x-direction, and width, y-direction. These values are based upon half-plane 2D axial symmetry along the x-axis.

{All values for length, x, are the actual lengths that one can find from the MOD-2 reference figure. All values for width, y, are the radial distances from the major-body axis or half diameters in the MOD-2 reference figure.}

-Input zoning that is two times the values entered for length, $\Delta x=2x$, and width, $\Delta y=2y$.

-Input initial velocities which are the estimated impact velocities of MOD-2.

{One can find the estimated impact velocities in Table 9}

[2]   Rhombus (MOD-2 Nose)

-Select the Rhombus geometry and fill with Tungsten.

-Select the Quarter Rhombus representation.

-Input dimensions for the width, x-direction, and height, y-direction. These values are based upon dimensions for a full rhombus.

{All values for width, x, are two times the actual lengths of the noses that one can find from the MOD-2 reference figure. All values for height, y-direction, are full diameters of the noses that one can find from the MOD-2 reference figure. The user must position the Rhombus such that the center body coordinates aligns with the bottom right edge of the Body Cylinder Block.}

-Input zoning for "Across" that are equal to the diameters of the Body Cylinders from the MOD-2 reference figure.}

-Input initial velocities which are the estimated impact velocities of MOD-2.

{One can find the estimated impact velocities in Table 9}

[3]   Join All

-Select Join All for the Rod Cylinder Block, the Body Cylinder Block, and the Nose Quarter Rhombus.

[4]   Block 3 (RHA Target)

-Select the Block geometry and fill with RHA.

{The placement of this block must ensure that a 1mm gap is between the tip of the nose, which is to the left, and the bottom left corner of this geometry.}

-Input dimensions for length, x-direction, and width, y-direction. These values are based upon half-plane 2D axial symmetry along the x-axis.

{All values for length, x, are the actual lengths that one can find from the RHA reference figure. All values for width, y, are the radial distances from the major-body axis or half diameters in the RHA reference figure.}

-Input zoning that is two times the values entered for length, Δx=2x, and width, Δy=2y.

-Input an initial velocity of zero for this geometry.

        d.   *Boundary Conditions*

-Create a Transmit boundary.

-Select "Boundary Line" and place in the x-direction along the top of the RHA geometry.

        e.   *Rotate Model*

-Select "Rotate-270 degree" and "Axial-Symmetric."

{This action will take the current 2D half-plane axial symmetry and make a three-quarter 3D figure. All AUTODYN computations are evaluated in the 2D half plane and then mapped to the 3D axial symmetric figure}

        f.   *Start Simulation*

2.   AUTODYN 5.0 Modeling Set-up for MOD-2 Impacting DLRC

I used the following AUTODYN model setup for the 30mm and 40mm MOD-2 projectiles impacting into the 200mm DLRC target. Several input parameters in this model are exactly the same as the input parameters for the AUTODYN RHA model. I reference the RHA model in cases where there is exact replication by stating, "No Change from RHA Model." A general understanding of the AUTODYN graphical user interface is necessary to comprehend the setup summary. All input values for MOD-2 come from Figure 4 in Chapter II. All input values for DLRC target come from Figure 7 in Chapter II.

        a.   *Modeling Domain* [No Change from RHA Model}

        b.   *Load Materials*

            [1]   Tungsten [No Change from RHA Model]

            [2]   Concrete-L

-Select Concrete-L from the material library.

-Ensure that the equation of state is "Porous."

            [3]   Steel 4340

-Select Steel 4340 from the material library.

-Ensure that the equation of state is "Linear-Johnson Cook."

    c.   *Create Parts*

        [1]   Block 1 and 2 (MOD-2 Rod Cylinder and Body Cylinder)
[No Change from RHA Model]

        [2]   Rhombus (MOD-2 Nose) [No Change from RHA Model]

        [3]   Join All [No Change from RHA Model]

        [4]   Block 3 (Concrete-L Target)

-Select the Block geometry and fill with Concrete-L.

{The placement of this block must ensure that a 1mm gap is between the tip of the nose, which is to the left, and the bottom left corner of this geometry.}

-Input dimensions for length, x-direction, and width, y-direction. These values are based upon half-plane 2D axial symmetry along the x-axis.

{All values for length, x, are the actual lengths that one can find from the DLRC reference figure. All values for width, y, are the radial distances from the major-body axis or half diameters in the DLRC reference figure.}

-Input zoning that is two times the values entered for length, $\Delta x = 2x$, and width, $\Delta y = 2y$.

-Input an initial velocity of zero for this geometry.

-Select the Fill function.

{This additional Fill is to add one of the two Steel 4340 reinforcement bars.}

-Select Ellipse and fill with Steel 4340.

-Input an origin for the ellipse that is 26mm from the left edge and 145mm from the bottom of Block 3.

-Input 6.5mm for the ellipse's semi-major and minor axis.

-Select the Fill function.

{This additional Fill is to add the other Steel 4340 reinforcement bar.}

-Select Ellipse and fill with Steel 4340.

-Input an origin for the ellipse that is 177mm from the left edge and 145mm from the bottom of Block 3.

-Input 6.5mm for the ellipse's semi-major and minor axis.

    d.   *Boundary Conditions*

-Create a Transmit boundary.

-Select "Boundary Line" and place in the x-direction along the top of the Concrete-L geometry.

e.   *Rotate Model*

-Select "Rotate-270 degrees" and "Axial Symmetric."

{This action will take the current 2D half-plane axial symmetry and make a three-quarter 3D figure. All AUTODYN computation are evaluated in the 2D half plane and then mapped to the 3D axial symmetric figure}

f.   *Start Simulation*

3.   Critical Analysis Calculations

The critical analysis theoretical method is a variant of the Tate Model for sub-hydrodynamic rod penetration. In this section of the appendix, I develop the primary relationships that one needs to make calculations with the critical analysis method. The primary reference for this analytical technique is the course notes from PH4857 [26]. The Department of Physics at the Naval Postgraduate School currently teaches PH4857 as a primary course requirement for the curriculum of Applied Physics in Weapons.

a.   *Cavity Propagation Speed and Critical Velocity*

[1]   The first step in this analytical technique is to determine if the material strength of the projectile is larger than the material strength of the target, $Y_P > R_T$.   One can use the ultimate yield stress of a material to approximate the material strength.   The yield stress of tungsten is 1.51 GPa, and the yield stress of RHA is 1.32 GPa [27]. Using these values for material strength, we can conclude that the material strength of tungsten, Y_P, is in fact greater than the material strength of RHA, R_T.

[2]   Given the case where our comparison of material strength satisfies the relationship of $Y_P > R_T$, we can calculate the cavity propagation speed, V_T. The relationship for the cavity propagation speed is based upon the pressure balance equation in Figure 18 and is approximated by the following equation:

$$V_T = \frac{V_S}{1+\mu} \frac{1-\mu\sqrt{1-\frac{V^2}{V_S^2}\left(1-\mu^2\right)}}{1-\mu}$$; where V_S is the impact velocity of the

projectile, μ is the square root of the ratio between the density of the target material and the projectile material ($\mu \equiv \sqrt{\rho_T/\rho_P}$),   and V_- is the first critical velocity

$(V_-^2 \equiv 2(Y_P - R_T)/\rho_T)$.   The input values for the cavity propagation relationship, and the results are shown in Table 16.

Variable	Units	Description	30 mm Projectile	40 mm Projectile
V_S	m/s	Impact Velocity	828	890 m/s
Y_P	GPa	Material Strength of Projectile	1.51	1.51
R_T	GPa	Material Strength of Target	1.32	1.32
ρ_p	kg/m^3	Density of Projectile (Tungsten)	19300	19300
ρ_T	kg/m^3	Density of Target (RHA)	7850	7850
μ	----	Target-Projectile Density Ratio	0.64	0.64
V_-	m/s	First Critical Velocity	220	220
V_T	m/s	Cavity Propagation Speed	522.5	561.7

Table 16.   Cavity Propagation Speed Inputs and Results

b.   Penetration Depth at Critical Velocity

[1]   In order to create an equation for the penetration depth as a function of velocity, one must first consider the penetration depth as a function of time. We can assume that the penetration depth is limited by the cavity propagation speed. Therefore, the following integral can adequately approximate the penetration depth: $P(t) = \int_0^t V_T(t')dt'$.   We can manipulate this relationship to represent the penetration depth as a function of velocity by making the following substitution:

$V_T(t')dt' = -\dfrac{\rho_p}{Y_P} l(v')V_T(v')dv'$; where $l(v')$ is the un-eroded penetrator length as a function of velocity and dv' is the incremental change in velocity. The fundamental concept that allows one to make this substitution comes from the assumption that the elastic-plastic interface within the projectile is decelerating the remaining un-eroded penetrator. This assumption is summarized in the following force balance relationship:

$-Y_P A_P = \rho_p l A_P \dfrac{dv_P}{dt}$; where A_P is the cross-sectional area of the penetrator, l is the un-eroded penetrator length behind the elastic-plastic interface within the projectile, and dv_P/dt is the deceleration. After making the appropriate substitutions, one will have the following relationship for penetration depth as a function of velocity:

$$P(V_C) = -\frac{\rho_p}{Y_P} \int_{V_S}^{V_C} l(v')V_T(v')dv'.$$ One should note that this integral is specific to the limits

of the impact velocity, Vs, and the first critical velocity, Vc = V-.

[2]   One can derive the un-eroded penetrator length as a
function of velocity from the force balance relationship inside the projectile at the elastic-
plastic interface. The relationship for the un-eroded penetrator length is expressed in the

following relationship: $l(v') = L\exp\left[\frac{\mu\rho_P}{2(1+\mu)Y_P}(v'^2 - V_S^2)\right]$; where L is the original

length of the penetrator, and v' is the instantaneous velolcity .

[3]   The form of the relationship for the cavity
propagation speed does not change from what I have previously introduced. As a
function of instantaneous velocity, the relationship for the cavity propagation speed is

expressed by the following: $V_T(v') = \frac{v'}{1+\mu}\frac{1-\mu\sqrt{1-\frac{V_-^2}{v'^2}(1-\mu^2)}}{1-\mu}$.   We can better

represent this function by considering a second order approximation for the instantaneous
velocity.   Given that the instantaneous velocity steadily decreases from the impact
velocity, Vs, to the first critical velocity, Vc, it is approximately equal to half the impact
velocity, $v' \approx (1/2)V$s. The final form of the instantaneous cavity propagation speed is

given by the following expression: $V_T(v') \approx \frac{v'}{1+\mu}\frac{1-\mu\sqrt{1\pm\frac{2V_-^2}{V_S^2}(1-\mu^2)}}{1-\mu} \equiv \frac{v'f}{1+\mu}$.

[4]   The final result of the integration for the penetration depth
as a function of velocity, within the limits of the impact velocity to the critical velocity, is
expressed in the following relationship. The input values and resulting calculations for
the penetration depth at the critical velocity are shown in Table 17.

$$\frac{P(V_C)}{L} \approx \frac{f}{\mu}\left(1-\exp\left[\frac{\mu\rho_P}{2(1+\mu)Y_P}(V_C^2 - V_S^2)\right]\right).$$

Variable	Units	Description	30 mm Projectile	40 mm Projectile
f	----	Cavity Propagation Parameter Function (Only for + from ±)	1.07	1.06
μ	----	Target-Projectile Density Ratio	0.64	0.64
ρ_p	kg/m^3	Density of Projectile (Tungsten)	19300	19300
Y_P	GPa	Material Strength of Projectile	1.51	1.51
V_s	m/s	Impact Velocity	828	890
V_c	m/s	First Critical Velocity	220	220
$P(V_C)/L$	----	Penetration Depth at V_c	1.17	1.24

Table 17. Penetration Depth at Critical Velocity

c. *Rigid Rod Penetration*

[1] After a penetrator reaches its critical velocity during impact, the resistance of the target's material strength influences its deceleration. We can assume that the force balance equation at the elastic-plastic interface in the target is approximately represented in the following expression: $\rho_P l_C A_P \dfrac{dv}{dt} \approx -R_T A_P$; where l_c is the un-eroded length of the penetration at the critical velocity. Starting with a function of rigid penetration with respect to time, we can manipulate this into a function with respect to instantaneous velocity. The integral form of this function and its final result are shown in the following expression: $P_{rigid} = \int_{V_C}^{0} v' dt' \approx -\dfrac{\rho_P l_C}{R_T} \int_{V_C}^{0} v' dv' = \dfrac{\rho_P l_C}{2R_T} V_C^2$. From the previous discussion of un-eroded penetrator length as a function of instantaneous velocity, we can assume that it has the following form at the critical velocity:

$l_C = L \exp\left[\dfrac{\mu \rho_P}{2(1+\mu)Y_P}(V_C^2 - V_S^2)\right]$. The final form of the rigid penetration depth and the resulting calculations are shown in the following expression and Table 18.

$$\frac{P_{rigid}}{L} \approx \frac{\rho_P V_C^2}{2R_T} \exp\left[\frac{\mu \rho_P}{2(1+\mu)Y_P}\left(V_C^2 - V_S^2\right)\right]$$

Variable	Units	Description	30 mm Projectile	40 mm Projectile
ρ_p	kg/m^3	Density of Projectile (Tungsten)	19300	19300
V_c	m/s	Critical Velocity	220	220
R_T	GPa	Material Strength of Target	1.32	1.32
μ	----	Target-Projectile Density Ratio	0.64	0.64
V_s	m/s	Impact Velocity	828	890
Y_P	GPa	Material Strength of Projectile	1.51	1.51
P_{rigid}/L	----	Rigid Penetration Depth	0.071	0.055

Table 18.   Rigid Penetration Depth

d.   *Total Penetration Depth*

[1]   30mm Projectile: $\dfrac{P_{tot}}{L} = \dfrac{P(V_C)}{L} + \dfrac{P_{rigid}}{L} = 1.24$

[2]   40mm Projectile: $\dfrac{P_{tot}}{L} = \dfrac{P(V_C)}{L} + \dfrac{P_{rigid}}{L} = 1.30$

THIS PAGE INTENTIONALLY LEFT BLANK

E.   AERODYNAMIC ANALYSIS

1.   Maple Computer Worksheet: 30mm Projectile

Maple Worksheet: Coefficient of Drag Calculation for 30mm Infantry Railgun Projectile. * Note [units are in meters, kilograms, seconds]

```
> u:=u:
c:=343:
rho:=1.20:
q:=1/2*rho*u^2:
M:=u/c:

> L:=325E-3:
L_n:=100E-3:
d:=29E-3:
f_n:=L_n/d:
gam:=1.4:
dLE:=10*3.1416/180:
TLE:=45*3.1416/180:
MLE:=M*cos(TLE):
Cmac_YF:=17.6E-3:
Cmac_PF:=14.9E-3:
tmac:=1E-3:
b_YF:=2*25.5E-3:
b_PF:=2*21.5E-3:
Sref:=665E-6:
S_YF:=673E-6:
S_PF:=482E-6:
nw:=1:
gam1:=gam/(gam-1):
gam2:=1/(gam-1):

> CDo_body_wave:=3.6/((L_n/d)*(M-1)+3):
CDo_base:=0.25/M:
CDo_body_friction:=0.053*(L/d)*(M/(q*L))^0.2*(1.71):
CDo_body:=CDo_body_wave+CDo_base+CDo_body_friction:

> CDo_YF_wave:=nw*(2/(gam*MLE^2))*
(((gam+1)*MLE^2/2)^gam1*((gam+1)/(2*gam*MLE^2-(gam-
1)))^gam2-1)*
sin(dLE)^2*cos(TLE)*tmac*b_YF/Sref:
CDo_YF_friction:=nw*(0.0133/(q*Cmac_YF)^0.2)*(2*S_YF/S
ref)*(1.71):
CDo_YF:=evalf(CDo_YF_wave+CDo_YF_friction):
```

```
> CDo_PF_wave:=nw*(2/(gam*MLE^2))*
(((gam+1)*MLE^2/2)^gam1*((gam+1)/(2*gam*MLE^2-(gam-
1)))^gam2-1)*
sin(dLE)^2*cos(TLE)*tmac*b_PF/Sref:
CDo_PF_friction:=nw*(0.0133/(q*Cmac_PF)^0.2)*(2*S_PF/S
ref)*(1.71):
CDo_PF:=evalf(CDo_PF_wave+CDo_PF_friction):

> CDo:=CDo_body+CDo_YF+CDo_PF:

> fit1:=570/u:
plot([CDo,fit1],u=343..1100,CD);
```
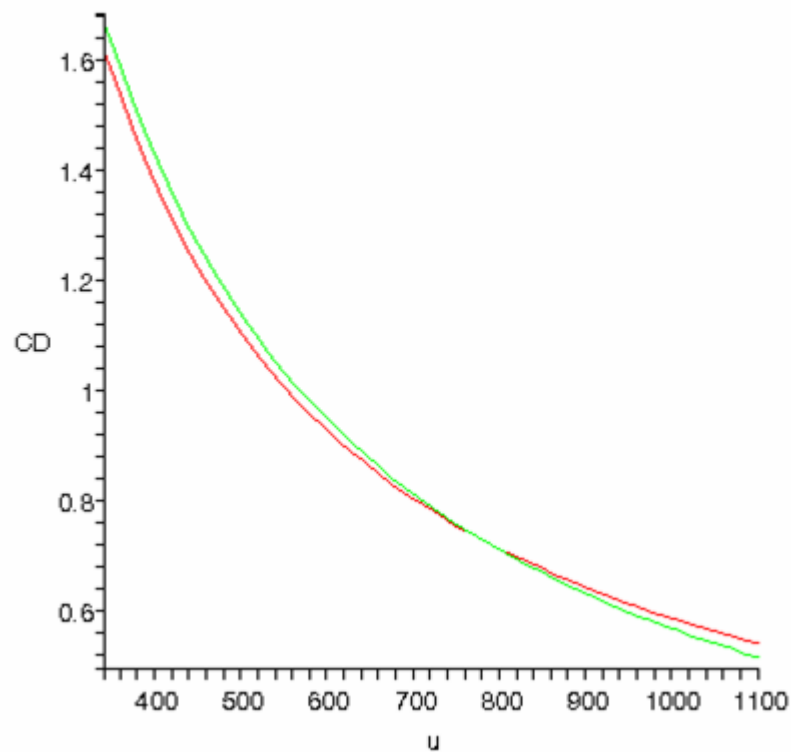
2. Maple Computer Worksheet: 40mm Projectile

Maple Worksheet: Coefficient of Drag Calculation for the 40mm Infantry Railgun Projectile. * Note [units are in meters, kilograms, seconds]

```
> u:=u:
c:=343:
rho:=1.20:
q:=1/2*rho*u^2:
M:=u/c:

> L:=433E-3:
L_n:=133.3E-3:
d:=38.8E-3:
f_n:=L_n/d:
gam:=1.4:
dLE:=10*3.1416/180:
TLE:=45*3.1416/180:
MLE:=M*cos(TLE):
Cmac_YF:=23.3E-3:
Cmac_PF:=20.0E-3:
tmac:=1.33E-3:
b_YF:=2*34.0E-3:
b_PF:=2*28.7E-3:
Sref:=1183E-6:
S_YF:=1200E-6:
S_PF:=860E-6:
nw:=1:
gam1:=gam/(gam-1):
gam2:=1/(gam-1):

> CDo_body_wave:=3.6/((L_n/d)*(M-1)+3):
CDo_base:=0.25/M:
CDo_body_friction:=0.053*(L/d)*(M/(q*L))^0.2*(1.71):
CDo_body:=CDo_body_wave+CDo_base+CDo_body_friction:

> CDo_YF_wave:=nw*(2/(gam*MLE^2))*
(((gam+1)*MLE^2/2)^gam1*((gam+1)/(2*gam*MLE^2-(gam-
1)))^gam2-1)*
sin(dLE)^2*cos(TLE)*tmac*b_YF/Sref:
CDo_YF_friction:=nw*(0.0133/(q*Cmac_YF)^0.2)*(2*S_YF/Sref)*
(1.71):
CDo_YF:=CDo_YF_wave+CDo_YF_friction:

> CDo_PF_wave:=nw*(2/(gam*MLE^2))*
(((gam+1)*MLE^2/2)^gam1*((gam+1)/(2*gam*MLE^2-(gam-
1)))^gam2-1)*
sin(dLE)^2*cos(TLE)*tmac*b_PF/Sref:
```

109

```
CDo_PF_friction:=nw*(0.0133/(q*Cmac_PF)^0.2)*(2*S_PF/Sref)*
(1.71):
CDo_PF:=CDo_PF_wave+CDo_PF_friction:

> CDo:=CDo_body+CDo_YF+CDo_PF:

> fit1:=570/u:
plot([CDo,fit1],u=343..1100,CD);
```
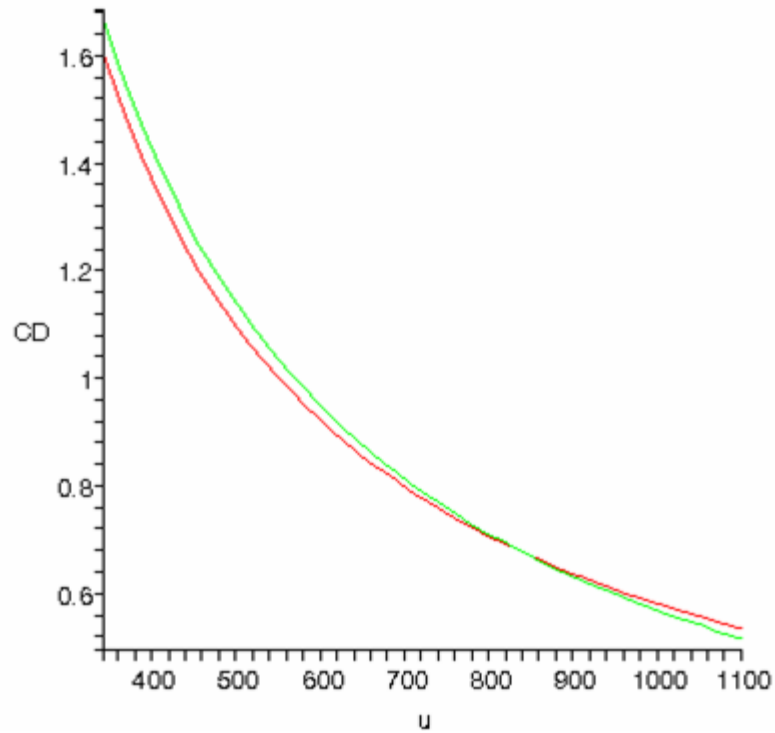
F. ELECTROMAGNETIC ANALYSIS

The purpose of this appendix is to describe the model setups for the electromagnetic launch simulations. The Comsol model setup summaries require a basic understanding of the software in order to properly replicate these simulations. All units in these models are standard metric (*mks*).

    1.   Comsol Multiphysics 30mm Model Summaries

        a.   Model Set-up

        [1] Application modes and modules used in this model:

            -Conductive Media DC (Electromagnetics Module)
            -Magnetostatics (Electromagnetics Module)
            -Heat Transfer by Conduction

        [2] Boundary mode:

[3] Subdomain mode

[4] Mesh Parameters

Parameter	Value	
Maximum element size scaling factor	0.55	
Mesh curvature factor	0.4	
Element growth rate	1.4	
Mesh curvature cut off	0.01	
Resolution of narrow regions	3	
Resolution of geometry	20	
x-direction scale factor	1/2	
y-direction scale factor	1.0	
z-direction scale factor	1.0	
Optimize quality	On	
Mesh geometry to level	Subdomain	
Subdomain	2-8	10-12
Element growth rate	3	5

[5] Mesh Statistics

Number of degrees of freedom	664244
Number of edge elements	1683
Number of boundary elements	26146
Number of elements	243932
Minimum element quality	0.0784

b.   ***Application mode type: Conductive Media DC***

[1] Application Mode Properties

Property	Value
Default element type	Lagrange - Quadratic
Input property	Fixed current density
Frame	Reference frame
Weak constraints	Off

[2]   Boundary Settings

Boundary	1-5, 81	6-15, 17-20, 22-80	
Type	Electric insulation	Continuity	
Normal current density (Jn)	0	0	
Boundary	16	21	
Type	Ground	Current source	
Normal current density (Jn)	0	1e9 [A/m^2]	

[3]   Subdomain Settings

Subdomain	1-3	4-7	
Electrical conductivity (sigma)	1e-30	5.998e7 (Copper)	
Temperature coefficient (alpha)	0.0039	17e-6 (Copper)	
Subdomain	8	9, 11-12	10
Electrical conductivity (sigma)	1e-14	1.77e7	2.5e7
Temperature coefficient (alpha)	0.0039	0.0039	0.0039

c. Application mode type: Magnetostatics (Electromagnetics Module)

[1]   Application Mode Properties

Property	Value
Default element type	Vector
Analysis type	Static
Potentials	Magnetic
Gauge fixing	On
Input property	Fixed current density
Frame	Reference frame
Weak constraints	Off

[2]   Boundary Settings

Boundary	1-5, 81	6-80
Electrostatic type	V0	Continuous
Magnetic type	A0	Continuous

[3]   Subdomain Settings

Subdomain	1-12
External current density (Je)	{'Jx_dcm';'Jy_dcm';'Jz_dcm'}

d.   Application mode type: Heat Transfer by Conduction

[1]   Application Mode Properties

Property	Value
Default element type	Lagrange - Quadratic
Analysis type	Transient
Frame	Reference frame
Weak constraints	Off

[2]   Boundary Settings

Boundary	1-5, 81	6-80
Type	Thermal insulation	Continuity

[3]   Subdomain Settings

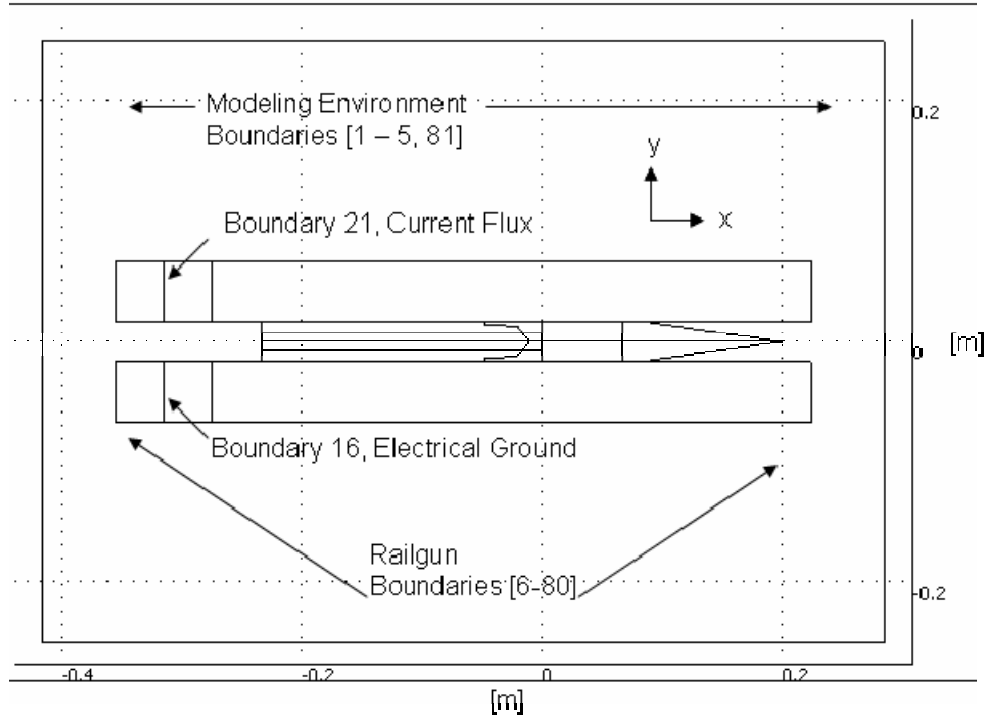| Subdomain	1-3	4-7	
Thermal conductivity (k)	0.4	400 (Copper)	
Density (rho)	1300	8700 (Copper)	
Heat capacity (C)	100	385 (Copper)	
Heat source (Q)	0	0	
Subdomain	8	9, 11-12	10
Thermal conductivity (k)	.4	163.3	167
Density (rho)	1300	19300	2700
Heat capacity (C)	100	134	896
Heat source (Q)	Q_dcm	Q_dcm	Q_dcm
Subdomain initial value	1-12		
Temperature (T)	30		

2.   Comsol Multiphysics 40mm Model Summaries
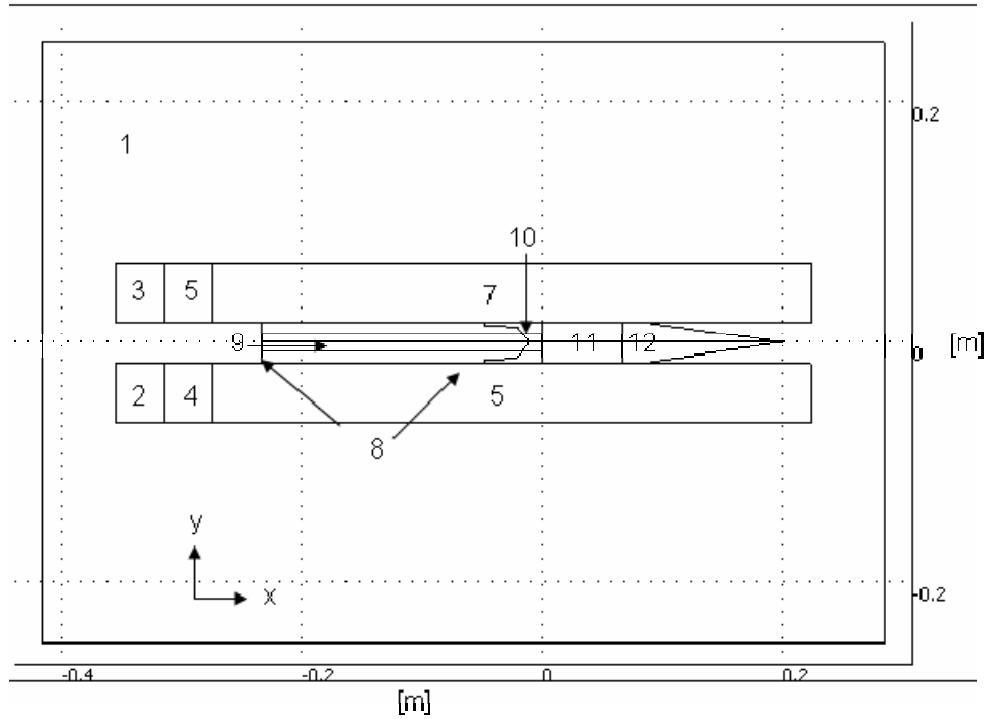
a.   *Model Set-up*

[1]   Application modes and modules used in this model:

-Conductive Media DC (Electromagnetic Module)

-Magnetostatics (Electromagnetics Module)

-Heat Transfer by Conduction

115

[2] Boundary mode:

[3] Subdomain mode:

[4] Mesh Parameters

Parameter	Value	
Maximum element size scaling factor	0.55	
Mesh curvature factor	0.4	
Element growth rate	1.4	
Mesh curvature cut off	0.01	
Resolution of narrow regions	3	
Resolution of geometry	20	
x-direction scale factor	1/2	
y-direction scale factor	1.0	
z-direction scale factor	1.0	
Optimize quality	On	
Mesh geometry to level	Subdomain	
Subdomain	2-8	10-12
Element growth rate	3	5

[5]   Mesh Statistics

Number of degrees of freedom	734998
Number of edge elements	1744
Number of boundary elements	28361
Number of elements	270442
Minimum element quality	0.0934

b.   *Application mode type: Conductive Media DC*

[1]   Application Mode Properties

Property	Value
Default element type	Lagrange - Quadratic
Input property	Fixed current density
Frame	Reference frame
Weak constraints	Off

Boundary	1-5, 81	6-15, 17-20, 22-80
Type	Electric insulation	Continuity
Normal current density (Jn)	0	0
Boundary	16	21
Type	Ground	Current source
Normal current density (Jn)	0	9e8 [A/m^2]

[3]   Subdomain Settings

Subdomain	1-3	4-7	
Electrical conductivity (sigma)	1e-30	5.998e7 (Copper)	
Temperature coefficient (alpha)	0.0039	17e-6 (Copper)	
Subdomain	8	9, 11-12	10
Electrical conductivity (sigma)	1e-14	1.77e7	2.5e7
Temperature coefficient (alpha)	0.0039	0.0039	23.4e-6

c. Application mode type: Magnetostatics (Electromagnetics Modules)

[1]   Application Mode Properties

Property	Value
Default element type	Vector
Analysis type	Static
Potentials	Magnetic
Gauge fixing	On
Input property	Fixed current density
Frame	Reference frame
Weak constraints	Off

[2]   Boundary Settings

Boundary	1-5, 81	6-80
Electrostatic type	V0	Continuous
Magnetic type	A0	Continuous

[3]   Subdomain Settings

Subdomain	1-12
External current density (Je)	{'Jx_dcm';'Jy_dcm';'Jz_dcm'}

d. Application mode type: Heat Transfer by Conduction

[1] Application Mode Properties

Property	Value
Default element type	Lagrange - Quadratic
Analysis type	Transient
Frame	Reference frame
Weak constraints	Off

[2] Boundary Settings

Boundary	1-5, 81	6-80
Type	Thermal insulation	Continuity

[3] Subdomain Settings

Subdomain	1-3	4-7	
Thermal conductivity (k)	0.4	400 (Copper)	
Density (rho)	1300	8700 (Copper)	
Heat capacity (C)	100	385 (Copper)	
Heat source (Q)	0	0	
Subdomain	8	9, 11-12	10
Thermal conductivity (k)	.4	163.3	167
Density (rho)	1300	19300	2700
Heat capacity (C)	100	134	896
Heat source (Q)	Q_dcm	Q_dcm	Q_dcm
Subdomain initial value		1-12	
Temperature (T)		30	

THIS PAGE INTENTIONALLY LEFT BLANK

LIST OF REFERENCES

[1] Cilli, Matthew. *U.S. Army Electromagnetic (EM) Gun Program*, presented at the Armament Research, Development & Engineering Center, January 2005.

[2] Schmidt, Edward. *Army Research in Electromagnetic Launch*, presented at the Tactical Power Sources Summit, February 2005.

[3] Bacon, L. and Sharoni, A.. *The Future Combat System (FCS)*. ARMOR Magazine, July-August 1997.

[4] Light Armored Vehicle (LAV). http://globalsecurity.org/military/systems/ground/m2a3.htm, November 2005.

[5] Future Combat System (FCS). http://globalsecurity.org/military/systems/ground/fcs-t.htm, November 2005.

[6] Site visit by NPS Railgun Research Group students to the Institute for Advanced Technology, University of Texas, Austin, March 2005.

[7] Marshall, R. and Yang, W. *Railguns: Their Science and Technology*. Langfang People Printing House, 2004.

[8] Crawford, Mark. *Railgun System Technology*, presented at the Naval Postgraduate School, May 2004.

[9] Ellis,R., Poynor, J., McGlasson, B. and Smith, A. *Influence of Bore and Rail Geometry on an Electromagnetic Naval Railgun System*. IEEE Transactions on Magnetics, Vol. 41, No. 1, January 2005.

[10] Tzeng, J. and Schmidt, E. *Advanced Materials Bring Electromagnetic Gun Technology One Step Closer to the Battlefied*. The AMPTIAC Quarterly, Vol. 8, No. 4, 2004.

[11] Cooke, Gary. *M242 25mm Automatic Gun*. http://www.inetres.com/gp/military/cv/weapon/M242.html, November 2005.

[12] Department of the Army Pamphlet 385-63. *Range Safety*. Headquarters Department of the Army, 10 April 2003.

[13] Brady, James. 101st ABN DIV, Infantry Company Commander. Operation Iraqi Freedom, March 2003 to September 2003.

[14] Rhinoceros Version 3.0, Robert McNeel & Associates, 2002.

[15] MatWeb Material Property Data. http://www.matweb.com, November 2005.

[16] Quadrant, Inc. Engineering Plastic Products. http://www.quadrantepp.com/source/celazole.html, November 2005.

[17] Pengelly, Rupert. *Medium-caliber ammunition innovations for AFV applications*. Jane's International Defense Review, June 1, 2003.

[18] Foss, Christopher. *European Armoured Fighting Vehicle Programmes – Balancing acts*. Jane's Defense Weekly, September 14, 2005.

[19] Zielinski, A. and Silsby, G. *Hypervelocity Penetration Impacts in Concrete Targets*. Army Research Laboratory, September 1999.

[20] Zukas, J., Nicholas, T., Swift, H., Greszczuk, L., and Curran, D.. *Impact Dynamics*. Krieger Publishing Company, 1992.

[21] Anderson, C., Morris, B., and Littlefield, D. *A Penetration Mechanics Database*. Southwest Research Institute, January 1992.

[22] Sliter, George. *Assessment of Empirical Concrete Impact Formulas*. Journal of the Structural Division, proceedings of the American Society of Civil Engineers, Vol. 106, No. 1, January 1980.

[23] Li, Q. and Chen, X. *Dimensionless formulae for penetration depth of concrete target impacted by a non-deformable projectile*. International Journal of Impact Engineering, Vol. 28, 2003.

[24] Brown, Ronald. Private Correspondence. Naval Postgraduate Professor in the Department of Physics, August 2005.

[25] AUTODYN Version 5.0. Century Dynamics, Inc., 2004.

[26] Borden, B. and Woehler, K. *Physics of High Velocity Impact, Weapons Lethality, and Survivability*. PH4857 Course Notes, Naval Postgraduate School, February 2003.

[27] Siong, N. and Raghavan, D. *Numerical Simulations For Optimizing Penetration Of Segmented Projectiles*. http://staff.science.nus.edu.sg/~scilooe/srp_2003/sci_paper/dsta/research_paper/neo_wei_siong.pdf. November 2005.

[28] Fleeman, Eugene. *Tactical Missile Design*. American Institute of Aeronautics and Astronautics, Inc., 2001.

[29] Pitts, W., Nielson, J., and Kaattari, G. *Lift and Center of Pressure of Wing-Body-Tail Combinations at Subsonic, Transonic, and Supersonic Speeds*. NACA Report 1307, January 1957.

[30] Longitudinal Static Stability. http://adg.standford.edu/aa241/stability/staticstability.html, November 2005.

[31] Plostins, P., Soencksen, K., Zielinski, A., and Hayden, T. *Aeroballistic Evaluation of Kinetic Engery (KE) Penetrators for Electromagnetic (EM) Gun Applications*. Army Research Laboratory, ARL-TR-922, January 1996.

[32] Liepmann, H. and Roshko, A. *Elements of Gasdynamics*. Dover Publications, Inc, 2001.

[33] Baker, Steve. *Missile Design Final Project*. SE4860 Course Notes, Naval Postgraduate School, April 2004.

[34] Maple Version 9. Maplesoft, Waterloo Maple Inc., 2003.

[35] Kerrisk, J.F. *Current Distribution and Inductance Calculations for Rail-Gun Conductors*. Los Alamos National Laboratory, November 1981.

[36] Maier, William B., III. *Selected Topics in Railgun Technology*. PH3994 Course Notes, Naval Postgraduate School, January 2005.

[37] Hypertextbook. *Resistivity of Tungsten*, http://hypertextbook.com/facts/2004/DeannaStewart.shtml, November 2005

[38] Comsol Multiphysics Version 3.2, Comsol, Inc., September 2005.

[39] Quan, Chris. Private Correspondence. Century Dynamics AUTODYN technical advisor, November 2005.

THIS PAGE INTENTIONALLY LEFT BLANK

INITIAL DISTRIBUTION LIST

1. Defense Technical Information Center
   Ft. Belvoir, Virginia

2. Dudley Knox Library
   Naval Postgraduate School
   Monterey, California

3. Dr. William B. Maier II
   Naval Postgraduate School
   Monterey, California

4. Dr. Mark Crawford
   Institute for Advanced Technology
   Austin, Texas

5. Dr. Hans Mark
   Institute for Advanced Technology
   Austin, Texas

6. Dr. Ian McNab
   Institute for Advanced Technology
   Austin, Texas

7. Dr. Edmund Schmidt
   U.S. Army Research Laboratory
   Adelphi, Maryland

8. Dr. Alexander Zielinski
   U.S. Army Research Laboratory
   Adelphi, Maryland

9. Dr. Matthew Cilli
   Armament, Research, Development, and Engineering Center
   Picatinny, New Jersey

10. CAPT Roger D. McGinnis, USN
    Office of Naval Research
    Arlington, Virginia

11. CAPT David Kiel, USN
    Naval Sea Systems Command
    Washington, D.C.

12.   Dr. Robert Hebner
Center for Electromechanics
Austin, Texas

13.   Dr. John Pappas
Center for Electromechanics
Austin, Texas